THE LUMINOUS POLYCYCLIC AROMATIC HYDROCARBON EMISSION FEATURES: APPLICATIONS TO HIGH REDSHIFT GALAXIES AND ACTIVE GALACTIC NUCLEI

A Dissertation

by

HEATH VERNON SHIPLEY

Submitted to the Office of Graduate and Professional Studies of
Texas A&M University
in partial fulfillment of the requirements for the degree of

DOCTOR OF PHILOSOPHY

Chair of Committee,	Casey J. Papovich
Committee Members,	Darren DePoy
	Bashkar Dutta
	Ping Yang
Head of Department,	Lewis A. Ford

August 2015

Major Subject: Physics & Astronomy

ABSTRACT

The co-evolution of star-formation and supermassive black hole (SMBH) accretion in galaxies is one of the key problems in galaxy formation theory. Understanding the formation of galaxies, and their subsequent evolution, will be coupled to intensive study of the evolution of SMBHs. This thesis focuses on studying diagnostics of star-formation and SMBH accretion to develop tools to study this co-evolution.

Chapter 2 consists of using mid-infrared (mid-IR) spectroscopy from the *Spitzer* Infrared Spectrograph (IRS) to study the nature of star-formation and SMBH accretion. The mid-IR spectra cover wavelengths 5-38μm, spanning the polycyclic aromatic hydrocarbon (PAH) features and important atomic diagnostic lines. We divide our sample into a subsample of galaxies with *Spitzer* IRAC colors indicative of warm dust heated by an AGN (IRAGN) and those galaxies whose colors indicate star-formation processes (non-IRAGN). In both the IRAGN and star-forming samples, the luminosity in the PAH features correlates strongly with [Ne II]λ12.8μm emission line, from which we conclude that the PAH luminosity directly traces the instantaneous star-formation rate (SFR) in both the IRAGN and star-forming galaxies. There is no measurable difference between the PAH luminosity ratios of $L_{11.3}/L_{7.7}$ and $L_{6.2}/L_{7.7}$ for the IRAGN and non-IRAGN, suggesting that AGN do not significantly excite or destroy PAH molecules on galaxy-wide scales.

In chapter 3, I calibrate the PAH luminosity as a SFR indicator. We provide a new robust SFR calibration using the luminosity emitted from PAH molecules at 6.2μm, 7.7μm and 11.3μm. The PAH features emit strongly in the mid-IR mitigating dust extinction, containing on average 5$-$10% of the total IR luminosity in galaxies. We use mid-IR spectroscopy from the *Spitzer*/IRS, and data covering other SFR

indicators (Hα emission and rest-frame 24μm continuum emission). The PAH luminosity correlates linearly with the SFR as measured by the Hα luminosity (corrected for attenuation using the mono-chromatic rest-frame 24um emission), with a tight scatter of <0.15 dex. The scatter is comparable to that between SFRs derived from the Paα and dust-corrected Hα emission lines, implying the PAH features may be as accurate a SFR indicator as the Hydrogen recombination lines. Because the PAH features are so bright, our PAH SFR calibration enables an efficient way to measure SFRs in distant galaxies with *JWST* to SFRs as low as $\sim$10 $M_\odot$ yr^{-1} to z $\lesssim$ 2. We use *Spitzer*/IRS observations of PAH features in lensed star-forming galaxies at 1 < z < 3 to demonstrate the utility of the PAHs to derive SFRs as accurate as those available from Paα.

Chapter 4 is the application of the PAH SFRs for galaxies with AGN to demonstrate the reliability for studies of the co-evolution of star-formation and SMBH accretion. We present a study of the contribution from star-formation in galaxies of varying AGN activity (from pure star-forming galaxies to quasars) as a function of total IR luminosity using a sample of 220 galaxies. We use mid-IR spectroscopy from the *Spitzer*/IRS and photometry from the MIPS 24μm, 70μm and 160μm bands with partial coverage of the sample with the Herschel 160μm band for the quasars. The contribution from star-formation to the total IR luminosity implied by the PAH emission decreases with increasing IR luminosity. We find a similar result to previous studies for the correlation between SFR, i.e. PAH luminosity, and AGN luminosity for quasars of $L_{SF} \propto L_{AGN}^{0.67\pm0.10}$ and $L_{SF} \propto L_{AGN}^{0.55\pm0.15}$ for the 11.3μm PAH feature only (which has been shown to be the most reliable PAH feature in the vicinity of AGN). This may indicate the PAH luminosity remains a reliable tracer of the SFR for galaxies with strong AGN contributions (i.e. quasars), as we did not subtract off the AGN component before measuring the SFR from the PAH luminosity.

ACKNOWLEDGEMENTS

We thank our collaborators that contributed valuable insight and comments to improve the thesis: George Rieke (University of Arizona, Arizona), John Moustakas (Siena College, NY), Michael Brown (Monash University, Australia), Arjun Dey (NOAO, AZ), Buell Jannuzi (University of Arizona and NOAO, AZ) and Benjamin Weiner (University of Arizona, AZ). A very special thank you to my advisor Casey Papovich who helped guide me throughout my thesis and provided invaluable advice to me all along the way.

We thank Nicholas Suntzeff and Darren DePoy for comments that helped improve the thesis. We also thank Rob Kennicutt Jr. and Daniela Calzetti for valuable discussions that added to the improvement of the thesis. We thank our colleagues on the NDWFS, AGES teams. We thank JD Smith for comments that helped improve the thesis. This work utilized the PAHFIT IDL tool for decomposing IRS spectra, which J. D. Smith has generously made publicly available (Smith et al., 2007). We thank the MPA/JHU collaboration for SDSS studies for making their catalogs publicly available.

Support for the work presented in this thesis was provided by the NASA Astrophysics Data Analysis Program (ADAP) for the proposal "Measuring Star-Formation Rates of AGNs and QSOs using a new calibration from Polycyclic Aromatic Hydrocarbon Emission" (14-ADAP14-0228), submitted in response to NNH14ZDA001N-ADAP, Research Opportunities in Space and Earth Sciences (ROSES-2014). Further support for this work was provided to the author by the George P. and Cynthia Woods Mitchell Institute for Fundamental Physics & Astronomy.

This work made use of images and/or data products provided by the NOAO

Deep Wide-Field Survey (Jannuzi & Dey, 1999; Jannuzi et al., 2004; Dey et al., 2004), which is supported by the National Optical Astronomy Observatory (NOAO). NOAO is operated by AURA, Inc., under a cooperative agreement with the National Science Foundation. The research of AD is supported by NOAO, which is operated by the Association of Universities for Research in Astronomy, Inc., under a cooperative agreement with the NSF. This work is based in part on observations and archival data obtained with the Spitzer Space Telescope, which is operated by the Jet Propulsion Laboratory, California Institute of Technology under a contract with NASA. Partial support for this work was provided by NASA through awards 1255094 and 1365085 issued by JPL/Caltech.

Funding for the SDSS has been provided by the Alfred P. Sloan Foundation, the Participating Institutions, NASA, NSF, the U.S. Department of Energy, the Japanese Monbuk- agakusho, the Max Planck Society, and the Higher Educa- tion Funding Council for England. The SDSS Web site is http://www.sdss.org/. The SDSS is managed by the Astrophysical Research Consortium for the Participating Institutions. The Participating Institutions are the American Museum of Natural History, Astrophysical Institute Potsdam, University of Basel, University of Cambridge, Case Western Reserve University, University of Chicago, Drexel University, Fermilab, the Insti- tute for Advanced Study, the Japan Participation Group, Johns Hopkins University, the Joint Institute for Nuclear Astrophysics, the Kavli Institute for Particle Astrophysics and Cosmology, the Korean Scientist Group, the Chinese Academy of Sciences (LAMOST), Los Alamos National Laboratory, the Max-Planck-Institute for Astronomy (MPIA), the Max-Planck-Institute for Astrophysics (MPA), New Mexico State University, Ohio State University, University of Pittsburgh, University of Portsmouth, Princeton University, the United States Naval Observatory, and the University of Washington.

TABLE OF CONTENTS

Page

ABSTRACT ii

ACKNOWLEDGEMENTS iv

TABLE OF CONTENTS vi

LIST OF FIGURES ix

LIST OF TABLES xix

1. INTRODUCTION 1

2. DIAGNOSTICS OF AGN AND STAR-FORMATION AND THE IMPORTANCE OF PAH EMISSION USING SPITZER SPECTROSCOPY OF INFRARED-LUMINOUS GALAXIES 4

2.1 Background 4
2.2 Sample Definition and Selection 7
2.3 *Spitzer* Imaging Data 14
2.3.1 Boötes Field 14
2.3.2 *Spitzer* First Look Survey (FLS) 15
2.3.3 IRAC AGN Selection 15
2.4 IRS Observations, Data Reduction, and Analysis 18
2.4.1 IRS Observations 18
2.4.2 Data Reduction 18
2.4.3 IRS Spectral Fitting 20
2.4.4 Offset Between IRS SL and LL Modules 25
2.5 Comparison of Mid-IR Emission Features and Relation to Total Infrared Luminosity 26
2.5.1 Composite Spectra 26
2.5.2 Measuring the Total Infrared Luminosity 28
2.5.3 Contribution of PAH Emission to L_{IR} 29
2.5.4 Detection Frequency of Emission Features 31
2.5.5 Measures of Grain Sizes and Ionization State 35
2.5.6 Relation between Radiation Hardness and PAH Strength . . . 37
2.5.7 The Distribution of the 6.2μm PAH Equivalent Width 40

2.5.8 The Relationship Between PAH Luminosity, Star-formation Rate, and AGN Luminosity . . . 43
2.6 Discussion . . . 44
2.6.1 The Color-Magnitude Diagram for IR Luminous Galaxies . . . 44
2.6.2 AGN Effects on PAH Emission and AGN Contribution to L_{IR} 49
2.6.3 Emission Ratios of Short-to-Long Wavelength PAHs in IRAGN and non-IRAGN . . . 52
2.6.4 Galaxies with Excess [O IV] $\lambda 25.9\mu$m Emission . . . 54

3. A NEW STAR-FORMATION RATE CALIBRATION FROM POLYCYCLIC AROMATIC HYDROCARBON EMISSION FEATURES: APPLICATION TO HIGH REDSHIFT GALAXIES . . . 58

3.1 Background . . . 58
3.2 Sample and Data . . . 61
3.2.1 Calibration Samples . . . 61
3.2.2 Application Sample of High Redshift Galaxies . . . 65
3.3 Derived Quantities . . . 68
3.3.1 IRS Spectral Fitting . . . 68
3.3.2 Optical Spectral Fitting . . . 69
3.3.3 Dust-Corrected Hα Emission from Rest-Frame MIPS 24 μm Flux . . . 70
3.3.4 Gas-Phase Metallicities . . . 73
3.3.5 Total Infrared Luminosity . . . 75
3.4 The PAH SFR Calibration . . . 77
3.4.1 PAH SFR Relations . . . 77
3.4.2 Uncertainties for Derived SFR Relations . . . 84
3.4.3 Correction to PAH Luminosity for Low Metallicity Galaxies . 86
3.4.4 The Interesting Galaxy: II Zw 096 . . . 87
3.5 Comparison to Previous Studies of PAH SFR Calibrations . . . 90
3.5.1 Comparison to PAH SFRs Calibrated to the Total Infrared Luminosity . . . 92
3.5.2 Comparison to PAH SFRs Calibrated to mid-IR Atomic Emission Lines . . . 96
3.6 SFRs of High Redshift (Lensed) Galaxies: A Preview for *JWST* . . . 97
3.6.1 SFRs for Galaxies at $z \sim 1$ . . . 101
3.6.2 SFRs for Galaxies at $2 < z < 3$ . . . 101

4. THE ROLE OF STAR-FORMATION IN GALAXIES FROM STARBURSTS TO QUASARS AS A FUNCTION OF TOTAL IR LUMINOSITY USING PAH EMISSION . . . 105

4.1 Background . . . 105

4.2 Sample and Data 108
4.2.1 O'Dowd et al. (2009) Sample 110
4.2.2 Shipley et al. (2013) Sample 110
4.2.3 Shi et al. (2014) Sample 111
4.3 Analysis of PG and 2MASS Quasars for Shi et al. (2014) Sample . . . 112
4.3.1 *Spitzer* IRS Spectral Fits 112
4.3.2 Total IR Luminosity 114
4.4 Distribution Functions of Star-Formation and AGN Luminosities . . . 115
4.4.1 Star-Formation as a Function of Total IR Luminosity 115
4.4.2 Star-Formation in Quasars 120
4.5 Disscussion 122
4.5.1 The Correlation Between L_{SF} and L_{AGN} 122
4.5.2 Comparison to Models 125

5. SUMMARY AND CONCLUSIONS 127

REFERENCES 135

APPENDIX A. ESTIMATING THE TOTAL IR LUMINOSITY 155

LIST OF FIGURES

FIGURE Page

2.1 — Color-Magnitude Diagram using optical data from the AGES catalog for our sample. The grey-shading indicates the density of all galaxies from AGES in that region of color-magnitude space and $0.02 < z < 0.6$, where the grey-shading increases as the density increases linearly. The cyan points show those AGES sources with $0.02 < z < 0.6$ and $f(24\mu\text{m}) \geq 1.2$ mJy, the IRS spectroscopic limit for our sample. The galaxies selected in our sample are indicated by white squares, white circles, and yellow diamonds for Dole (program 20113), Lagache (program 20128, non-FLS sources), and Rieke (program 40251), respectively. Furthermore, we selected IR-luminous galaxies for our sample such that they span the full range of $(u-r)_{0.1}$ optical color with an equal number (12-13) galaxies in each of four bins, denoted by the red-dashed lines and defined in section 2.2. 10

2.2 — Distribution of the redshifts and 24μm flux densities of the 65 galaxies in our IRS sample. The galaxies are indicated by white squares, white circles, and yellow diamonds for Dole (program 20113), Lagache (program 20128), and Rieke (program 40251), respectively. The orange circles are from O'Dowd et al. (2009) sample as a comparison to our sample. The red dashed line indicates $f_\nu(24\mu\text{m}) = 1.2$mJy. The redshift mean and median of the distribution are 0.30 and 0.28, respectively. The redshift distribution is fairly uniform from $0.2 < z < 0.6$, with an interquartile range (which contains the inner 50% of galaxies) of $z_{\text{interquartile}} = 0.18 - 0.42$. 11

2.3 — IRAC colors of [5.8] - [8.0] versus [3.6] - [4.5] for galaxies in our IRS sample. Here, the IRAC colors are in the Vega magnitude system, following Stern et al. (2005). The blue circles are sources from the Boötes field and green diamonds are FLS sources. The dotted lines show the empirical selection-criteria for IRAC-AGN selection: galaxies inside this "wedge" are IRAC-selected AGN (Stern et al., 2005). We denote the subsample of galaxies in our IRS sample that satisfy these colors as IRAGN. We denote galaxies outside this wedge as non-IRAGN, and we expect the IR emission in these objects to be dominated by star-formation. 17

2.4 — Examples of PAHFIT spectral decomposition to object 23 (top) and object 4 (bottom). In each panel, the IRS spectroscopic data are shown as black squares. The total fit and individual spectral components fit by PAHFIT are shown, including the molecular and atomic emission features (blue curves), dust continua (red), and stellar light (magenta). The total fit (the sum of all the model components) is shown in green, which provides a good representation of the data. . 20

2.5 — Composite spectra for the IRS sample. The top panel shows the composite spectrum for all 65 galaxies in the IRS sample. The middle and bottom panels show composite spectra for the subsamples of IRAGN (14 galaxies) and non-IRAGN (51 galaxies), respectively. The vertical red-dashed lines indicate the prominent PAH features and emission lines in the wavelength range, as labeled. The flux is normalized at the continuum flux of 21μm. The outset panels show the composite spectra in a small wavelength region 24.5μm-27.5μm to show the strength of the [O IV] λ25.9μm emission line (see section 2.5.1 for explanation). The error bars shown is the error on the weighted mean for each composite spectrum. 27

2.6 — Redshift versus the total IR luminosity from 8-1000μm for our IRS sample (blue circles, Boötes sources; green diamonds, FLS sources) derived from the MIPS 24 μm data (and 70 and 160 μm, if available) derived using the Rieke et al. (2009) IR SEDs. The galaxies in our IRS sample span the range of IR luminosity of "Luminous IR galaxies" (LIRGs), $L_{IR} = 10^{11} - 10^{12} L_{\odot}$. The figure also shows the O'Dowd et al. (2009) SSGSS sample (orange circles), which are lower redshift and IR luminosity. The dashed curve shows the limiting IR luminosity as a function of redshift for a fixed 24 μm flux density of 1.2 mJy using the IR SEDs from Rieke et al. (2009). 30

2.7 — The distribution of L_{PAH}/L_{IR} for our sample, where L_{PAH} is the total luminosity of the 6.2, 7.7, 8.6, 11.3, 12.7, and 17.0μm PAH emission features. The bottom panel shows the distribution for our IRS sample. The middle panel shows the distribution for our subsample of IRAGN, and the top panel shows the distribution for our subsample of non-IRAGN. The median L_{PAH}/L_{IR} is 0.05 for the IRAGN, and is about half that for the non-IRAGN which have a median of L_{PAH}/L_{IR} = 0.09. The arrows represent the L_{PAH}/L_{IR} ratios from the composite spectra in figure 2.5 (L_{PAH}/L_{IR} = 0.09, 0.06, and 0.10 for the IRS sample, IRAGN, and non-IRAGN, respectively). 32

2.8 — Detection frequencies for common mid-IR PAH features and atomic emission lines in the IRS sample. Each histogram gives the frequency that a given emission feature is detected at $\geq 3\sigma$ significance in the IRS sample (black bars), or the IRAGN (red bars) or the non-IRAGN (blue bars) subsamples. On the abscissa, atomic features are labled, and PAH emission features are denoted by their central wavelengths. 35

2.9 — PAH band ratios $L_{6.2}/L_{7.7}$ vs. $L_{11.3}/L_{7.7}$ for the galaxies in the IRS sample. The $L_{6.2}/L_{7.7}$ ratio is a tracer of PAH grain size, and the $L_{11.3}/L_{7.7}$ ratio is a tracer of PAH grain ionization (O'Dowd et al., 2009). The red squares denote IRAGN and the blue circles denote non-IRAGN galaxies. The IRS sample falls mostly within the locus defined by 0.2–0.4 in both axes. This shows that the galaxies have a mixture of grain sizes and different ionization fractions of PAHs. We measure a weak correlation between $L_{6.2}/L_{7.7}$ and $L_{11.3}/L_{7.7}$ (Spearman's $\rho = 0.41$), which we interpret as evidence for decreasing PAH grain size and increasing ionization within the locus. We also observe that the IRAGN ratios are slightly lower typically compared to the non-IRAGN galaxies, in our IRS sample. 38

2.10 — $[\text{Ne III}]_{15.6\mu m}/[\text{Ne II}]_{12.8\mu m}$ versus $L_{7.7}/L_{11.3}$. Blue circles show the subsample of non-IRAGN, and red squares show the subsample of IRAGN (not all IRAGN have [Ne III]/[Ne II] ratio detections). The dashed line is the median $L_{7.7}/L_{11.3}$ value for the non-IRAGN subsample only. There is no trend between [Ne III]/[Ne II] and $L_{7.7}/L_{11.3}$ for either the non-IRAGN or IRAGN. This is similar to the conclusions from other studies (O'Dowd et al., 2009; Wu et al., 2010), but contrasts with the findings of Smith et al. (2007), although we expect this difference, in part, is due to issues with the full integrated light (nucleus and outer regions from the galaxies in our IRS sample fall within the IRS aperture in constrast to the sample of Smith et al., 2007). 39

2.11 — PAH 6.2μm equivalent width versus the $L_{7.7}/L_{11.3}$ PAH ratio. The dashed lines show selection criteria to separate sources into AGN, composite, and SB galaxies, as labeled in the figure. Galaxies with EW ≤ 0.2 μm are likely AGN (red-dashed line), galaxies with EW > 0.5 μm are SB galaxies (blue-dashed line), and galaxies that fall between these lines are likely AGN+SB composites. We observe no correlation between $L_{7.7}/L_{11.3}$ and the EW of the 6.2μm PAH feature. 41

2.12 — The relationship between the PAH emission features and the [Ne II] (top panel) and [O IV] (bottom panel) emission lines. All units are in W/m^2. The top panel shows a correlation between the PAH emission and [Ne II] emission line suggesting PAH emission correlates with star formation. The dashed line represents a linear fit ($0.02 \times {F_{7.7+11.3}}^{0.99}$) to the sample. The bottom panel shows that there is little, if any, correlation between PAH emission and [O IV], but there is a population of objects with low PAH emission and excess [O IV] emission. The upper dashed line is four times greater than the fit to the non-IRAGN subsample (lower dashed line) used to select the [O IV]-excess objects. 45

2.13 — Optical $(u-r)_{0.1}$ color-magnitude diagram. Both plots are similar to figure 2.1 except for symbol changes to the Boötes IRS sample. (*Top Panel*) The sample symbols denote IRAGN (red squares), non-IRAGN (blue circles), and non-IRAGN galaxies with excess [O IV] (defined in section 2.5.8, black open circles). (*Bottom Panel*) The sample symbols denote galaxy IR luminosity as low-luminosity galaxies ($L_{IR} = 10^{10} - 2.4 \times 10^{11}$ $L_\odot$, green diamonds), medium-luminosity galaxies ($L_{IR} = 2.4 \times 10^{11} - 4.5 \times 10^{11}$ $L_\odot$, purple circles), and high-luminosity galaxies ($L_{IR} > 4.5 \times 10^{11} L_\odot$, orange squares). 47

2.14 — The relationship between the luminosity of the PAH emission features and the [Ne II] emission line. The [Ne II] luminosity correlates strongly with the PAH luminosity, with a Spearman correlation coefficient of $\rho = 0.90$ and a linear fit (dashed line) of $\mathrm{Log}(L[\mathrm{Ne\ II}]) = 1.02 \pm 0.03 \times \mathrm{Log}(L_{7.7+11.3})$ - 1.71 ± 0.25. 50

2.15 — The total IR luminosity versus the PAH luminosity as an indicator for the contribution of AGN luminosity to the L_{IR}. The shaded regions represent percent amounts, marked in the plot, for the contribution of AGN luminosity to the total IR luminosity for the IRAGN in our sample under the assumption that the PAH luminosity traces the total SFR (see section 2.6.2 for explanation). 51

2.16 — The IRS mid-IR spectra of three non-IRAGN galaxies in our IRS sample with excess [O IV] emission and no other indications of an AGN. The continuous spectrum of each galaxy is shown, but split to better show the spectrum and excess [O IV] emission. Note range of y-axis differs from left to right panel for each spectrum. The open circles are the measured flux densities from the *Spitzer* IRS data observations with error bars representing the uncertainties in those measurements and the green line represents the best fit from spectral decomposition of PAHFIT. All three galaxies show clear emission from [O IV] at 25.9μm. 55

2.17 — The optical spectra of three non-IRAGN galaxies in our IRS sample with excess [O IV] emission and no other indications of an AGN. Galaxy IDs 6 and 50 are optical spectra from AGES. Galaxy 55 is from the FLS and has an optical spectrum from Papovich et al. (2006). The emission lines of [O III] λ5007Å, Hβ λ4861Å, [N II] λ6583Å, and Hα λ6563Å have been marked to indicate the atomic lines used for optical classification of galaxies as star-forming, composite, or AGN (Kewley et al., 2001; Kauffmann et al., 2003). The redshifts listed for each galaxy are the given optical redshifts from AGES (see table 2.1). 57

3.1 — In each panel, the open circles are the measured flux densities from the *Spitzer*/IRS data observations with error bars representing the uncertainties in those measurements and the green line represents the best fit from spectral decomposition of PAHFIT. The (Right) panel shows the *Spitzer*/IRS LL1 spectrum of the strongly gravitationally lensed galaxy, the "8 o'clock arc" (see § 3.2.2 and table 3.5). Because of the galaxy's high redshift, z=2.731, not all PAH features are accessible, but the 6.2μm SFR = 302 $\pm$ 20.0 $M_\odot$ yr^{-1} and the 7.7μm SFR = 262 $\pm$ 36.7 $M_\odot$ yr^{-1}. In contrast, the *Spitzer*/IRS SL2 spectrum (Left) panel gives a consistent SFR from Paα, SFR = 265 $\pm$ 29.6 $M_\odot$ yr^{-1}. 69

3.2 — Examples of our fits (green dot-dashed line) to the optical spectra (solid black line) for Brown et al. (2014) for the Hα and [N II] emission lines (see § 3.3.2 for fitting procedure). Here, we show NGC 6052 (star-forming) and NGC 5256 (AGN) that is representative of the entire Brown et al. (2014) sample for each classification (see § 3.3.2 for classification). 72

3.3 — The relation between the dust-corrected Hα luminosity and the dust correction factor, defined as the ratio of the dust-corrected Hα to observed (uncorrected) Hα. The horizontal lines show the 25, 50, and 75 percentiles of the distribution. The median correction factor is 4.2 and the interquartile range (25−75 percentiles) is 2.5 − 5.9. The orange symbols are low metallicity galaxies as defined in § 3.3.4. The blue point enclosed by a black circle denotes II Zw 096, see § 3.4.4. . 74

3.4 — Histogram of the metallicities for all the star-forming galaxies in the calibration sample, where the metallicities are 12 + log(O/H)$_{N2}$. For the calibration of the SFR relations using PAH luminosity we used galaxies with 12 + log(O/H)$_{N2} \geq 8.5$ (red dashed line) for our primary calibration sample. The resulting cut being ∼0.65 the solar abundance (12 + log(O/H) = 8.69, Asplund et al., 2009, orange dashed line). . . 76

3.5 — The dust corrected Hα luminosity (L$_{\mathrm{H}\alpha}$ + 0.020×L$_{24\mu\mathrm{m}}$, Kennicutt et al., 2009) versus the total PAH luminosity (L$_{6.2\mu\mathrm{m}}$ + L$_{7.7\mu\mathrm{m}}$ + L$_{11.3\mu\mathrm{m}}$ PAH features, top panel). We fit a unity relation to the primary calibration sample (solid black line) and use this line as L$_{\mathrm{fit}}$ to show the ratio of the total PAH luminosity to the unity relationship as a function of dust-corrected Hα luminosity (bottom panel). We classify galaxies as star-forming (blue points), composite (green points) or an AGN (red points) based on the location of their emission line ratios on a BPT diagram. Unclassified galaxies (purple points) did not have all lines required for BPT classification and galaxies with low metallicity or S/N (orange points) we exclude for the fit (see text for more detail). The blue point enclosed by a black circle denotes II Zw 096, see § 3.4.4. 79

3.6 — The dust corrected Hα luminosity (L$_{\mathrm{H}\alpha}$ + 0.020×L$_{24\mu\mathrm{m}}$, Kennicutt et al., 2009) versus L$_{\mathrm{PAH}}$ (top left) and for the 6.2μm (top right), 7.7μm (bottom left) and 11.3μm (bottom right) PAH features separately. This illustrates that the small scatter persists for the individual PAH features ($\sigma_{\mathrm{MAD}} \lesssim 0.2$ dex). We fit a unity relation to the primary calibration sample (solid black line) and use this line as L$_{\mathrm{fit}}$ to determine residuals of expected L$_{\mathrm{PAH}}$ values (bottom for each panel). We used this fit to determine a SFR relation for L$_{\mathrm{PAH}}$ and each PAH feature shown individually (see § 3.4.1). The blue point enclosed by a black circle denotes II Zw 096, see § 3.4.4. 82

3.7 — A histogram of the ratio of L_{PAH}/L_{fit}, where L_{fit} is the unity relation to the star-forming galaxies shown in figure 3.6, demonstrating the scatter in the sample and consistency of L_{PAH} as a SFR indicator in comparison to dust-corrected Hα for the 6.2μm (top right), 7.7μm (bottom left), 11.3μm (bottom right) PAH features individually and L_{PAH} (top left). The bin size used is 0.1 log L_{PAH}/L_{fit} and N_{gal} represents the number of galaxies in each bin. We fit a gaussian distribution to determine the standard deviation of the scatter (σ_{gauss}, shown in plot) and calculated the median absolute deviation (σ_{MAD}, shown in plot) detailed in Beers et al. (1990) to accurately represent the uncertainty of $L_{PAH,\lambda}$ as a SFR indicator. 85

3.8 — The (Top) panel shows the same metallicity distribution for the star-forming galaxies in the calibration sample as figure 3.4. The (Bottom) panel shows the L_{PAH}/L_{fit} ratios for the star-forming galaxies as a function of oxygen abundance. This shows how the low metallicity galaxies result in weaker observed PAH emission than expected from the correlation. For the corrections to the PAH luminosity we used galaxies with $12 + \log(O/H)_{N2} \leq 8.55$. We determined a correction to the PAH luminosity by fitting a line (solid black line) for the galaxies below Z_0 ($Z_0 = Z_\odot - 8.55$ = -0.14) and extrapolations (dashed black lines) beyond the sample limit (low end) and the fit (high end, see § 3.4.3 for more details). The blue point enclosed by a black circle denotes II Zw 096, see § 3.4.4. 88

3.9 — SFRs for the application sample (labeled on the vertical axis with the galaxy's name) as given in table 3.5. We indicate the different SFR indicators as Paα, Brα and all the PAH features with green, red and black lines, respectively for the range in uncertainty of the estimated SFRs. The estimated PAH SFRs agree closely to each other as well as the other SFR indicators for most of these galaxies. In all cases, we do not increase the PAH SFRs for effects of low metallicity (see, e.g., § 3.6.2). 99

3.10 — The estimated SFRs from the PAH 7.7 μm in comparison to the estimated Paα (open black circles) and Brα (open red circles) SFRs for the application sample (some of the statistical uncertainties are smaller than the symbol size, primarily for the vertical axis; see § 3.6 for discussion). The line shown is the unity PAH 7.7 μm SFR relation from our calibration sample (§ 3.4.1) to the Paα and Brα SFR relations. Excluding the galaxies with upper limits or uncertainties larger than the measured fluxes (A2667a, The Clone and cB58) the galaxies lie along the relation for both SFR indicators to that of the PAH 7.7 μm SFR. Furthermore the galaxies (A2218b and A1835a) both show possible indications of an AGN, which would potentially cause an overestimation of their Paα and Brα SFRs resulting in a shift left back to the SFR relations, illustrating the robustness of the PAH SFRs. 100

4.1 — In both panels, we show fits from the spectral decomposition code PAHFIT with our modifications to fit the silicate emission seen in the quasar sample from Shi et al. (2014). The open circles are the measured flux densities from the *Spitzer*/IRS data observations with error bars representing the uncertainties in those measurements and the green line represents the best fit from spectral decomposition of PAHFIT. The (Left) panel shows the best fit for a galaxy with silicate emission near our limit for reliable continuum fits with PAHFIT (9.7μm silicate strength = 0.17, see § 4.3.1). The (Right) panel shows the best fit for a galaxy with strong silicate emission beyond our limit for reliable continuum fits with PAHFIT (9.7μm silicate strength = 0.39, see § 4.3.1). 114

4.2 — In both panels, we show the total IR luminosity against the PAH luminosity (PAH SFR) for each sample (O'Dowd et al., 2009; Shipley et al., 2013; Shi et al., 2014, green squares, blue diamonds and black circles, respectively), where the magenta stars are the median values for each sample. The (Left) panel is the PAH luminosity from the three brightest PAH features (6.2μm, 7.7μmand 11.3μm), L_{PAH}. The (Right) panel is the PAH luminosity from the 11.3μm feature alone, which has been shown to be a better tracer of star-formation in galaxies with AGN (see § 4.4.1). 117

4.3 — The contribution of star-formation to the total IR luminosity as a function of the total IR luminosity. In both panels, we show the different star-formation contributions for each sample of O'Dowd et al. (2009, green sqaures), Shipley et al. (2013, blue diamonds) and Shi et al. (2014, black circles). The (Left) panel is for total PAH luminosity, L_{PAH}, where we see lower luminosity galaxies following the trend seen by Bell (2003) for IR excess emission (red dashed line) that lowers the star-formation contribution. The (Right) panel for the 11.3 μm feature follows the same trend but not as significantly as L_{PAH} for the lower SFRs at lower IR luminosities. The median values for the samples, in both panels, are given in § 4.4.1. This clearly shows a trend for decreasing contribution from star-formation with increasing IR luminosity. Furthermore, the contribution from star-formation during the quasar phase is significantly less than galaxies at similar IR luminosities. 119

4.4 — PAH SFRs for the O'Dowd et al. (2009) sample (green squares), the Shipley et al. (2013) sample (blue diamonds) and the Shi et al. (2014) sample (black circles) estimated from L_{PAH} and the 11.3μm feature only. The SFRs span three orders of magnitudes from 0.1 to 300 $M_{\odot}$ yr^{-1}. The dashed black line represents a unity relation between the two SFR indicators. 121

4.5 — SFRs for the quasars only from the Shi et al. (2014) sample estimated from L_{PAH} (Left) panel and the 11.3μm feature only (Right) panel. The SFRs span three orders of magnitudes from 0.1 to 200 $M_{\odot}$ yr^{-1} but the median and peak of the SFR in both panels is $\sim$10 $M_{\odot}$ yr^{-1}. 122

4.6 — In both panels, the top gives the total IR luminosities of the quasars from Shi et al. (2014) sample (interquartile range of $1 - 6 \times 10^{11}$ $L_{\odot}$. The bottom of each panel is the relation between the SFR (i.e. luminosity of star-formation) and the total IR luminosity ($L_{SF} \propto L_{IR}^{\beta}$) and as the star-formation only contributes $\sim$10% roughly the total AGN luminosity for quasars ($L_{SF} \propto L_{AGN}^{\beta}$). This demonstrates for increasing total IR luminosity the SFR increases. The best fit slope for this relation is $\beta = 0.71 \pm 0.10$ for L_{PAH} (Left) panel and $\beta = 0.88 \pm 0.14$ for 11.3μm feature (Right) panel for L_{IR}. If we remove the contribution from star-formation to the L_{IR} (i.e. L_{AGN}) we get a best fit slope of $\beta = 0.67 \pm 0.10$ for L_{PAH} and $\beta = 0.55 \pm 0.15$ for the 11.3μm feature, consistent with previous estimates of this relation (see § 4.5.1 for more detail). 124

A.1 — The IR luminosities derived from the 24μm data only $L_{IR}(24\mu m)$ compared to the L_{IR} derived using multiple MIPS bands (24μm, 70μm and/or 160μm) for each of the three sets of IR SED models (Chary & Elbaz, 2001; Dale & Helou, 2002; Rieke et al., 2009, as labeled in each panel). The dashed line represents a unity relation between the two L_{IR} estimates. Sources with only 24μm flux densities are not plotted. 158

LIST OF TABLES

TABLE Page

2.1 Galaxy Classifications and Locations 13

2.2 Fitted Fluxes of the Most Prominent PAH Emission Features 21

2.3 Fitted Fluxes of the Most Prominent Atomic Emission Lines 23

2.4 Emission Feature Detection Frequencies 34

2.5 Equivalent Widths for Various PAH Emission Features 42

3.1 Optical Fluxes and BPT Classification for Shipley et al. (2013) Sample 71

3.2 Unity PAH Luminosity SFR Relations 83

3.3 Linear PAH Luminosity SFR Relations 84

3.4 Metallicity Corrections 87

3.5 Application Sample SFRs 98

1. INTRODUCTION

The variation in stellar content over a wide range in young stellar objects and star-formation activity is the foundation for the Hubble classification (Hubble, 1926), which is one of the most recognizable features of galaxies. Understanding the physical conditions and origins of the Hubble sequence is fundamental to understanding galaxy evolution in its greater context. The review of Kennicutt (1998) dealt with the global star-formation properties of galaxies, the systematics of those properties along the Hubble sequence, and their implications for galactic evolution. This picture required the development of accurate and more precise diagnostics to quantify the global star-formation rates (SFRs) in galaxies.

As the gas reservoir in a galaxy is depleted by the process of star-formation, the gas must be replenished by infall from the surrounding environment known as the intergalactic medium (IGM) to support prolonged star-formation or many epochs of starbursts. When the more massive stars from this ongoing star-formation die, these massive stars enrich the surrounding interstellar medium (ISM) of a galaxy with heavy metals, through supernovae explosions or expelling mass in strong stellar winds and results in a galaxy's chemical composition being altered. Therefore, star-formation needs to be accurately traced across cosmic time to give important constraints for how galaxies form and evolve (e.g., Tinsley, 1968; Somerville et al., 2012; Madau & Dickinson, 2014, and references therein).

For decades, significant work has been applied to calibrating emission from the ultra-violet, nebular emission lines, far-infrared (far-IR), X-ray and radio as tracers of the SFR in distant galaxies (see the review by Kennicutt & Evans, 2012). As discussed in Kennicutt (1998), activity in this field has been stimulated in large part

by two major discoveries. The first was the discovery of a large population of ultra luminous IR starburst galaxies (i.e. ULIRGs) by the Infrared Astronomical Satellite (IRAS) in the mid-1980s. IRAS revealed the universality of the phenomenon and the extreme nature of these most luminous objects. The latest burst of interest in the field has been motivated by the discovery of star-forming galaxies at high redshift (very distant galaxies, Steidel et al., 1996; Ellis, 1997). This makes it possible to apply the locally calibrated SFR diagnostics to distant galaxies and to develop new SFR diagnostics using these high redshift galaxies. This result allows us to directly trace the evolution of the SFR density and the Hubble sequence with cosmological lookback time. That is, because of the finite speed of light, observing galaxies at large distances is equivalent to looking back in time to the early history of the Universe.

Understanding the exact rate of star-formation and how it evolves with time and galaxy mass has deep implications for how galaxies form. The co-evolution of star-formation and supermassive black hole (SMBH) accretion is one of the key problems in galaxy formation theory. This relation is important for understanding why at present the mass in galaxy bulges (on scales of kpc) correlates so tightly with the mass of galaxy central SMBHs (on scales of AU). Because the mass of the SMBH does not correlate with mass of galaxy disks or galaxy dark-matter halos, there is a now wide-spread belief that SMBHs and galaxy bulges co-evolve by regulating each others growth. Did bulge formation proceed the formation of black holes, or vice versa, or are they contemporaneous or even unrelated?

The formation of a prominent bulge appears to be the driving reason for the quenching of star-formation in galaxies. As illustrated in a growing number of studies (e.g., Franx et al., 2008; Wuyts et al., 2011; Bell et al., 2012; Papovich et al., 2012), galaxies with large bulges have the lowest relative SFRs, and galaxies with pure disks have high relative SFRs. The reasons for this relation are not understood, but

many theoretical models now attribute the cessation of star-formation in galaxies to feedback from accreting SMBHs (i.e., quasi-stellar objects, QSOs Springel et al., 2005), which may expel cold gas from the galaxies altogether, shutting off the fuel for further star-formation and SMBH growth. This feedback mechanism and the physical processes that drive it are among the most active areas of astrophysical research, and significant questions remain. Understanding them is paramount for understanding galaxy evolution itself. But, many of these SFR indicators discussed above are influenced by SMBH accretion in galaxies and result in unreliable SFRs.

We present results from a multistage study of the star-formation and SMBH accretion in galaxies (i.e. Active Galactic Nuclei) at moderate redshifts. Utilizing the luminous polycyclic aromatic hydrocarbon (PAH) emission features, we will address two key problems in galaxy evolution (1) measuring reliable SFRs in galaxies that host Active Galactic Nuclei (AGN) and (2) how star-formation and AGN co-evolve in galaxies. In § 2, we will discuss my work in studying the diagnostics of star-formation and AGN from mid-IR spectroscopy. In § 3, we will discuss my work in quantifying the relation between PAH luminosity and the SFR, and application of this calibration to high redshift galaxies. In § 4, application of the PAH SFR calibration to galaxies of varying AGN activity (from starburst to quasars, luminous AGN) to give valid SFRs to address these questions. In § 5, we conclude by summarizing the important results from this multistage study and give future considerations that must be addressed.

2. DIAGNOSTICS OF AGN AND STAR-FORMATION AND THE IMPORTANCE OF PAH EMISSION USING SPITZER SPECTROSCOPY OF INFRARED-LUMINOUS GALAXIES*

2.1 Background

The mid-IR (3-19μm) spectrum of star-forming galaxies is dominated by strong emission features often associated with polycyclic aromatic hydrocarbons (PAHs). PAH molecules are made up of tens to hundreds of carbon atoms in planar lattices that typically are several Å in diameter (Leger & Puget, 1984; Allamandola et al., 1985). Specifically, each PAH band is identified with specific carbon-carbon (C-C) and carbon-hydrogen (C-H) bending and stretching modes (Allamandola et al., 1989). Their vibrational modes are excited by efficient absorption of UV and optical photons whose energy is re-emitted in the IR. In many galaxies, the emission of young stars and active galactic nuclei (AGN) is almost entirely absorbed by dust and re-emitted in the IR; PAHs must then be used for detailed diagnostics of the luminosity sources.

The luminosity in the mid-IR PAH emission bands is very strong for galaxies with ongoing star-formation. The total PAH emission can contribute as much as 20% of the total IR luminosity and the 7.7μm PAH band may contribute as much as 50% of the total PAH emission (e.g., Smith et al., 2007). Certain PAH bands are made up of several dust emission features (e.g., 7.7μm, 8.6μm, 11.3μm, 12.7μm, and 17.0μm PAH bands) and so we will use the general term "feature" to describe the PAH emission bands.

*Reprinted with permission from "Diagnostics of AGN and Star-Formation and the Importance of PAH Emission Using Spitzer Spectroscopy of Infrared-Luminous Galaxies" by Shipley et al., 2013. ApJ, 769, 75, Copyright 2013 by ApJ.

From laboratory experiments, models of stochastic heating of dust grains predict that the relative strengths of PAH features are dependent on the size distribution of PAH grains and the ionization state of the PAH molecules (Schutte et al., 1993; Draine & Li, 2001). Although the detailed physics is not well understood, existing models do explain the general trends observed for the various PAH features.

Previous *Spitzer* studies (Diamond-Stanic & Rieke, 2010; O'Dowd et al., 2009; Smith et al., 2007) have found trends between the ratios of the various PAH features and galaxy properties, such as AGN activity and star formation history. A tendency for active galaxies to have lower ratios of the 6-8μm PAH features relative to the 11.3μm PAH feature has been reported both by O'Dowd et al. (2009) and Smith et al. (2007). Smith et al. argued that AGN are able to modify the PAH grain size distribution or are able to excite the emission of larger PAH molecules. O'Dowd et al. interpreted their results as being consistent with the destruction of smaller PAH grains by shocks or X-rays associated with the AGN, but were unable to determine a difference between AGN-dominated and AGN–starforming composite sources. Diamond-Stanic & Rieke (2010) chose a sample of local Seyfert galaxies to explore the effects of AGN on PAH emission. They found similar results to the previous studies when observing the AGN-dominated nuclear regions of galaxies, and determined AGNs do not excite PAH emission. In contrast, off-nuclear (presumably) star-forming regions in the galaxy disks had 7.7-to-11.3μm PAH ratios similar to those of star-forming galaxies in studies from the literature.

Here, we extend studies of IR luminous galaxies with mid-IR spectroscopy to higher redshifts and higher luminosities. Specifically, we focus on galaxies that have high IR luminosities ($> 10^{11}\mathrm{L}_{\odot}$) and moderate redshifts ($z \lesssim 0.6$). This allows us to study the nature of the IR emission in galaxies at the same redshift range and IR luminosity range that dominate the IR luminosity density at high redshifts ($z \sim 1$

Le Floc'h et al., 2005). By observing the mid-IR spectral features of these galaxies we can therefore study the ionization state of the IR emission, and study how both star-formation and AGN contribute to the IR luminosity in these objects.

An additional goal of our study is to understand if there is a correlation (causal or otherwise) between the IR-active stages involving star-formation and/or AGN and other galaxy properties, such as their optical color. At a basic level the optical color depends on the galaxies' star-formation histories (galaxies with recent star-formation have bluer optical colors, and passive galaxies lacking any recent star-formation form a well documented "red sequence" e.g., Bell et al., 2004; Blanton et al., 2003; Faber et al., 2007). Studies of the optical colors of galaxies with high IR-luminosity (as measured by their MIPS 24μm emission) show they span a wide range of optical color from the blue star-forming galaxies, through the "green valley", and up to the blue edge of the red sequence (Bell et al., 2005; Mendez et al., 2013). This highlights a dependency of galaxy colors on IR activity. Wyder et al. (2007) show that the sequence of star-forming galaxies becomes redder with increasing optical luminosity, which is presumably a result of increased dust obscuration. This implies that stages of increased dust obscuration in luminous galaxies may be a precursor to the cessation of star-formation in galaxies as they migrate through the "green valley" to the quiescent red sequence (Faber et al., 2007), and this may be related to quenching by the presence of an AGN (Bundy et al., 2008; Nandra et al., 2007; Schawinski et al., 2007, 2010). Because IR-luminous galaxies have optical colors that span from the star-forming sequence to the red-sequence, there may be a relationship between their excitation mechanism (star-formation versus black hole accretion) and their optical color (Bell et al., 2005; Chen et al., 2010; Nandra et al., 2007).

To date samples of IR-luminous with mid-IR spectroscopy have been heterogeneous or incomplete in their coverage of galaxies over the full range of optical color.

For our study, we allow for changes in the mid-IR spectral features as a function of optical color in galaxies by using a sample of IR-luminous galaxies that is selected to have a uniform distribution in rest-frame $(u-r)_{0.1}$[1] color. In sections 2.2 and 2.3, we describe our sample selection and ancillary data. In section 2.4, we describe our *Spitzer* IRS observations, data reduction, and analysis of the IRS spectra. In section 2.5, we describe our measurements of the total IR luminosity and discuss correlations between the PAH emission and emission from other atomic lines. In section 4.5, we discuss the color-magnitude relation for IRAGN, AGN effects of PAH emission, and the significance of [O IV] emission. In section 5, we present our conclusions. The ΛCDM cosmology we assume is $H_0 = 71$ km s^{-1} Mpc^{-1}, $\Omega_m = 0.27$, and $\Omega_\lambda = 0.73$ throughout this section.

2.2 Sample Definition and Selection

Our main goal is to compare the mid-IR spectral properties of AGN and star-forming (SF) galaxies in luminous IR galaxies (LIRGs) out to moderate redshifts ($z \lesssim 0.6$). To accomplish this goal, we must be sensitive to the fact that both AGN and IR-luminous star-forming galaxies are known to span a broad range in optical color (see section 4.1). As discussed above, the energetics of both obscured AGN and star-forming galaxies may affect both the mid-IR spectral properties and the optical color. To avoid any bias related to these effects, we therefore built a sample of IR-luminous galaxies for spectroscopy that span an approximately uniform distribution of $(u-r)_{0.1}$ optical color that spans the full range from the blue, star-forming sequence to the red, quiescent sequence.

We built our primary sample for IRS spectroscopy using the AGN and Galaxy

[1]Note that throughout, $(u-r)_{0.1}$ and $M(r)_{0.1}$ are the rest-frame color and absolute magnitude observed at z=0.1 (as used extensively in the SDSS literature, see, e.g., Blanton et al., 2003). Furthermore, throughout, $M(r)_{0.1}$ and $(u-r)_{0.1}$ are measured in AB magnitudes (Oke & Gunn, 1983).

Evolution Survey (AGES, Kochanek et al., 2012). This survey provides deep ($I < 20$ mag) spectroscopy covering the $\sim$10 deg^2 Boötes field, which includes deep optical imaging from the NOAO Wide Deep-Field Survey (NWDFS) (Jannuzi & Dey, 1999). The field was also covered with *Spitzer*/IRAC imaging at 3.6–8.0 μm as discussed in Ashby et al. (2009), and with MIPS imaging at 24–160 μm first with shallow coverage by Houck et al. (2005) and subsequently with much deeper coverage as part of MIPS AGES (MAGES) survey (PI: B. Januzzi). The spectroscopy, optical, and mid-IR imaging allows us to select IR-luminous galaxies out to moderate redshift and over the full range of $(u-r)_{0.1}$ optical color.

As our parent sample, we selected 498 galaxies from the AGES data with spectroscopic redshifts $0.2 < \mathrm{z} < 0.6$, and $f_\nu(24\mu\mathrm{m}) > 1.2$ mJy. We then searched the *Spitzer* archive for programs that had previously targeted galaxies in our parent sample with IRS spectroscopy. Two programs satisfied our needs and included *Spitzer*/IRS data for a total of 17 galaxies from PID 20113 (PI: H. Dole) and 38 galaxies from PID 20128 (PI: G. Lagache); to our knowledge the data from these programs have not been published previously.

We supplemented the archival IRS spectroscopy with new IRS observations of additional galaxies taken as part of the MIPS guaranteed time observations (GTO) 40251 (PI: G. Rieke) to ensure that our full IRS sample includes galaxies with an approximately uniform distribution in $(u-r)_{0.1}$ color. To identify the sample for GTO observations, we derived bins in $(u-r)_{0.1}$ optical color that run roughly parallel to the red sequence, which has some slope in the color-magnitude plane:

$$(u-r)_{0.1} + 3/50 \times (M[r]_{0.1} + 20) > 2.39$$

$$2.39 \geq (u-r)_{0.1} + 3/50 \times (M[r]_{0.1} + 20) > 2.18$$

$$2.18 \geq (u-r)_{0.1} + 3/50 \times (M[r]_{0.1} + 20) > 1.73$$

$$(u-r)_{0.1} + 3/50 \times (M[r]_{0.1} + 20) \leq 1.73,$$

We require at least 12 galaxies in each of these color bins. As shown in figure 2.1, this required new IRS observations of 14 additional galaxies from our GTO allocation in PID 40251.

The combined archival IRS data (7 + 19 galaxies) and new IRS data (14 galaxies) yield a sample of 40 galaxies that form our primary IRS sample. In addition, the archival programs used here include 29 additional galaxies, either at lower redshift ($0.02 < z < 0.2$; 12 galaxies) or from the *Spitzer* First Look Survey (FLS; 17 galaxies), or both. These galaxies appear to all be selected using a 24 μm flux limit ($f_\nu(24\mu\text{m}) > 1.2$ mJy). We included these galaxies as a secondary sample here because our sample is increased by $\sim$70% and it enables us to extend our observations to both lower-luminosity objects (in the case of the objects at $0.02 < z < 0.2$) and adds higher luminosity objects from the FLS (even though these have no $(u-r)_{0.1}$ color information). As discussed in section 2.4.2, we ultimately exclude four observations (two from AGES and two from the FLS) that showed contamination from a serendipitous source in the IRS slit. Therefore, our full sample of primary and secondary sources includes 65 galaxies with $f_\nu(24\mu\text{m}) > 1.2$ mJy and $0.02 < z < 0.6$.

In summary, we have three samples defined in this paper.

- Full Sample. All 956 galaxies with $f_\nu(24\mu\text{m}) > 1.2$ mJy and redshift of 0.02

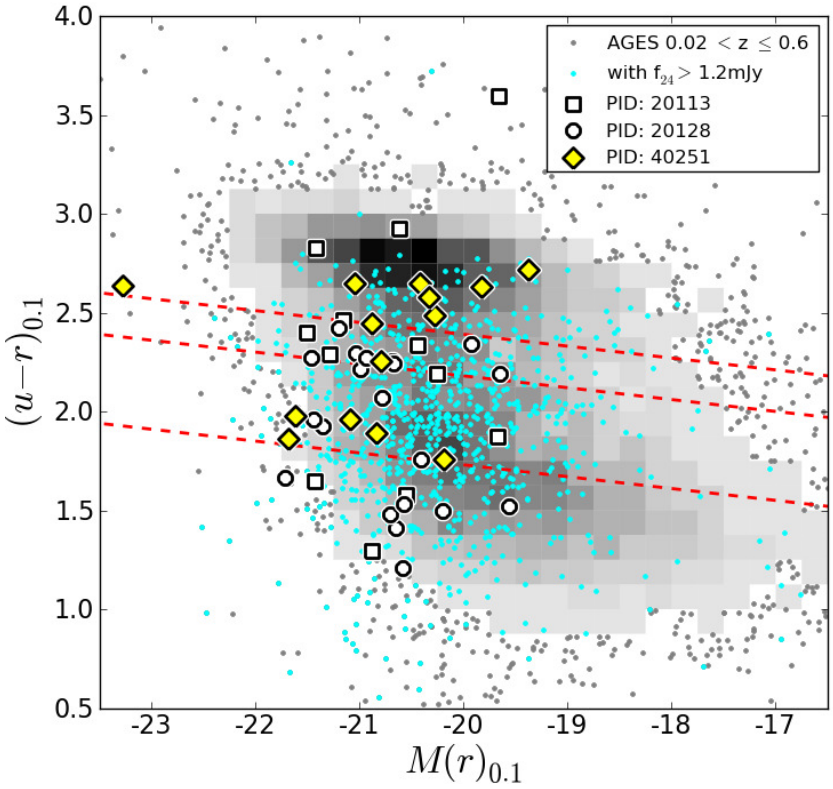

Figure 2.1 — Color-Magnitude Diagram using optical data from the AGES catalog for our sample. The grey-shading indicates the density of all galaxies from AGES in that region of color-magnitude space and $0.02 < z < 0.6$, where the grey-shading increases as the density increases linearly. The cyan points show those AGES sources with $0.02 < z < 0.6$ and $f(24\mu\text{m}) \geq 1.2$ mJy, the IRS spectroscopic limit for our sample. The galaxies selected in our sample are indicated by white squares, white circles, and yellow diamonds for Dole (program 20113), Lagache (program 20128, non-FLS sources), and Rieke (program 40251), respectively. Furthermore, we selected IR-luminous galaxies for our sample such that they span the full range of $(u-r)_{0.1}$ optical color with an equal number (12-13) galaxies in each of four bins, denoted by the red-dashed lines and defined in section 2.2.

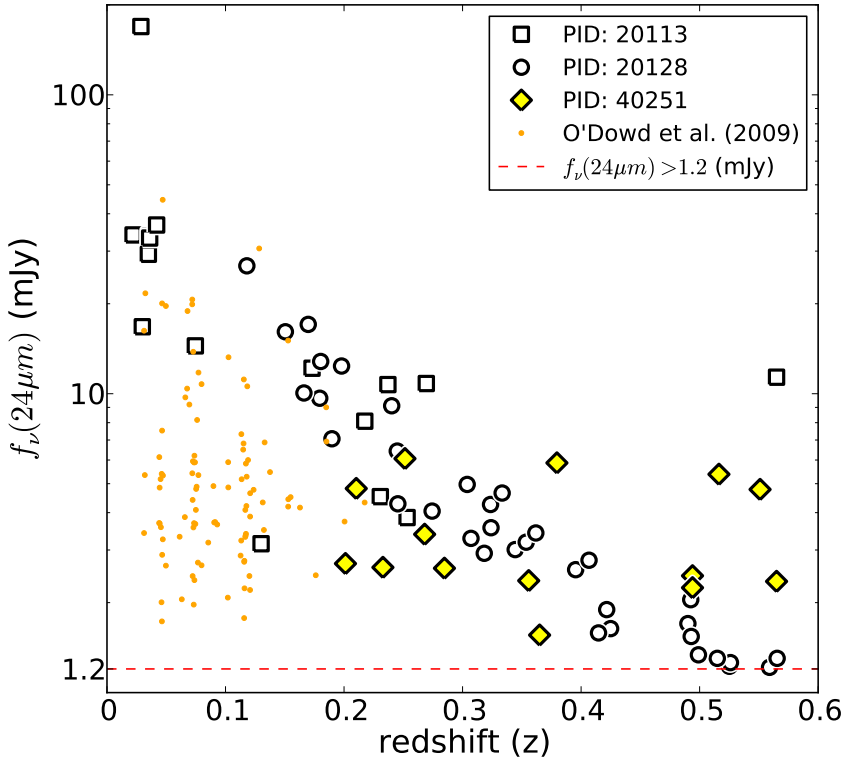

Figure 2.2 — Distribution of the redshifts and 24μm flux densities of the 65 galaxies in our IRS sample. The galaxies are indicated by white squares, white circles, and yellow diamonds for Dole (program 20113), Lagache (program 20128), and Rieke (program 40251), respectively. The orange circles are from O'Dowd et al. (2009) sample as a comparison to our sample. The red dashed line indicates $f_\nu(24\mu\text{m}) = 1.2$mJy. The redshift mean and median of the distribution are 0.30 and 0.28, respectively. The redshift distribution is fairly uniform from $0.2 < z < 0.6$, with an interquartile range (which contains the inner 50% of galaxies) of $z_{\text{interquartile}} = 0.18 - 0.42$.

$< z < 0.6$ in AGES.

- Parent Sample. All 498 galaxies with $f_\nu(24\mu\text{m}) > 1.2$ mJy and redshift $0.2 < z < 0.6$, from which targets for new IRS observations were selected.

- IRS Sample. The 65 galaxies with $f_\nu(24\mu\text{m}) > 1.2$ mJy that have IRS spectroscopy either from archival data (51 galaxies) or our new GTO observations (14 galaxies).

Figure 2.1 shows the $(u-r)_{0.1}$–$M(r)_{0.1}$ color-magnitude diagram for all the galaxies in AGES in the redshift range of our full sample, and indicates the galaxies in the redshift range with ($f_\nu(24\mu\text{m}) > 1.2$ mJy (956 galaxies). The figure shows that the existing galaxies from the *Spitzer* archival programs (non-FLS galaxies) are biased toward IR-luminous galaxies with blue colors compared to the AGES sample and the sample of GTO observations help to uniformly distribute the galaxies in $(u-r)_{0.1}$ color. The properties of our sample are listed in table 2.1 and figure 2.2 shows the redshift and 24μm flux density distributions.

Table 2.1. Galaxy Classifications and Locations

ID	AOR	R.A.	Dec.	z(opt)	z(IRS)	f(24μm) [mJy]	f(70μm) [mJy]	f(160μm) [mJy]	L(IR)$_{\rm R}$ [10^{10}L$_\odot$]	AGN
1	14127872	14h25m00.18s	+32d59m50.0s	0.296	0.304	4.97 ± 0.02	60.7 ± 1.09	...	31.9	
2	21757184	14h25m27.91s	+33d47m47.0s	0.509	0.516	5.38 ± 0.02	17.4 ± 1.38	...	94.6	Y
3	14129920	14h25m44.96s	+33d37m05.0s	0.321	0.344	3.01 ± 0.01	...	...	24.8	Y
4	14087680	14h25m52.68s	+34d02m40.1s	0.562	0.565	11.36 ± 0.02	258.2 ± 1.03	413.0 ± 1.12	268.	Y
5	14133248	14h26m07.93s	+34d50m45.0s	0.405	0.407	2.77 ± 0.01	47.5 ± 1.09	143.9 ± 1.21	39.0	
6	14133504	14h26m18.65s	+34d57m03.0s	0.418	0.415	1.58 ± 0.01	...	...	35.8	
7	14084352	14h26m23.88s	+32d44m35.8s	0.171	0.173	12.17 ± 0.02	304.1 ± 1.03	474.2 ± 1.04	31.1	Y
8	14126080	14h26m59.13s	+33d33m05.0s	0.150	0.150	16.12 ± 0.19	178.6 ± 1.25	...	22.9	
9	21758464	14h27m44.37s	+34d29m08.2s	0.365	0.365	1.56 ± 0.01	109.4 ± 1.06	234.4 ± 1.12	59.1	
10	21758208	14h27m50.32s	+35d04m51.2s	0.211	0.210	4.82 ± 0.01	87.1 ± 1.07	206.1 ± 1.15	17.2	
11	14132480	14h28m19.51s	+33d51m50.0s	0.488	0.490	1.70 ± 0.01	22.3 ± 1.24	101.9 ± 1.24	53.4	
12	14132992	14h28m19.57s	+34d23m34.0s	0.474	0.493	2.05 ± 0.01	18.9 ± 1.22	...	54.0	Y
13	14086144	14h28m49.79s	+34d32m40.2s	0.216	0.218	8.09 ± 0.03	253.5 ± 1.04	598.4 ± 1.06	47.5	
14	14132736	14h29m19.77s	+34d15m06.0s	0.424	0.425	1.64 ± 0.01	23.3 ± 1.16	92.7 ± 1.26	37.9	
15	14132224	14h29m35.97s	+33d37m13.0s	0.419	0.422	1.90 ± 0.01	33.3 ± 1.17	131.8 ± 1.20	38.8	
16	21758720	14h29m50.66s	+35d08m42.7s	0.366	0.380	5.87 ± 0.01	19.2 ± 1.25	...	53.8	Y
17	21755648	14h29m51.38s	+32d50m36.0s	0.270	0.268	3.39 ± 0.01	19.1 ± 1.22	...	16.8	Y
18	14129408	14h30m00.39s	+35d38m14.0s	0.240	0.240	9.11 ± 0.02	125.3 ± 1.06	146.9 ± 1.15	28.0	
19	21756672	14h30m19.82s	+33d40m47.2s	0.231	0.233	2.62 ± 0.01	44.9 ± 1.15	97.3 ± 1.21	11.4	
20	14082304	14h30m24.46s	+32d56m16.4s	0.042	0.042	36.68 ± 0.15	483.1 ± 1.04	824.1 ± 1.08	4.56	
21	14086400	14h31m14.77s	+33d46m23.0s	0.230	0.231	4.53 ± 0.03	153.5 ± 1.09	347.5 ± 1.07	31.1	
22	14081792	14h31m19.76s	+35d34m18.0s	0.034	0.036	33.58 ± 0.11	537.0 ± 1.03	691.8 ± 1.06	3.11	
23	14082048	14h31m21.12s	+35d37m21.8s	0.035	0.036	33.18 ± 0.46	1318.3 ± 1.04	2779.7 ± 1.04	11.4	
24	14130432	14h31m21.88s	+34d40m46.0s	0.348	0.354	3.19 ± 0.01	17.1 ± 1.20	...	27.4	Y
25	14080768	14h31m25.43s	+33d13m49.7s	0.022	0.022	33.98 ± 0.54	794.3 ± 1.06	1011.6 ± 1.07	2.04	
26	21756160	14h31m33.98s	+33d45m16.0s	0.490	0.494	2.46 ± 0.01	22.8 ± 1.22	...	54.4	Y
27	14081536	14h31m56.23s	+33d38m33.1s	0.034	0.035	29.27 ± 0.50	...	...	1.67	
28	14083840	14h32m28.36s	+34d58m38.8s	0.129	0.130	3.15 ± 0.02	137.1 ± 1.13	258.8 ± 1.22	7.63	
29	14086912	14h32m34.90s	+33d28m32.3s	0.249	0.253	3.85 ± 0.02	338.8 ± 1.03	395.4 ± 1.09	46.6	
30	14086656	14h32m39.56s	+35d01m51.3s	0.236	0.237	10.73 ± 0.02	236.6 ± 1.03	349.9 ± 1.07	42.9	
31	14131968	14h32m52.49s	+33d11m53.0s	0.401	0.395	2.58 ± 0.01	28.2 ± 1.21	...	32.4	
32	14128128	14h33m26.18s	+33d05m58.0s	0.243	0.245	4.28 ± 0.02	62.1 ± 1.08	119.4 ± 1.21	16.6	
33	21755904	14h33m33.34s	+33d09m22.0s	0.353	0.356	2.37 ± 0.01	...	...	24.9	Y
34	21757440	14h33m42.17s	+34d56m51.0s	0.494	0.494	2.24 ± 0.01	...	...	54.4	
35	14083584	14h34m45.32s	+33d13m46.1s	0.073	0.075	14.46 ± 0.03	288.4 ± 1.03	485.3 ± 1.08	7.01	
36	14130176	14h34m53.85s	+34d27m44.0s	0.329	0.324	3.56 ± 0.01	29.4 ± 1.15	...	25.5	
37	21756416	14h35m00.65s	+33d29m23.0s	0.274	0.285	2.61 ± 0.01	70.0 ± 1.08	140.6 ± 1.16	20.1	
38	14081024	14h35m18.21s	+35d07m08.3s	...	0.029	169.23 ± 3.72	3926.4 ± 1.04	5571.9 ± 1.04	19.7	
39	14130688	14h35m19.42s	+35d36m22.0s	0.316	0.318	2.92 ± 0.01	26.5 ± 1.24	...	20.8	Y
40	21758976	14h35m35.47s	+33d25m44.4s	0.244	0.251	6.07 ± 0.02	104.2 ± 1.06	145.5 ± 1.18	24.9	
41	14134272	14h36m06.84s	+35d09m27.0s	0.525	0.525	1.22 ± 0.01	21.0 ± 1.22	...	63.1	
42	14125824	14h36m19.14s	+33d29m17.0s	0.188	0.190	7.07 ± 0.05	...	...	17.8	
43	14087168	14h36m28.12s	+33d33m58.0s	0.265	0.269	10.82 ± 0.03	223.4 ± 1.04	267.3 ± 1.11	51.0	
44	14128640	14h36m33.16s	+33d48m05.0s	0.218	0.245	6.43 ± 0.02	12.4 ± 1.38	...	25.4	Y
45	14129152	14h36m36.65s	+34d50m34.0s	0.279	0.274	4.05 ± 0.02	39.2 ± 1.12	...	21.0	
46	14081280	14h36m41.23s	+34d58m24.2s	0.030	0.030	16.75 ± 0.25	...	...	0.84	
47	14130944	14h37m11.26s	+35d40m36.0s	0.362	0.362	3.42 ± 0.02	223.9 ± 1.04	236.0 ± 1.16	64.0	
48	21757952	14h37m23.73s	+35d07m35.0s	0.579	0.551	4.78 ± 0.01	30.5 ± 1.15	...	96.2	
49	21757696	14h37m52.92s	+35d32m51.4s	0.563	0.565	2.36 ± 0.01	68.7 ± 1.10	217.3 ± 1.10	101.	
50	21756928	14h38m09.88s	+35d27m37.8s	0.204	0.201	2.70 ± 0.02	31.7 ± 1.15	...	8.74	
51	14127104	17h12m39.64s	+58d41m48.0s	0.165	0.166	10.06 ± 0.13	...	...	18.3	
52	14131712	17h13m08.57s	+60d16m21.0s	0.332	0.333	4.65 ± 0.09	76.2 ± 12.20	...	36.7	
53	14135552	17h14m27.02s	+58d38m36.0s	0.562	0.565	1.30 ± 0.06	...	...	75.6	
54	14127360	17h14m37.44s	+59d56m48.1s	0.196	0.198	12.38 ± 0.14	...	...	30.8	
55	14135808	17h15m25.74s	+60d04m24.0s	0.501	0.499	1.34 ± 0.06	...	...	55.8	
56	14127616	17h15m42.00s	+59d16m57.4s	0.116	0.118	26.78 ± 0.21	...	...	19.7	
57	14126336	17h19m16.60s	+59d34m49.0s	0.166	0.170	17.06 ± 0.17	177.5 ± 27.00	...	30.2	
58	14131200	17h20m25.19s	+59d15m03.0s	0.305	0.307	3.28 ± 0.08	...	...	21.3	

Table 2.1 (cont'd)

ID	AOR	R.A.	Dec.	z(opt)	z(IRS)	f(24μm) [mJy]	f(70μm) [mJy]	f(160μm) [mJy]	L(IR)$_{\rm R}$ [10^{10}L$_\odot$]	AGN
59	14134528	17h20m46.74s	+59d22m23.0s	0.539	0.526	1.26 ± 0.06	...	...	63.4	
60	14134784	17h21m17.75s	+58d51m20.0s	0.512	0.493	1.54 ± 0.06	...	...	54.1	Y
61	14135040	17h21m18.31s	+58d46m01.0s	0.555	0.559	1.22 ± 0.05	...	...	73.5	Y
62	14126592	17h22m20.27s	+59d09m49.0s	0.179	0.179	9.66 ± 0.13	180.4 ± 27.50	...	21.3	
63	14131456	17h23m48.13s	+59d01m54.0s	0.321	0.324	4.26 ± 0.09	...	...	29.9	
64	14126848	17h24m00.61s	+59d02m28.0s	0.178	0.180	12.82 ± 0.14	...	...	26.5	
65	14135296	17h25m03.37s	+59d11m09.0s	0.514	0.515	1.30 ± 0.06	...	...	60.2	

Note. — Optical redshifts [z(opt)] are from the AGES catalog (Kochanek et al., 2012) and Papovich et al. (2006) for FLS sources. IRS redshifts [z(IRS)] are from the fits as discussed in section 2.4.3. The 24μm flux densities are from the AGES catalog (Kochanek et al., 2012) and Papovich et al. (2006) for FLS sources and discussed in sections 2.3.1 and 2.3.2. The 70μm and 160μm flux densities are from MAGES (B. Jannuzi et al., in prep) and discussed in sections 2.3.1 and 2.3.2. $L_{\rm IR}$ values are described in section 2.5.2 and appendix A and the selection of IRAGN in section 2.3.3.

2.3 *Spitzer* Imaging Data

2.3.1 Boötes Field

For our IRS sample, we used observations taken from the Infrared Array Camera (IRAC) and MIPS. IRAC observations were taken from the *Spitzer* Deep Wide-Field Survey (SDWFS) catalog for Boötes sources (Ashby et al., 2009). The sources in our sample had IRAC coverage in all four photometric IRAC bands (3.6μm, 4.5μm, 5.8μm, and 8.0μm). We used the 8.0μm selected SDWFS catalog for the four IRAC band magnitudes (given in the Vega magnitude system) of the Boötes sources.[2]

Since our IRS data were acquired, deeper MIPS data were taken as part of the MIPS AGES (MAGES) program (B. Jannuzi et al., in prep). These data catalogs provide deeper imaging in all three MIPS bands, (24 μm, 70 μm, and 160 μm) in the Boötes field. The MAGES catalogs provide significantly deeper imaging at 70 μm and 160 μm, achieving detections at these wavelengths for many of the sources in our IRS sample.

[2]Throughout we use [3.6], [4.5], [5.8], and [8.0] to denote the magnitudes with respect to Vega measured in each IRAC band, respectively.

Using the MAGES data catalog, we first matched all 50 galaxies (in the AGES Boötes' field) with a $r = 2''$ matching radius at 24 μm. For all galaxies, the IRS integrated 24 μm flux densities (see section 2.4.2) agreed within the measurement errors with those matched to the MAGES 24 μm flux densities. We then used the MAGES matched catalog to obtain 70 μm and 160 μm flux densities for sources in our IRS sample, including 46 galaxies with 70 μm detections and 27 galaxies with 160 μm detections (flux densities given in table 2.1). We use these longer wavelength data to improve our estimates of the total IR luminosity (see section 2.5.2).

2.3.2 Spitzer First Look Survey (FLS)

Sources in our IRS sample from the *Spitzer*/FLS have IRAC and MIPS imaging from programs published in the literature. We used data from the four IRAC channels from the *Spitzer* data archive provided from Lacy et al. (2005). We used the combined FLS catalog to acquire the four IRAC band flux densities of the FLS sources. We converted the flux densities to the appropriate magnitudes (Vega magnitude system), identical to that for the Boötes sources. We use the catalogs of Papovich et al. (2006) and Frayer et al. (2006) to obtain MIPS 24μm flux densities, and MIPS 70μm and 160μm flux densities, respectively.

2.3.3 IRAC AGN Selection

The primary goal of this study is to compare the mid-IR spectral features of IR-luminous galaxies with indications of AGN activity to those without. IR-selected AGN can be identified from "star-forming" IR galaxies because AGN typically show indications of warm ($\sim$1000 K) dust heated by the AGN which produces a characteristic power law continuum through the IRAC channels (e.g., Donley et al., 2012). We take advantage of this color selection here to identify IR-selected AGN using the color selection criteria proposed by Stern et al. (2005). The Stern et al. color selection is

defined using spectroscopic observations of galaxies in the same redshift range as our sample, which makes it appropriate here. This selection is also relatively immune to mis-identification of purely star forming galaxies as AGN over the redshift range of our study (Donley et al., 2008), so this region in the diagram can be re-interpreted to identify galaxies where the AGN makes a substantial contribution to the mid-IR output but is not totally dominant (Mendez et al., 2013). We show the result of this selection on our IRS spectroscopic sample in figure 2.3.

We define the subsample of galaxies in our IRS sample that satisfy this IRAC color-color selection as IRAGN. This includes 14 out of the 65 galaxies in our IRS sample (2 are in the FLS sample and 12 are in the AGES Boötes sample). Based on the statistics from Stern et al. (2005), it is unlikely that our IRAGN subsample contains any star-forming galaxies for the AGES sample. It is likely, however, that our subsample of IRAGN is incomplete for all AGN in our sample. Furthermore, the number of AGN dominated galaxies in our sample may be biased towards a higher fraction because of our 24μm selection criteria. For the remainder of this paper we refer to galaxies in our sample satisfying this selection as IRAGN, and the other galaxies in our sample as non-IRAGN. We expect the non-IRAGN subsample to be dominated by star-forming galaxies even though some will have an AGN.

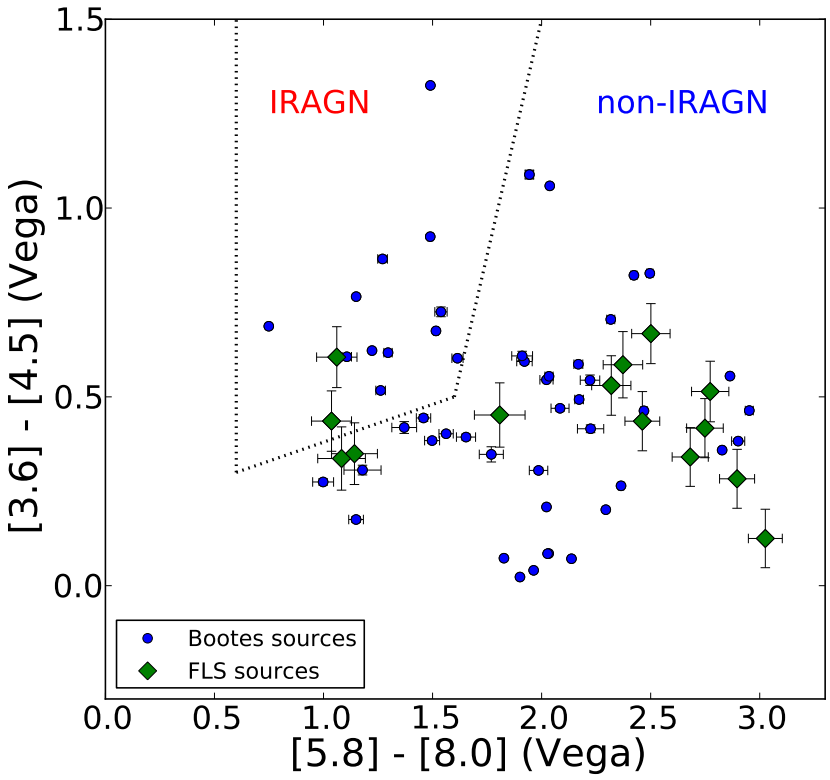

Figure 2.3 — IRAC colors of [5.8] - [8.0] versus [3.6] - [4.5] for galaxies in our IRS sample. Here, the IRAC colors are in the Vega magnitude system, following Stern et al. (2005). The blue circles are sources from the Boötes field and green diamonds are FLS sources. The dotted lines show the empirical selection-criteria for IRAC-AGN selection: galaxies inside this "wedge" are IRAC-selected AGN (Stern et al., 2005). We denote the subsample of galaxies in our IRS sample that satisfy these colors as IRAGN. We denote galaxies outside this wedge as non-IRAGN, and we expect the IR emission in these objects to be dominated by star-formation.

2.4 IRS Observations, Data Reduction, and Analysis

2.4.1 IRS Observations

The IRS was used in staring mode to make the observations with both the low-resolution short-low (SL) and long-low (LL) IRS modules, giving 5.2-38.0μm coverage (SL $\sim$ 5.2-14μm and LL $\sim$ 14-38μm) with resolving power of $\sim 60 - 125$. Exposure times were estimated based on the 24 μm flux densities and the purpose of the individual programs. Observing times ranged from 360-600 seconds for the SL observations and 180-3600 seconds for the LL observations. The SL and LL modules have respective slit widths of $\sim$3.7" and $\sim$10.5", the slits have physical sizes of 1.5-25 kpc and 4.3-70 kpc respectively, over the redshift range of the sample ($0.02 < z < 0.6$). At the median redshift, the physical slit sizes are 16 kpc and 45 kpc, respectively.

2.4.2 Data Reduction

We used the two-dimensional *Spitzer* data products processed by the *Spitzer* Pipeline version S18.7.0 to perform the standard IRS calibration. Our post-pipeline reduction of the spectral data started from the pipeline products basic calibrated data (bcd) files. To perform sky subtraction, we created a sky frame for each object by taking the median of all the images for a single object at the same nod position. We subtracted this image from the frames for the other nod position for the object to produce sky subtracted images. We combined all sky subtracted images for each object at a given nod position to produce coadded 2-dimensional images. We used IRSCLEAN (v.1.9) on each image to remove and correct for bad and rogue pixels.

We used the *Spitzer* IRS Custom Extractor (SPICE) software to extract one-dimensional spectra for each order at each nod position. We chose to use the optimal extraction with point-source calibration because it improved the signal-to-noise (S/N) ratios for our sources. We combined the 1D spectra manually using a weighted

mean for the nod position for each order. We combined the SL2 + SL1 orders (for the 25 sources with SL2 data) and LL2 + LL1 orders (for all sources).

To combine the SL and LL orders we took care to match the flux calibration, accounting for light lost outside the spectroscopic slits (which varies considerably between SL and LL, see above). We integrated the IRS spectra from the SL module with the IRAC 5.8μm and the IRAC 8.0μm transmission functions, and we integrated the spectra from the LL module with the MIPS 24μm transmission function. We took the ratio of the observed flux density as measured directly from the IRAC and MIPS observations to the flux density synthesized from the IRS spectra as an aperture correction (although other effects may contribute to variations in the IRS flux density) for each spectrum, with mean corrections of 1.55, 0.98, and 1.12 for IRAC 5.8μm, IRAC 8.0μm, and MIPS 24μm respectively. We combined (using a weighted mean, weighting by inverse variance) the flux-corrected spectra to produce a single 1D spectrum for each source covering the entire wavelength range.

During the process of the IRS data reduction, we rejected four galaxies from our sample because these objects show strong contamination from another source in the slit, resulting in a dubious spectrum. After rejecting these galaxies, our IRS sample includes IRS spectra of 67 objects used in the spectral analysis. However, two of our sources were repeat visits of the same source (sources observed both by the 20113 Dole and 20128 Lagache programs). Comparing the reduced spectra for each of these sources, they give consistent results for redshift and PAH ratios. For the analysis here, we rejected the visits with lower S/N. Therefore, our final dataset includes IRS spectra for 65 unique objects.

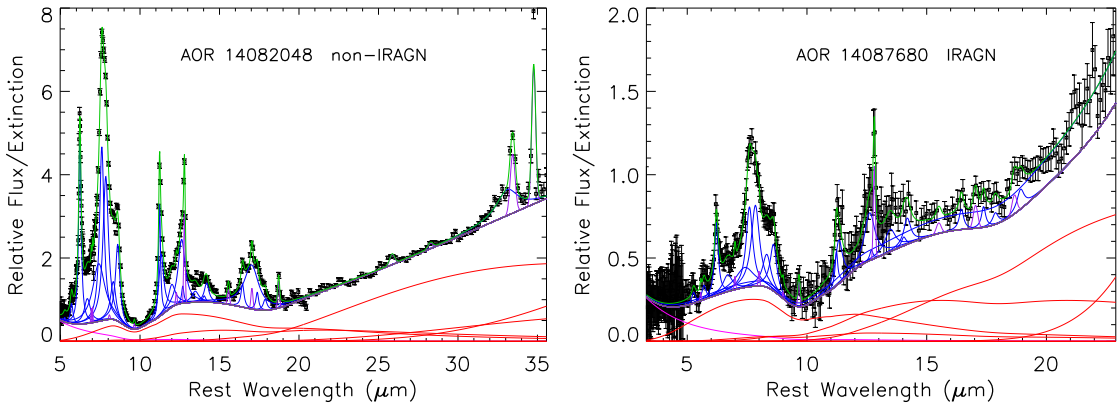

Figure 2.4 — Examples of PAHFIT spectral decomposition to object 23 (top) and object 4 (bottom). In each panel, the IRS spectroscopic data are shown as black squares. The total fit and individual spectral components fit by PAHFIT are shown, including the molecular and atomic emission features (blue curves), dust continua (red), and stellar light (magenta). The total fit (the sum of all the model components) is shown in green, which provides a good representation of the data.

2.4.3 IRS Spectral Fitting

To study the mid-IR emission features in the IRS spectra of our sample, we used the PAHFIT spectral decomposition code (Smith et al., 2007), designed for *Spitzer* IRS data. PAHFIT uses a χ^2 minimization routine to fit a non-negative combination of multiple emission features and continua to the one-dimensional spectra of our sources. The features included in PAHFIT are the dust emission features from PAHs (modeled as Drude profiles), thermal dust continuum, continuum from starlight, atomic and molecular emission lines (modeled as Gaussians), and dust extinction. The PAH emission features at (e.g. 7.7, 11.3, and 17 μm) are blends of multiple components, and PAHFIT treats these complexes as individual emission "features".

Table 2.2. Fitted Fluxes of the Most Prominent PAH Emission Features

ID	$F_{6.2}$ $[10^{-17}]$	$F_{7.7}$ $[10^{-16}]$	$F_{8.6}$ $[10^{-17}]$	$F_{11.3}$ $[10^{-17}]$	$F_{12.7}$ $[10^{-17}]$	$F_{17.0}$ $[10^{-17}]$
1	4.50 ± 1.45	2.48 ± 0.41	19.3 ± 2.30	0.39 ± 0.54	6.42 ± 0.56	...
2	0.30 ± 1.47	0.67 ± 0.72	0.79 ± 2.67	1.07 ± 0.75	1.48 ± 1.14	1.73 ± 0.54
3	...	0.26 ± 0.22	1.09 ± 0.75	0.39 ± 0.15	0.23 ± 0.33	0.99 ± 1.55
4	7. 4 ± 0.69	3.31 ± 0.34	12.2 ± 1.46	6.97 ± 1.74	6.65 ± 2.62	2.57 ± 0.85
5	6.37 ± 0.60	2.12 ± 0.24	6.92 ± 0.98	6.49 ± 0.77	3.49 ± 0.68	3.19 ± 2.28
6	0.58 ± 0.48	0.30 ± 0.17	0.78 ± 0.41	1.02 ± 0.19	0.12 ± 0.29	0.74 ± 0.90
7	7.5 ± 1.62	5.58 ± 0.48	14.6 ± 1.57	13.5 ± 1.49	7.30 ± 2.49	5.12 ± 3.88
8	17.2 ± 0.94	6.45 ± 0.33	8.0 ± 1.03	16.6 ± 0.90	9.28 ± 1.48	8.38 ± 1.56
9	11.4 ± 1.52	3.46 ± 0.67	12.4 ± 2.39	9.90 ± 1.85	6.50 ± 1.16	2.11 ± 0.66
10	7.48 ± 5.79	2.34 ± 0.79	7.76 ± 2.03	7.95 ± 2.16	7.84 ± 2.58	6.69 ± 3.23
11	7.01 ± 0.68	2.34 ± 0.23	7.49 ± 1.23	6.61 ± 0.82	4.50 ± 0.51	2.14 ± 1.79
12	0.88 ± 0.54	0.56 ± 0.23	1.27 ± 0.78	0.70 ± 0.40	0.46 ± 0.17	0.11 ± 0.27
13	26.7 ± 1.01	9.80 ± 0.51	29.2 ± 1.68	23.8 ± 1.75	14.8 ± 1.53	8.19 ± 3.29
14	4.45 ± 0.68	1.31 ± 0.27	4.98 ± 1.37	7.59 ± 1.20	1.63 ± 0.87	2.62 ± 2.14
15	5.12 ± 0.70	1.75 ± 0.28	5.69 ± 1.09	4.95 ± 0.77	3.76 ± 0.71	2.26 ± 1.94
16	1.42 ± 1.69	0.16 ± 0.74	0.95 ± 2.01	2.15 ± 1.67	1.80 ± 1.72	1.28 ± 0.85
17	2.07 ± 3.19	0.59 ± 0.54	2.28 ± 2.02	2.10 ± 1.13	1.14 ± 1.42	1.73 ± 2.26
18	9.08 ± 0.91	2.60 ± 0.34	10.1 ± 1.05	8.75 ± 0.85	3.96 ± 0.71	6.74 ± 1.14
19	1.76 ± 1.61	0.76 ± 0.43	2.23 ± 1.31	2.44 ± 1.12	1.55 ± 1.14	0.91 ± 0.60
20	28.6 ± 0.77	9.29 ± 0.37	28.8 ± 1.08	26.3 ± 0.86	16.1 ± 0.91	18.1 ± 1.51
21	10.8 ± 0.69	3.88 ± 0.33	21.4 ± 1.22	10.9 ± 1.24	5.57 ± 1.18	2.99 ± 2.42
22	43.1 ± 0.87	15.7 ± 0.36	223.1 ± 1.08	42.6 ± 0.76	24.9 ± 1.14	30.0 ± 1.75
23	81.0 ± 1.51	30.9 ± 0.49	79.6 ± 1.82	231.3 ± 1.39	38.4 ± 1.32	58.1 ± 2.25
24	1.18 ± 0.71	0.60 ± 0.28	2.40 ± 0.98	1.39 ± 0.40	0.47 ± 0.16	0.74 ± 1.87
25	22.1 ± 0.90	7.34 ± 0.40	21.8 ± 0.87	21.8 ± 0.64	9.89 ± 0.89	256.8 ±25.17
26	3.43 ± 1.00	1.22 ± 0.31	3.85 ± 1.00	3.43 ± 0.66	2.65 ± 1.16	1.96 ± 1.50
27	27.2 ± 0.88	10.7 ± 0.35	37.7 ± 1.10	30.1 ± 0.86	16.1 ± 1.06	270.9 ± 1.76
28	7.17 ± 0.67	2.65 ± 0.22	7.75 ± 0.66	7.86 ± 0.60	5.62 ± 0.59	5.78 ± 1.02
29	5.88 ± 0.51	2.60 ± 0.19	8.07 ± 0.64	6.09 ± 0.69	2.15 ± 0.39	3.41 ± 1.03
30	11.9 ± 0.76	4.33 ± 0.41	16.1 ± 1.25	14.4 ± 1.24	8.55 ± 0.98	5.06 ± 2.62
31	1.81 ± 0.66	0.54 ± 0.12	1.84 ± 0.78	3.01 ± 0.49	0.83 ± 0.55	3.19 ± 1.54
32	5.40 ± 0.91	1.47 ± 0.40	5.83 ± 1.08	6.79 ± 0.80	2.90 ± 0.60	2.60 ± 0.95
33	0.89 ± 0.52	0.32 ± 0.08	1.23 ± 0.66	0.82 ± 0.52	0.76 ± 0.84	1.11 ± 0.66
34	0.55 ± 0.47	0.31 ± 0.18	1.50 ± 0.85	0.45 ± 0.67	0.84 ± 1.20	0.25 ± 0.27
35	10.6 ± 1.06	3.84 ± 0.40	12.2 ± 1.22	13.7 ± 1.00	7.25 ± 1.01	12.7 ± 2.08
36	1.61 ± 1.13	0.63 ± 0.17	1.88 ± 0.82	2.08 ± 0.52	1.49 ± 0.51	0.37 ± 0.53
37	1.96 ± 0.68	1.07 ± 0.16	2.83 ± 0.67	3.24 ± 0.88	2.85 ± 0.84	0.27 ± 0.33
38	61.5 ± 0.89	385.5 ± 0.43	66.5 ± 1.22	77.2 ± 1.04	39.6 ± 1.18	173. ± 4.74
39	1.67 ± 1.03	0.79 ± 0.29	2.71 ± 1.16	1.74 ± 0.64	1.28 ± 0.37	2.01 ± 2.61
40	7.97 ± 3.22	2.41 ± 0.71	7.85 ± 2.82	6.70 ± 2.50	5.25 ± 2.36	5.57 ± 8.23
41	1.67 ± 0.42	0.60 ± 0.19	2.06 ± 0.88	3.71 ± 0.43	2.56 ± 0.73	2.24 ± 1.75
42	7.96 ± 1.22	2.37 ± 0.27	7.35 ± 1.15	4.79 ± 1.12	9.65 ± 0.37	7.60 ± 1.54
43	10.1 ± 0.96	4.13 ± 0.35	10.7 ± 1.14	7.72 ± 1.43	5.83 ± 1.64	4.68 ± 2.36
44	0.80 ± 0.84	0.68 ± 0.34	0.55 ± 0.83	2.19 ± 0.39	0.24 ± 0.13	0.01 ± 0.42
45	2.81 ± 1.01	0.90 ± 0.34	3.45 ± 0.97	3.30 ± 0.49	0.44 ± 0.50	0.91 ± 0.67
46	17.4 ± 0.79	6.54 ± 0.40	20.8 ± 1.01	20.3 ± 0.93	10.0 ± 0.83	21.9 ± 1.85
47	3.97 ± 1.37	1.66 ± 0.54	7.86 ± 2.36	6.19 ± 2.01	1.31 ± 0.90	1.94 ± 2.02
48	0.47 ± 0.73	0.05 ± 0.14	0.60 ± 1.57	...	0.40 ± 0.96	1.09 ± 1.18
49	4.19 ± 0.39	1.83 ± 0.18	4.64 ± 0.74	4.81 ± 1.10	3.28 ± 1.40	1.51 ± 1.32
50	0.37 ± 7.50	0.37 ± 0.20	1.90 ± 1.51	2.01 ± 1.56	0.78 ± 1.17	0.91 ± 1.36
51	18.2 ± 1.36	6.27 ± 0.33	21.5 ± 1.00	19.3 ± 0.98	12.2 ± 0.58	6.54 ± 0.75
52	9.22 ± 0.80	2.83 ± 0.29	10.0 ± 1.26	9.88 ± 0.61	4.36 ± 0.63	5.59 ± 0.79
53	2.66 ± 1.12	0.97 ± 0.40	2.92 ± 1.56	3.62 ± 1.78	1.46 ± 1.49	1.33 ± 0.89
54	5.86 ± 0.88	2.16 ± 0.28	5.94 ± 0.79	6.65 ± 0.77	5.25 ± 1.13	1.19 ± 0.49
55	3.73 ± 0.56	1.08 ± 0.24	3.54 ± 1.00	5.52 ± 0.97	2.01 ± 0.55	2.86 ± 2.47
56	44.3 ± 5.43	8.94 ± 1.77	28.6 ± 5.48	29.0 ± 5.00	20.8 ± 3.42	16.9 ± 4.31
57	16.0 ± 4.62	4.44 ± 0.71	11.3 ± 2.86	8.66 ± 3.22	5.01 ± 1.34	1.37 ± 0.61
58	6.92 ± 0.60	2.20 ± 0.26	7.06 ± 0.87	8.03 ± 0.77	4.40 ± 0.49	3.69 ± 2.28

Table 2.2 (cont'd)

ID	$F_{6.2}$ $[10^{-17}]$	$F_{7.7}$ $[10^{-16}]$	$F_{8.6}$ $[10^{-17}]$	$F_{11.3}$ $[10^{-17}]$	$F_{12.7}$ $[10^{-17}]$	$F_{17.0}$ $[10^{-17}]$
59	0.65 ± 0.57	0.24 ± 0.22	1.43 ± 0.99	0.32 ± 0.34	0.31 ± 0.34	1.48 ± 0.83
60	1.04 ± 0.51	0.35 ± 0.09	1.42 ± 0.49	1.04 ± 0.22	0.83 ± 0.72	2.13 ± 0.88
61	1.50 ± 0.43	0.60 ± 0.20	2.67 ± 0.79	1.11 ± 0.27	0.09 ± 0.47	0.41 ± 0.54
62	9.76 ± 1.21	3.45 ± 0.31	11.3 ± 0.95	13.0 ± 0.92	6.90 ± 0.49	4.58 ± 0.67
63	4.87 ± 0.66	1.67 ± 0.18	5.24 ± 0.62	4.39 ± 0.39	3.20 ± 0.49	1.85 ± 0.82
64	9.25 ± 1.76	3.14 ± 0.40	8.46 ± 1.31	11.5 ± 1.26	4.78 ± 1.26	4.92 ± 2.03
65	3.85 ± 0.56	1.14 ± 0.20	3.90 ± 1.09	3.05 ± 0.63	0.44 ± 0.16	2.16 ± 1.65

Note. — Integrated fluxes in W/m^2 from PAHFIT spectral decomposition for the PAH Emission features. Values given as (...) do not have a measured flux from PAHFIT spectral decomposition.

We used PAHFIT to fit the IRS spectrum for each galaxy in our sample. The line fluxes derived by PAHFIT for the emission features for each object are listed in table 2.2 and table 2.3. Figure 2.4 shows the PAHFIT spectral decompositions for the spectra of objects ID=4 and 23 in our sample, using the IDs in Table 2.1. Object 4 is classified as an IRAGN as described by the method in Section 2.3.3, while object 23 shows no indication of an AGN. The spectra are characteristic of the data quality and fit quality of our sample.

Table 2.3. Fitted Fluxes of the Most Prominent Atomic Emission Lines

ID	$F_{[NeII]}$ $[10^{-18}]$	$F_{[NeIII]}$ $[10^{-18}]$	$F_{[OIV]}$ $[10^{-18}]$	$F_{[H_2S(3)]}$ $[10^{-18}]$
1	8.84 ± 1.25	10.6 ± 1.30	1.52 ± 4.16	24.5 ± 20.9
2	...	...	1.75 ± 0.49	3.15 ± 3.68
3	2.25 ± 0.70	...	...	0.52 ± 1.23
4	15.0 ± 3.55	3.56 ± 4.51	2.17 ± 0.59	9.78 ± 5.04
5	11.2 ± 1.04	1.33 ± 3.02	...	1.62 ± 1.57
6	3.03 ± 0.76	0.17 ± 2.81	14.9 ± 5.49	0.02 ± 1.19
7	26.0 ± 2.75	4.24 ± 2.33	7.54 ± 2.23	46.1 ± 9.36
8	22.6 ± 2.07	12.0 ± 1.68	...	0.48 ± 1.17
9	14.5 ± 2.96	1.52 ± 3.35	1.70 ± 5.54	5.09 ± 4.81
10	14.0 ± 3.53	3.33 ± 4.20	...	3.40 ± 4.24
11	7.65 ± 1.24	...	1.25 ± 0.36	2.81 ± 1.66
12	...	...	0.81 ± 0.23	0.39 ± 0.70
13	25.2 ± 2.18	2.69 ± 2.36	5.97 ± 3.18	6.04 ± 3.00
14	6.46 ± 1.00	3.23 ± 3.01	...	6.61 ± 5.54
15	5.74 ± 1.01	...	...	0.93 ± 1.85
16	2.49 ± 3.30	2.75 ± 5.95	23.2 ± 7.35	1.70 ± 3.21
17	3.37 ± 1.76	2.85 ± 2.14	...	0.77 ± 4.28
18	17.7 ± 0.86	6.50 ± 0.91	2.24 ± 2.44	7.11 ± 2.98
19	1.05 ± 1.08	0.87 ± 1.64	...	0.32 ± 2.08
20	51.3 ± 1.41	9.63 ± 1.94	2.30 ± 1.48	3.77 ± 1.19
21	16.3 ± 1.70	1.15 ± 4.65	1.04 ± 1.71	2.10 ± 2.06
22	226.8 ± 1.73	11.5 ± 1.63	4.82 ± 16.5	8.08 ± 1.29
23	235.8 ± 1.95	13.1 ± 1.68	11.6 ± 1.45	13.4 ± 3.34
24	1.33 ± 0.67	8.98 ± 1.50	6.43 ± 4.13	1.19 ± 1.76
25	25.8 ±25.25	42.9 ±25.34	...	25.99 ±25.25
26	3.13 ± 1.46	0.89 ± 1.18	20.8 ± 0.67	0.62 ± 1.27
27	35.3 ± 1.67	8.80 ± 1.45	2.19 ± 1.61	7.71 ± 1.56
28	28.11 ± 0.96	0.91 ± 0.77	2.60 ± 0.69	1.66 ± 1.51
29	9.12 ± 0.97	0.99 ± 0.91	1.04 ± 1.29	9.11 ± 2.84
30	27.4 ± 2.43	7.72 ± 2.65	...	17.1 ± 3.86
31	2.65 ± 0.75	1.17 ± 2.78	...	3.83 ± 5.45
32	9.22 ± 0.90	2.27 ± 0.70	...	1.13 ± 1.74
33	1.99 ± 1.14	9.76 ± 40.0	3.06 ± 2.65	0.40 ± 1.32
34	0.58 ± 1.55	0.52 ± 1.40	0.52 ± 0.15	1.76 ± 1.98
35	16.7 ± 1.36	2.78 ± 1.51	1.68 ± 1.88	3.60 ± 2.64
36	3.35 ± 0.60	0.26 ± 0.87	1.91 ± 2.85	0.49 ± 3.05
37	...	1.66 ± 1.51	0.51 ± 1.63	...
38	86.2 ± 1.69	60.7 ± 3.56	12.4 ± 5.60	10.5 ± 1.40
39	1.99 ± 0.75	1.36 ± 1.01	2.52 ± 7.10	4.18 ± 4.63
40	6.87 ± 3.45	2.37 ± 3.43	3.17 ± 3.98	2.99 ± 6.70
41	6.07 ± 1.26	3.24 ± 1.87	0.50 ± 0.14	3.08 ± 0.99
42	42.4 ± 1.18	5.81 ± 0.94	...	3.48 ± 2.45
43	24.3 ± 2.38	4.42 ± 2.69	...	4.72 ± 2.74
44	0.65 ± 0.62	2.44 ± 0.74	...	1.02 ± 1.92
45	6.30 ± 0.70	...	2.90 ± 1.13	0.23 ± 1.42
46	20.1 ± 1.16	4.73 ± 1.29	1.28 ±46.27	46.71 ± 1.32
47	7.03 ± 1.30	2.10 ± 2.71	2.43 ± 5.68	14.0 ± 20.8
48	0.46 ± 4.35	0.51 ± 4.18	0.69 ± 0.19	13.3 ± 22.0
49	6.70 ± 1.90	2.56 ± 1.31	1.06 ± 0.29	1.95 ± 1.57
50	2.18 ± 1.50	0.96 ± 1.58	2.98 ± 1.86	2.49 ± 3.60
51	51.1 ± 0.80	7.58 ± 0.68	1.76 ± 1.31	4.08 ± 1.29
52	11.8 ± 0.98	6.27 ± 1.02	5.50 ± 1.14	5.18 ± 3.71
53	1.53 ± 1.79	6.88 ± 3.58	0.68 ± 0.19	1.29 ± 2.55
54	12.4 ± 1.51	11.6 ± 1.71	4.18 ± 1.33	1.11 ± 1.26
55	8.55 ± 1.32	...	64.4 ± 18.3	1.82 ± 2.39
56	36.9 ± 3.98	9.21 ± 2.81	...	10.2 ± 11.4
57	9.29 ± 1.65	6.66 ± 1.44	...	17.3 ± 12.4
58	13.0 ± 0.87	4.23 ± 1.06	3.16 ± 2.89	0.94 ± 1.17

Table 2.3 (cont'd)

ID	$F_{[NeII]}$ $[10^{-18}]$	$F_{[NeIII]}$ $[10^{-18}]$	$F_{[OIV]}$ $[10^{-18}]$	$F_{[H_2S(3)]}$ $[10^{-18}]$
59	...	0.36 ± 1.39	0.43 ± 0.12	1.18 ± 0.78
60	0.93 ± 0.62	0.61 ± 1.42	22.4 ± 5.32	0.42 ± 0.71
61	0.56 ± 0.55	...	0.56 ± 0.15	0.19 ± 0.36
62	13.9 ± 0.61	2.05 ± 0.45	5.89 ± 1.07	3.40 ± 1.48
63	7.29 ± 0.65	1.84 ± 0.48	1.80 ± 1.05	1.16 ± 0.98
64	19.9 ± 1.60	2.96 ± 1.38	...	6.93 ± 3.25
65	7.76 ± 0.93	...	0.61 ± 0.17	3.18 ± 2.48

Note. — Integrated fluxes in W/m^2 from PAHFIT spectral decomposition for the atomic emission lines. Values given as (...) do not have a measured flux from PAHFIT spectral decomposition.

We fit the IRS spectra for the galaxies in our sample using PAHFIT models with and without dust extinction. PAHFIT uses a model where the dust is mixed with the emitting stars and grains, as opposed to an absorbing screen. Our fits showed that the PAHFIT χ^2 values are improved using models with dust extinction for 60/65 galaxies in our sample (the other 5 galaxies had similar χ^2 values and are low S/N sources). Other studies have also found it desirable to use the default PAHFIT dust extinction parameter (Smith et al., 2007; O'Dowd et al., 2009; Wu et al., 2010; Diamond-Stanic & Rieke, 2010). Therefore, we chose to use results from PAHFIT for our sample that include dust extinction. However, none of our conclusions are changed if we use the fits excluding dust extinction.

Using PAHFIT, we also fit for the redshift of each galaxy using the IRS spectra. All galaxies in our sample have a measured redshift from optical spectroscopy from AGES in the Boötes sample (Kochanek et al., 2012) or from Papovich et al. (2006) in the FLS sample, but the PAHFIT measurement provides an independent check on the redshift, and provides supporting evidence that the mid-IR source corresponds to the optical counterpart. PAHFIT requires an input redshift (it does not minimize over redshift as part of the fit). Therefore, for each galaxy in our sample we used

PAHFIT with a grid of redshift. We did this step iteratively. We first ran PAHFIT using a the full redshift range with $0.0 < z < 0.6$ with steps of $\Delta z = 0.01$, and we selected the fit with the best reduced χ^2. We then refined the redshift solution by fitting the redshift with $\Delta z = 0.001$ using a redshift range ± 0.1 about the best-fit redshift from the first step.

We verified the consistency in our redshifts by doing a comparison to the AGES optical redshifts. We found the two redshifts for all galaxies agree within 2%, the resolution of the IRS. Table 2.1 gives both the redshift measured from the optical spectroscopy and the redshift measured independently from the IRS spectrum here.

2.4.4 Offset Between IRS SL and LL Modules

In the analysis below, one of the important emission-line ratios we will consider is the relative strength of the 7.7 μm to 11.3 μm PAH features. For galaxies with $z < 0.2$, these lines both sit in the IRS SL module, but for $z \geq 0.2$, the 11.3 μm feature shifts into the LL module, in which case the two lines are measured from different modules with different slit widths. Our procedure to flux-calibrate the spectra using the IRAC and MIPS photometry described above should account for changes in the relative flux owing to the slit widths. Nevertheless, we did some additional tests to confirm that the flux measured for the 11.3 μm feature is accurate.

The median redshift of our IRS sample is $z_{\rm median} = 0.28$, and therefore, nearly 50% of the galaxies in our IRS sample have the 11.3 μm feature in the LL module. For approximately one quarter of the sample ($0.19 < \mathrm{z} < 0.28$), the 11.3 μm feature lies in the overlap region covered by both the SL and LL modules. For these galaxies, we compared the measured emission of this feature in the SL and LL modules separately, and found that for 13/16 galaxies there was less than a 3% difference in the measured flux of the feature. For the remaining three galaxies, the features have lower signal-to-

noise, and the difference in the fluxes is within the uncertainties on the measurement. Therefore, we are confident that the uncertainties are fully represented in the errors on the data, and that any systematic errors from our flux calibration from using the two modules are small.

2.5 Comparison of Mid-IR Emission Features and Relation to Total Infrared Luminosity

2.5.1 Composite Spectra

The spectra of the IRAGN and non-IRAGN subsamples show different continua and strength of emission features, as illustrated in Figure 2.5. The figure shows composite spectra for the full sample (IRAGN + non-IRAGN), the IRAGN, and non-IRAGN. The composite spectra were created by performing a weighted mean. First, the spectra were interpolated to a common wavelength spacing using the observed wavelength scale of each order for the SL and LL modules ($\Delta\lambda$(SL2) $\approx 0.030\mu$m, $\Delta\lambda$(SL1) $\approx 0.059\mu$m, $\Delta\lambda$(LL2) $\approx 0.083\mu$m, $\Delta\lambda$(LL1) $\approx 0.166\mu$m) to preserve the information from each spectrum when creating the composite spectrum. The composite spectra are then normalized to the continua fluxes at 21μm. An outset panel of each composite spectrum is shown for the [O IV] $\lambda 25.9\mu$m emission line. For the [O IV] panel, we have subtracted the continuum out (by fitting a line to the continuum around the [O IV] line for each composite spectrum) to better show the strength of the [O IV] line for the IRAGN compared to the non-IRAGN. The [O IV] atomic line at 25.89μm has been established to be an indicator of AGN luminosity by Meléndez et al. (2008) and Rigby et al. (2009) by comparison to hard (E $>$ 10 keV) X-rays. Diamond-Stanic et al. (2009) showed that this line can be used to find AGN that are in heavily dust-obscured galaxies and therefore are missed by optical, X-ray, and other selection criteria.

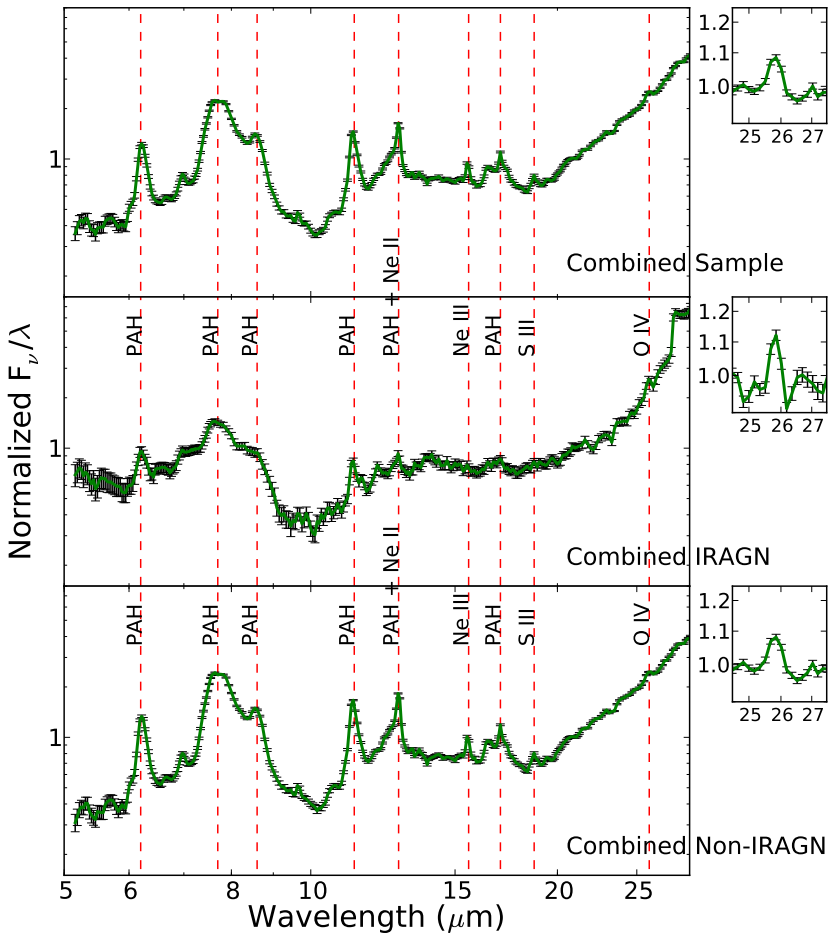

Figure 2.5 — Composite spectra for the IRS sample. The top panel shows the composite spectrum for all 65 galaxies in the IRS sample. The middle and bottom panels show composite spectra for the subsamples of IRAGN (14 galaxies) and non-IRAGN (51 galaxies), respectively. The vertical red-dashed lines indicate the prominent PAH features and emission lines in the wavelength range, as labeled. The flux is normalized at the continuum flux of 21μm. The outset panels show the composite spectra in a small wavelength region 24.5μm-27.5μm to show the strength of the [O IV] λ25.9μm emission line (see section 2.5.1 for explanation). The error bars shown is the error on the weighted mean for each composite spectrum.

The IRAGN composite spectrum shows a lower PAH emission equivalent width compared to the non-IRAGN composite spectrum. The most apparent PAH emission feature in the IRAGN subsample is the weak 7.7 μm feature. The continuum is mostly flat across the wavelength range of the spectra, suggesting the continuum is raised in response to heating from the AGN (more detailed studies of the mid-IR continuum shape such as Petric et al., 2011; Veilleux et al., 2009, have seen similar results). Furthermore, the PAH features are not absent in the IRAGN, which suggests that in part, the mid-IR continuum from the AGN is diluting the luminosity from the PAH features. In comparison, the continuum is much weaker in the non-IRAGN composite spectrum, and this spectrum shows very prominent PAH and other emission features throughout the wavelength range covered.

2.5.2 Measuring the Total Infrared Luminosity

We used model spectral energy distributions (SEDs) to estimate the total L_{IR} = $L_{8-1000\mu m}$ from the MIPS 24μm flux densities for all sources. 70μm and 160μm flux densities were used when available from MAGES for Boötes sources and Frayer et al. (2006) for the FLS sources. To calculate the total IR luminosity, we tested several model libraries that provide far-IR SEDs that vary in shape as a function of galaxy IR luminosity and ionization (Dale & Helou, 2002; Chary & Elbaz, 2001; Rieke et al., 2009). For galaxies with 24 and 70 μm detections, or 24, 70, and 160 μm flux densities, the total IR luminosities are consistent (within 40%) using any of the IR SEDs from Chary & Elbaz (2001), Dale & Helou (2002), or Rieke et al. (2009). However, because 19 galaxies (including four IRAGN) in our sample are detected at only 24 μm, we use the Rieke et al. (2009) IR SEDs because our tests showed that the total IR luminosities derived using their templates with only the 24 μm are closest with those derived from multiple MIPS bands (24 and 70 μm, or 24, 70,

and 160 μm). These tests are described more fully in Appendix A. For the four IRAGN only detected at 24μm, we interpret the luminosities from the purely star-forming spectral templates to be upper limits. However, if we assume an extreme case of a quasar (using the quasar SED templates of Shang et al., 2011) then our total IR luminosity is at most overestimated by a factor of 3.5 for these four IRAGN. However, we consider this highly unlikely because the MIPS-to-IRAC flux ratios for these four IRAGN ($F_{24\mu m}/F_{8.0\mu m} = 4.2$ median) is highly discrepant from the optically luminous quasars of Shang et al. (2011) ($F_{24\mu m}/F_{8.0\mu m} = 1.4$ median) and so this factor of 3.5 is a very conservative limit for this extreme case. We believe our estimates of the total IR luminosity to be valid due to the majority of our sample being LIRGs and having modest redshifts, based on the work of Rujopakarn et al. (2012).

Figure 2.6 shows the calculated total IR luminosities from fits to the MIPS data using the Rieke et al. (2009) IR SEDs. Table 2.1 lists the MIPS flux densities for 24μm, 70μm, and 160μm, along with the total IR luminosities. The figure also shows the relation for the IRS sample of the *Spitzer* SDSS Galaxy Spectroscopic Survey (SSGSS) from O'Dowd et al. (2009), which illustrates the distinction in IR luminosity and redshift range between their sample and our sample here.

2.5.3 Contribution of PAH Emission to L_{IR}

In figure 2.7, we show the distribution of L_{PAH}/L_{IR} for the entire sample (bottom panel), the subsamples of IRAGN (middle panel) and non-IRAGN (top panel). Here L_{PAH} is the sum of all the luminosities of the PAH features at 6.2, 7.7, 8.6, 11.3, 12.7, and 17.0 μm, and L_{IR} is the total IR luminosity as described in section 2.5.2 using the Rieke et al. (2009) templates. The median ratio of L_{PAH}/L_{IR} is 0.08 with an interquartile range (which contains the inner 50% of galaxies) of 0.05 to 0.11.

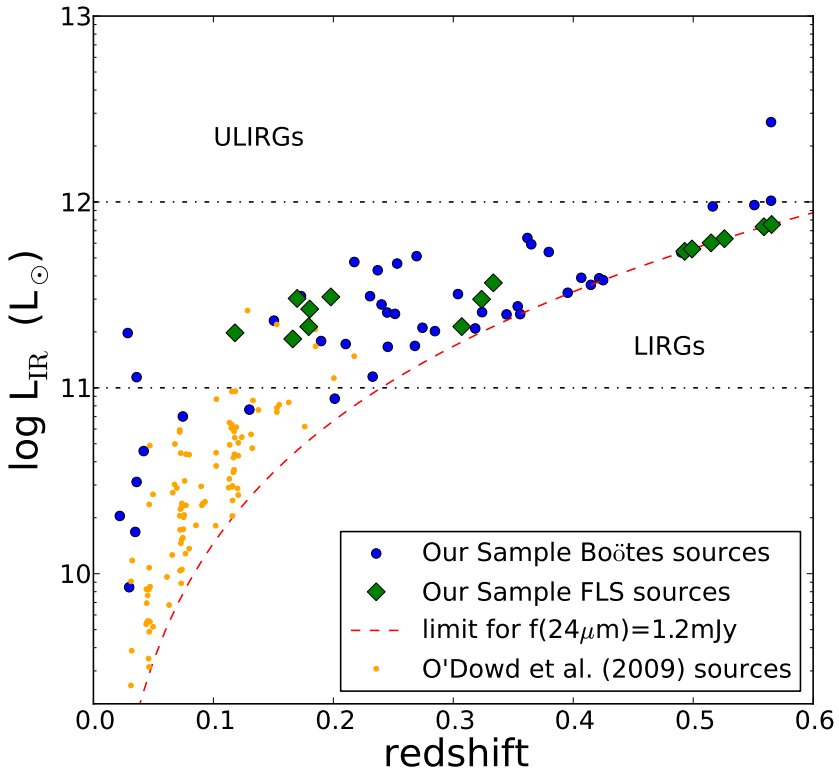

Figure 2.6 — Redshift versus the total IR luminosity from 8-1000μm for our IRS sample (blue circles, Boötes sources; green diamonds, FLS sources) derived from the MIPS 24 μm data (and 70 and 160 μm, if available) derived using the Rieke et al. (2009) IR SEDs. The galaxies in our IRS sample span the range of IR luminosity of "Luminous IR galaxies" (LIRGs), $L_{IR} = 10^{11} - 10^{12} L_\odot$. The figure also shows the O'Dowd et al. (2009) SSGSS sample (orange circles), which are lower redshift and IR luminosity. The dashed curve shows the limiting IR luminosity as a function of redshift for a fixed 24 μm flux density of 1.2 mJy using the IR SEDs from Rieke et al. (2009).

We find that L_{PAH}/L_{IR} is higher in the non-IRAGN sample, with a median of 0.09, compared to $L_{PAH}/L_{IR} = 0.05$ for the IRAGN. A K-S test applied to the distributions gives a D-statistic = 0.52, which indicates a 99.7% likelihood that the IRAGN and non-IRAGN have different parent distributions. If we exclude the four IRAGN only detected at 24μm and not in the far-IR, the K-S test gives a D-statistic = 0.49 and a likelihood of 97.6%.

The 7.7μm feature for either IRAGN or non-IRAGN contributes significantly to the entire amount of PAH emission. The median $L_{7.7}/L_{PAH}$ is 0.45 with an interquartile range (which contains the inner 50% of galaxies) of 0.40 to 0.48 for our sample; and the median IRAGN $L_{7.7}/L_{PAH}$ is slightly higher at 0.49. These results show that as much as 10% of the total IR luminosity can come from the 7.7μm feature alone.

The IRAGN in our sample show lower L_{PAH}/L_{IR} compared to the non-IRAGN, where 13/14 IRAGN have $L_{PAH}/L_{IR} < 0.09$. This is similar to the findings of Smith et al. (2007), who suggested there may be a natural limit to the absolute PAH strength in sources with AGNs, either because of partial destruction of the grains or an increase to the total infrared luminosity from other continuum sources. However, there are two key differences between our sample and that of Smith et al. (2007). First, the objects in our sample have (in most cases) significantly higher IR luminosities. Second, the IRS apertures encompass the integrated light from the galaxies in our sample, whereas the IRS resolves those in the Smith et al. (2007) sample to include light separately from the disk and nucleus. This will tend to dilute the effects of the AGN on the integrated PAH ratios. We discuss this further in section 2.6.2.

2.5.4 Detection Frequency of Emission Features

Figure 2.8 shows the fraction of galaxies in our sample whose IRS spectra show some of the most common emission features detected at $\geq 3\sigma$ significance. Emis-

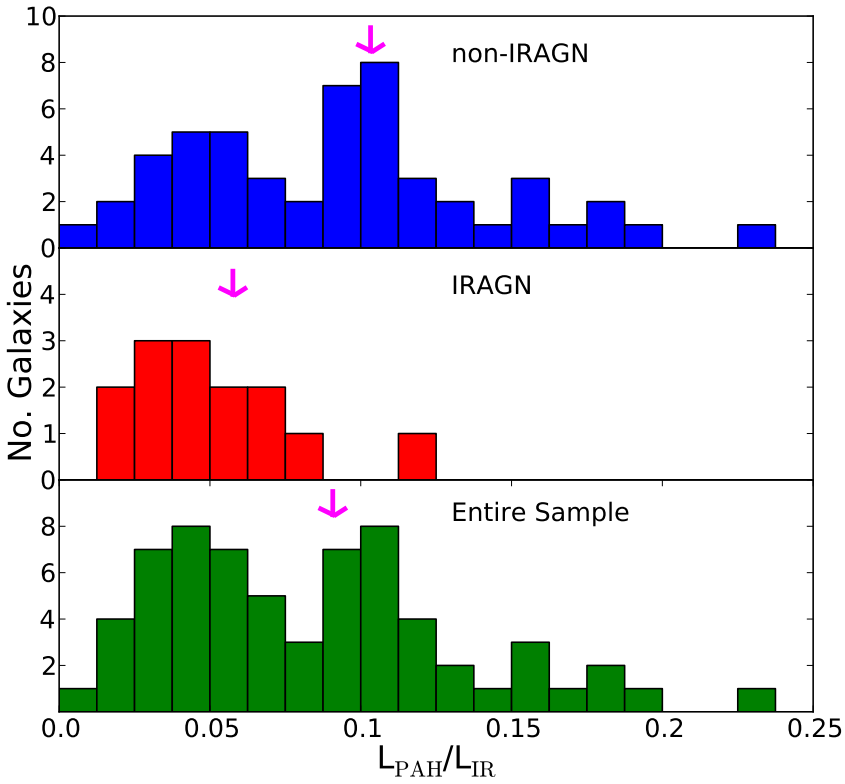

Figure 2.7 — The distribution of L_{PAH}/L_{IR} for our sample, where L_{PAH} is the total luminosity of the 6.2, 7.7, 8.6, 11.3, 12.7, and 17.0μm PAH emission features. The bottom panel shows the distribution for our IRS sample. The middle panel shows the distribution for our subsample of IRAGN, and the top panel shows the distribution for our subsample of non-IRAGN. The median L_{PAH}/L_{IR} is 0.05 for the IRAGN, and is about half that for the non-IRAGN which have a median of $L_{PAH}/L_{IR} = 0.09$. The arrows represent the L_{PAH}/L_{IR} ratios from the composite spectra in figure 2.5 ($L_{PAH}/L_{IR} = 0.09$, 0.06, and 0.10 for the IRS sample, IRAGN, and non-IRAGN, respectively).

sion frequencies are given in table 2.4 for the full sample, non-IRAGN, and IRAGN subsamples. As an example, the 7.7μm PAH emission feature is found with $\geq 3\sigma$ significance in only 5 out of the 14 IRAGN in our the sample, and therefore its frequency is 36%. Although a variety of factors can influence detection of the PAH features, since our sample is selected primarily on mid-IR flux, to first order we should reach similar detection limits on average for all the sample members.

The 6.2μm, 7.7μm, 8.6μm, 11.3μm, and 12.7μm PAH features are present in more than 50% of the galaxies in our sample (and the same PAH features are present in more than 70% of the non-IRAGN galaxies). The most commonly detected PAH emission feature is the 11.3μm feature with a frequency of 75%. The PAH feature with the lowest detection frequency (29%) is the 17μm feature. Considering the two subsamples, the frequency of the PAH emission features for the IRAGN subsample is less than half that of the non-IRAGN subsample except for the 11.3μm feature, which has 50% for IRAGN and 82% for the non-IRAGN. This supports the conclusion from Diamond-Stanic et al. (2009) that the 11.3μm feature is relatively unaffected by AGN.

Figure 2.8 shows the frequency that the [Ne II] λ12.8μm, [Ne III] λ15.6μm, and [O IV] λ25.9μm emission lines are detected with $\geq 3\sigma$ significance in our IRS sample. The emission line of [Ne II] is a tracer of the SFR (Ho & Keto, 2007), while the ratio of [Ne III]/[Ne II] and the [O IV] emission line trace harder ionization parameters that correlate with AGN intrinsic luminosity (e.g. Diamond-Stanic et al., 2009; Meléndez et al., 2008; Rigby et al., 2009). The [Ne II] line has a >80% detection frequency for the non-IRAGN subsample, significantly higher than the ∼20% detection frequency for the IRAGN subsample. In contrast, the [O IV] line has >70% detection frequency in the IRAGN subsample compared to ∼30% for the non-IRAGN. These detection frequencies of [Ne II] and [O IV] are independent of the selection of these subsamples

Table 2.4. Emission Feature Detection Frequencies

Feature/Line	All galaxies	non-IRAGN galaxies	IRAGN galaxies
6.2μm	41/65 63%	37/51 73%	4/14 29%
7.7μm	47/65 72%	42/51 82%	5/14 36%
8.6μm	44/65 68%	40/51 78%	4/14 29%
11.3μm	49/65 75%	42/51 82%	7/14 50%
12.7μm	37/65 57%	36/51 71%	1/14 7%
17.0μm	19/65 29%	18/51 35%	1/14 7%
[Ne II]	46/65 71%	43/51 84%	3/14 21%
[Ne III]	22/65 34%	20/51 39%	2/14 14%
[O IV]†	22/56 39%	14/45 31%	8/11 73%

Note. — We present our detection frequencies for the most common PAH emission features and atomic emission lines in the mid-IR for the IRS sample. Each column gives the frequency that a given emission feature is detected at $\geq 3\sigma$ significance in the full sample, or the IRAGN, or the non-IRAGN subsamples (given as number of galaxies with detections in the sample or as a percentage of galaxies with detections compared to their respective sample, see section 2.5.4). In the far left column, atomic features are labeled, and PAH features are denoted by their central wavelengths. †9 sources in our sample have redshifts ($z \gtrsim 0.5$) for which [O IV] is shifted out of the IRS LL channel and are not included in the sample for this line.

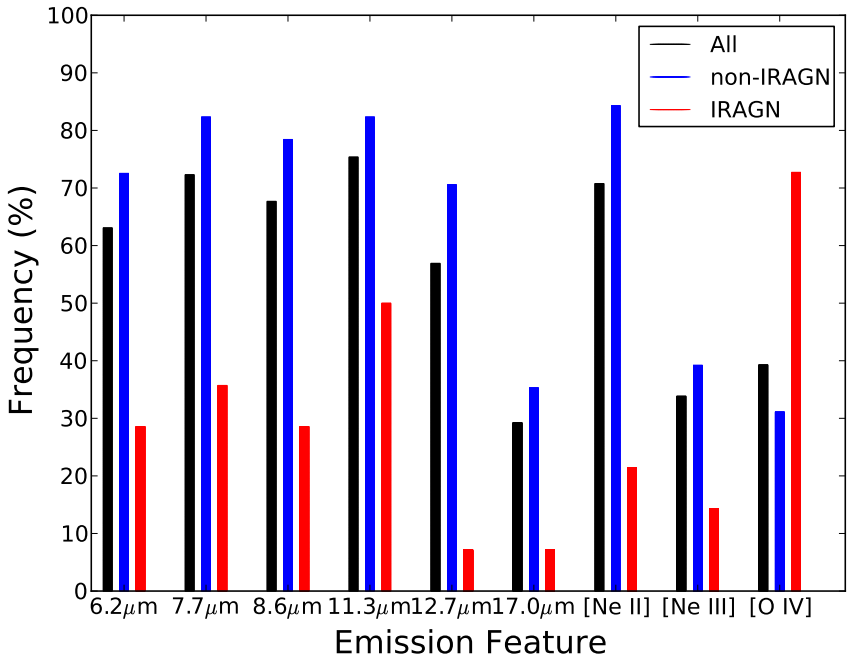

Figure 2.8 — Detection frequencies for common mid-IR PAH features and atomic emission lines in the IRS sample. Each histogram gives the frequency that a given emission feature is detected at $\geq 3\sigma$ significance in the IRS sample (black bars), or the IRAGN (red bars) or the non-IRAGN (blue bars) subsamples. On the abscissa, atomic features are labled, and PAH emission features are denoted by their central wavelengths.

(which depend solely on their IRAC colors), yet give additional evidence that the emission from these samples stems from star-formation (in the case of the non-IRAGN) and AGN (in the case of the IRAGN). We discuss the inferred physics based on the [Ne II] and [O IV] emission lines in Sections 2.5.8 and 2.6.4.

2.5.5 Measures of Grain Sizes and Ionization State

Models show that the relative power emitted in the different PAH emission features depends on the distribution of molecular grain sizes contributing to that PAH feature (Draine & Li, 2001; Schutte et al., 1993; Tielens, 2005). Generically, the models predict that PAH molecules of smaller size should emit more power at shorter

wavelengths and PAH molecules of larger size should emit more power at longer wavelengths (i.e., the emission from the 6.2μm PAH feature should be dominated by grains of smaller size than those at 11.3μm). Therefore, the ratio of the strength of longer–wavelength PAH features to shorter–wavelength PAH features constrains the size of the PAH molecules.

In addition, the models predict that the ionization state of PAH molecules affects the relative luminosity in each PAH emission feature (Draine & Li, 2001). For example, the C-C vibrational modes are expected to be more intense in ionized PAH molecules (Tielens, 2005). The 6.2μm and 7.7μm bands result from radiative relaxation of C-C stretching modes and the features should change little relative to each other as the ionization fraction changes (O'Dowd et al., 2009). In contrast, the power of the PAH bands attributed to C-H modes such as the 11.3μm and 12.7μm features is expected to decrease (moving from neutral to ionized clouds in the interstellar medium (ISM)). Therefore, the ratio of the strength of ionization–independent PAH features, such as the 6.2 and 7.7 μm feature, to ionization–dependent PAH features, such as the 11.3 and 12.7 μm features should be sensitive to the overall ionization state of the PAH molecules.

Therefore, the PAH molecule sizes and ionization state can be constrained by comparing the PAH band ratios $L_{6.2}/L_{7.7}$ to $L_{11.3}/L_{7.7}$. The former traces PAH grain size, but is relatively unaffected by ionization. The latter is sensitive to ionization and less affected by changes in grain size. Figure 2.9 shows these line ratios for the galaxies in our sample. The sample lies mostly in a locus between line ratios of 0.2–0.4 for both $L_{6.2}/L_{7.7}$ and $L_{11.3}/L_{7.7}$. This is consistent with the findings from other studies (O'Dowd et al., 2009; Diamond-Stanic & Rieke, 2010; Wu et al., 2010). We measure a weak correlation between $L_{6.2}/L_{7.7}$ and $L_{11.3}/L_{7.7}$ (Spearman's ρ = 0.41), which we interpret as evidence for decreasing PAH grain size with increasing

ionization within the locus (this is consistent with the trend seen in O'Dowd et al., 2009).

2.5.6 Relation between Radiation Hardness and PAH Strength

The emission-line ratio of the [Ne III] (15.6μm with an ionization potential of 41eV) emission to the [Ne II] (12.8 μm, with an ionization potential of 21.6eV) is a measure of the hardness of the radiation field (Smith et al., 2007). Figure 2.10 shows the ratio of $L_{[NeIII]}/L_{[NeII]}$ as a function of $L_{7.7\mu m}/L_{11.3\mu m}$, which is an indicator of the ratio of ionized-to-neutral PAH molecules, as discussed in section 2.5.5. In general, there is no correlation between $L_{[NeIII]}/L_{[NeII]}$ and $L_{7.7\mu m}/L_{11.3\mu m}$. The dashed line in figure 2.10 shows the median $L_{7.7\mu m}/L_{11.3\mu m}$ for the non-IRAGN only. There is tentative evidence that the IRAGN have $L_{7.7\mu m}/L_{11.3\mu m}$ ratios higher than this median, but this is not statistically significant given our sample size.

We see no IRAGN galaxies with extremely low $L_{7.7\mu m}/L_{11.3\mu m}$ ratios (<1), as seen in the Smith et al. (2007) sample. The $L_{7.7\mu m}/L_{11.3\mu m}$ ratio behavior contrasts strongly with Smith et al. (2007), but is in reasonable agreement with others (Wu et al., 2010; O'Dowd et al., 2009). We suspect the difference is a result of the fact that the IRS spectra for our sample contains the integrated light from the galaxy (nucleus + galaxy), whereas the IRS apertures containing the nuclei used by Smith et al. (2007) included only the galactic nuclear regions. Our sample contains few sources with high hardness ratios ([NeIII]/[NeII] > 2, similar to the samples of O'Dowd et al., 2009; Smith et al., 2007; Wu et al., 2010), and most sources with high hardness ratios are upper limits only. This suggests that higher hardness ratios cannot account for the trend seen by Smith et al. (2007). This conclusion agrees with that in Gordon et al. (2008) from a study of H II regions in M101 and Brandl et al. (2006) studying 22 starburst galaxies. Diamond-Stanic & Rieke (2010) showed that spectra taken

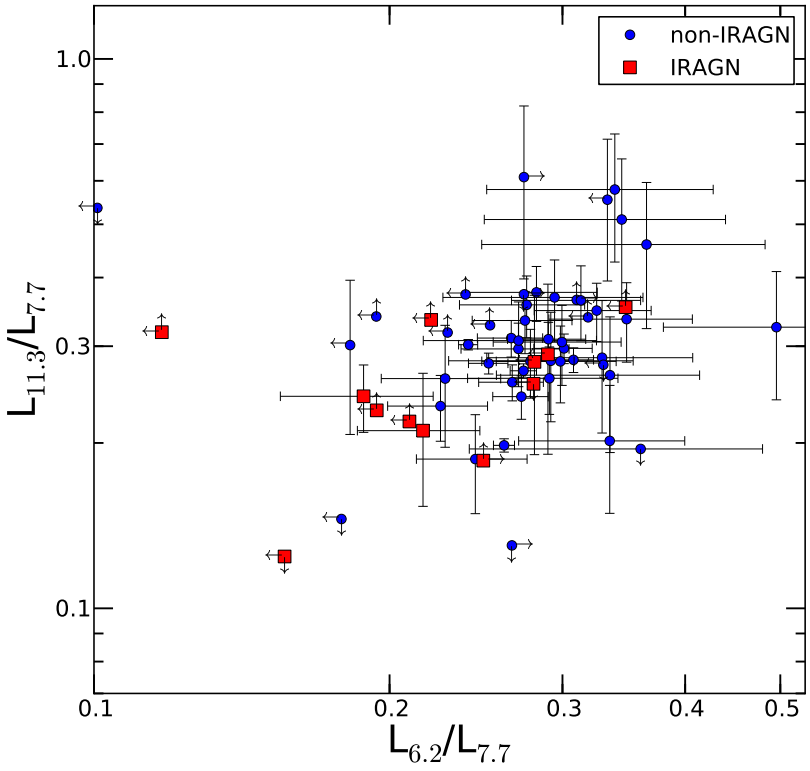

Figure 2.9 — PAH band ratios $L_{6.2}/L_{7.7}$ vs. $L_{11.3}/L_{7.7}$ for the galaxies in the IRS sample. The $L_{6.2}/L_{7.7}$ ratio is a tracer of PAH grain size, and the $L_{11.3}/L_{7.7}$ ratio is a tracer of PAH grain ionization (O'Dowd et al., 2009). The red squares denote IRAGN and the blue circles denote non-IRAGN galaxies. The IRS sample falls mostly within the locus defined by 0.2–0.4 in both axes. This shows that the galaxies have a mixture of grain sizes and different ionization fractions of PAHs. We measure a weak correlation between $L_{6.2}/L_{7.7}$ and $L_{11.3}/L_{7.7}$ (Spearman's $\rho = 0.41$), which we interpret as evidence for decreasing PAH grain size and increasing ionization within the locus. We also observe that the IRAGN ratios are slightly lower typically compared to the non-IRAGN galaxies, in our IRS sample.

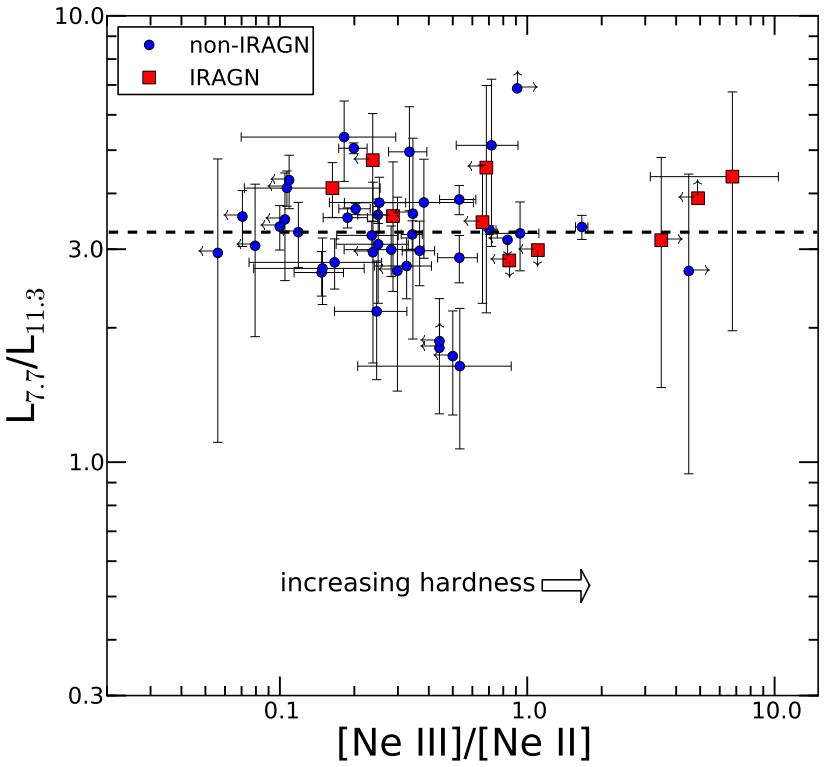

Figure 2.10 — $[\text{Ne III}]_{15.6\mu m}/[\text{Ne II}]_{12.8\mu m}$ versus $L_{7.7}/L_{11.3}$. Blue circles show the subsample of non-IRAGN, and red squares show the subsample of IRAGN (not all IRAGN have [Ne III]/[Ne II] ratio detections). The dashed line is the median $L_{7.7}/L_{11.3}$ value for the non-IRAGN subsample only. There is no trend between [Ne III]/[Ne II] and $L_{7.7}/L_{11.3}$ for either the non-IRAGN or IRAGN. This is similar to the conclusions from other studies (O'Dowd et al., 2009; Wu et al., 2010), but contrasts with the findings of Smith et al. (2007), although we expect this difference, in part, is due to issues with the full integrated light (nucleus and outer regions from the galaxies in our IRS sample fall within the IRS aperture in constrast to the sample of Smith et al., 2007).

from an off-axis region of an AGN host galaxy have no significant differences from SINGS H II galaxies' PAH ratios. As discussed in Section 2.5.4, the 11.3μm feature is relatively unaffected by AGN, which could explain the lower ratios seen by Smith et al. (2007). The other studies also have samples that would remain relatively unchanged over their respective ranges of hardness ratios (O'Dowd et al., 2009; Wu et al., 2010, $z_{med} = 0.08$ and normal SF galaxies and $0.008 < z < 4.27$, respectively).

2.5.7 The Distribution of the 6.2μm PAH Equivalent Width

Previous studies use the equivalent width (EW) of the 6.2μm PAH feature to classify sources as AGN, starbursts (SBs), and composite AGN+SB subsamples (e.g., Wu et al., 2010). Sources where an AGN dominates the IR emission are expected to have lower 6.2μm PAH EW either because the mid-IR continuum from the AGN is much stronger and washes out the emission, or because the ionization field of the AGN destroys the PAH molecules, or a combination of the two. The EW measures the relative strength of the PAH feature to the mid-IR continuum, thereby allowing us to quantify the effects of an AGN.

Figure 2.11 shows the PAH 6.2μm EW versus the 7.7–to–11.3μm PAH flux ratio. The red dashed line shows a selection for AGN with EW $\leq$ 0.2μm, the blue dashed line shows a selection for SB galaxies with EW $>$ 0.5μm, and AGN+SB composite sources populate the region between these regions (Armus et al., 2007, EWs are given in table 2.5). Most of the IRAGN (defined by the IRAC color-color selection) have low 6.2μm EW: 12 of the 14 IRAGN satisfy either the composite or AGN 6.2μm PAH EW criteria. Similarly, most of the non-IRAGN have high 6.2μm EW: 46 of 51 non-IRAGN satisfy the SB 6.2μm PAH EW criterion. Interestingly, the figure shows no correlation between the 6.2μm EW and $L_{7.7\mu m}/L_{11.3\mu m}$ ratio. A similar observation is shown for the $L_{7.7\mu m}/L_{11.3\mu m}$ ratio compared to the hardness of the

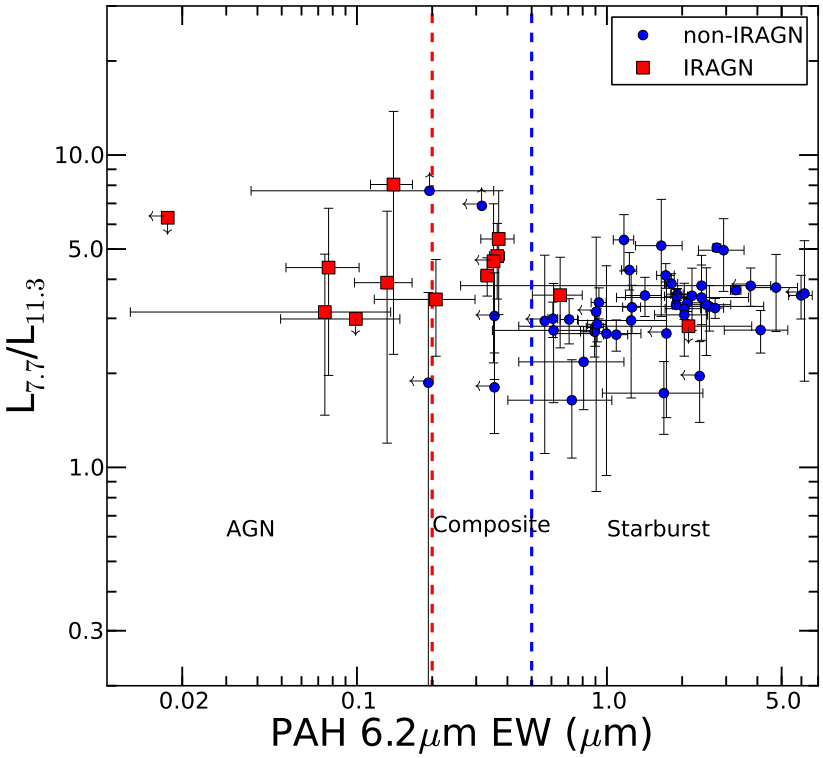

Figure 2.11 — PAH 6.2μm equivalent width versus the $L_{7.7}/L_{11.3}$ PAH ratio. The dashed lines show selection criteria to separate sources into AGN, composite, and SB galaxies, as labeled in the figure. Galaxies with EW $\leq$ 0.2 μm are likely AGN (red-dashed line), galaxies with EW $>$ 0.5 μm are SB galaxies (blue-dashed line), and galaxies that fall between these lines are likely AGN+SB composites. We observe no correlation between $L_{7.7}/L_{11.3}$ and the EW of the 6.2μm PAH feature.

radiation field in figure 2.10 (see section 2.5.6). Therefore, we see no indication that the presence of an AGN affects the $L_{7.7\mu m}/L_{11.3\mu m}$ ratio. If the AGN were photoionizing the PAH molecules; and reducing the 6.2μm EW, we would expect the $L_{7.7\mu m}/L_{11.3\mu m}$ ratio to decrease with decreasing 6.2μm EW. Because we do not, we conclude that the AGN decreases the PAH 6.2μm EW because the AGN increases the mid-IR continuum, and not because the AGN destroys the PAH molecules on a galaxy wide scale (see section 2.6.3).

Table 2.5. Equivalent Widths for Various PAH Emission Features

ID	$EW_{6.2}$	$EW_{7.7}$	$EW_{8.6}$	$EW_{11.3}$
1	1.96 ± 0.22	4.46 ± 0.20	3.99 ± 0.11	0.07 ± 0.01
2	0.02 ± 0.03	0.41 ± 0.12	0.05 ± 0.04	0.09 ± 0.02
3	0.02 ± 0.07	0.60 ± 0.22	0.27 ± 0.05	0.10 ± 0.01
4	0.36 ± 0.03	1.76 ± 0.11	0.76 ± 0.05	0.52 ± 0.04
5	2.57 ± 1.67	7.03 ± 1.88	2.39 ± 0.36	2.54 ± 0.14
6	0.56 ± 2.56	2.58 ± 1.51	0.64 ± 0.51	0.64 ± 0.09
7	0.33 ± 0.02	2.23 ± 0.12	0.91 ± 0.05	1.42 ± 0.09
8	1.81 ± 0.11	5.99 ± 0.30	1.65 ± 0.06	1.54 ± 0.03
9	2.39 ± 1.30	6.09 ± 1.72	2.33 ± 0.46	2.34 ± 0.25
10	1.25 ± 0.48	3.63 ± 0.98	1.43 ± 0.30	2.23 ± 0.29
11	5.98 ± 0.65	9.76 ± 0.90	2.62 ± 0.20	2.11 ± 0.11
12	0.14 ± 0.03	1.09 ± 0.10	0.26 ± 0.04	0.17 ± 0.02
13	1.72 ± 0.14	6.84 ± 0.66	2.55 ± 0.17	2.93 ± 0.08
14	1.69 ± 0.73	4.08 ± 0.95	1.96 ± 0.36	4.03 ± 0.40
15	2.19 ± 4.17	6.45 ± 3.07	2.21 ± 0.50	2.37 ± 0.17
16	0.10 ± 0.05	0.47 ± 0.10	0.07 ± 0.04	0.20 ± 0.03
17	2.12 ± 1.68	2.63 ± 0.98	0.84 ± 0.31	0.53 ± 0.10
18	0.71 ± 0.06	1.72 ± 0.10	0.82 ± 0.04	0.98 ± 0.03
19	0.91 ± 64.86	4.04 ± 60.40	1.38 ± 5.30	1.68 ± 0.62
20	1.90 ± 0.20	5.43 ± 0.28	1.71 ± 0.04	1.75 ± 0.12
21	1.42 ± 0.23	5.73 ± 0.99	2.23 ± 0.29	2.67 ± 0.30
22	3.28 ± 0.16	10.27 ± 0.23	3.01 ± 0.04	1.91 ± 0.02
23	2.75 ± 0.07	10.80 ± 0.24	3.14 ± 0.05	2.55 ± 0.02
24	0.08 ± 0.03	0.68 ± 0.09	0.35 ± 0.04	0.30 ± 0.02
25	2.10 ± 0.27	6.26 ± 0.37	25.87 ± 0.06	25.86 ± 0.03
26	0.65 ± 0.15	2.60 ± 0.27	0.85 ± 0.07	0.84 ± 0.04
27	1.91 ± 0.11	7.41 ± 0.24	2.40 ± 0.05	1.51 ± 0.03
28	0.93 ± 0.06	3.64 ± 0.31	1.41 ± 0.08	2.35 ± 0.10
29	1.23 ± 0.09	5.30 ± 0.36	2.02 ± 0.13	1.92 ± 0.12
30	0.61 ± 0.03	2.51 ± 0.15	1.20 ± 0.06	1.86 ± 0.06
31	0.35 ± 0.66	1.04 ± 0.90	0.51 ± 0.27	1.33 ± 0.14
32	0.81 ± 0.36	2.10 ± 0.51	0.97 ± 0.12	1.76 ± 0.09
33	0.13 ± 0.03	0.58 ± 0.08	0.24 ± 0.04	0.20 ± 0.02
34	0.32 ± 1.20	2.68 ± 1.06	1.29 ± 0.30	0.21 ± 0.06
35	0.90 ± 0.07	3.18 ± 0.24	1.20 ± 0.07	1.74 ± 0.05
36	0.35 ± 0.36	1.41 ± 0.61	0.48 ± 0.17	0.77 ± 0.10
37	2.50 ± 0.63	6.61 ± 1.26	1.59 ± 0.31	1.69 ± 0.24
38	1.89 ± 0.06	7.01 ± 0.16	1.88 ± 0.03	38.14 ± 0.01
39	0.35 ± 2.53	2.00 ± 1.93	0.95 ± 0.54	0.84 ± 0.13
40	6.17 ± 7.58	8.36 ± 4.45	2.21 ± 0.88	1.33 ± 0.23
41	0.72 ± 0.32	2.68 ± 0.56	1.01 ± 0.18	3.20 ± 0.25
42	2.93 ± 0.61	7.50 ± 0.97	2.29 ± 0.22	1.12 ± 0.14
43	1.17 ± 0.11	4.05 ± 0.30	1.13 ± 0.06	0.86 ± 0.05
44	0.07 ± 0.06	0.64 ± 0.30	0.05 ± 0.13	0.25 ± 0.02
45	0.61 ± 0.26	1.84 ± 0.39	0.71 ± 0.10	0.88 ± 0.05
46	2.04 ± 0.33	7.26 ± 0.67	2.32 ± 0.13	1.97 ± 0.14
47	1.73 ± 10.84	5.96 ± 6.75	4.64 ± 2.36	4.56 ± 0.69
48	0.25 ± 1.00	0.19 ± 0.47	0.21 ± 0.26	0.01 ± 0.06
49	2.39 ± 2.13	13.13 ± 2.43	3.25 ± 0.43	2.06 ± 0.22
50	0.19 ± 10.89	1.74 ± 27.35	0.97 ± 4.52	1.30 ± 0.45
51	2.71 ± 0.51	7.61 ± 0.39	2.52 ± 0.09	2.30 ± 0.04
52	0.91 ± 0.08	2.76 ± 0.38	1.27 ± 0.11	2.18 ± 0.17
53	1.00 ± 0.37	2.97 ± 0.58	0.90 ± 0.15	1.20 ± 0.10
54	1.26 ± 0.10	4.08 ± 0.25	1.09 ± 0.06	1.09 ± 0.04
55	2.35 ± 2.39	4.32 ± 1.61	1.50 ± 0.33	2.54 ± 0.26
56	2.04 ± 0.49	4.47 ± 0.68	1.85 ± 0.21	2.35 ± 0.14
57	1.65 ± 0.35	3.91 ± 0.52	1.57 ± 0.57	0.98 ± 0.10
58	4.12 ± 1.17	8.85 ± 1.27	2.64 ± 0.27	2.97 ± 0.15
59	0.20 ± 0.16	0.85 ± 0.18	0.54 ± 0.09	0.15 ± 0.03

Table 2.5 (cont'd)

ID	$EW_{6.2}$	$EW_{7.7}$	$EW_{8.6}$	$EW_{11.3}$
60	0.21 ± 0.09	0.71 ± 0.15	0.33 ± 0.06	0.39 ± 0.03
61	0.37 ± 0.06	1.92 ± 0.15	0.95 ± 0.07	0.49 ± 0.03
62	1.09 ± 0.12	4.02 ± 0.42	1.47 ± 0.10	2.26 ± 0.06
63	3.76 ± 3.92	11.72 ± 2.02	2.92 ± 0.28	1.22 ± 0.04
64	0.89 ± 0.11	2.79 ± 0.25	0.92 ± 0.06	1.41 ± 0.04
65	4.75 ± 1.04	6.75 ± 1.18	2.09 ± 0.29	1.53 ± 0.10

Note. — Equivalent widths are from PAHFIT spectral decomposition results and the errors were done using monte carlo simulations and running through PAHFIT to get uncertainties. Values given as (...) do not have a measured flux from PAHFIT spectral decomposition.

2.5.8 The Relationship Between PAH Luminosity, Star-formation Rate, and AGN Luminosity

As discussed above, the [Ne II] and the [O IV] emission lines are useful probes of the SFR and AGN luminosity, respectively. In figure 2.12, we plot the flux measured in the [Ne II] and [O IV] lines against the summed flux from the 7.7μm and 11.3μm PAH features, which we are able to then compare directly against results from Diamond-Stanic & Rieke (2010). The [Ne II] emission correlates strongly with PAH emission, with a Spearman correlation coefficient of $\rho = 0.94$ and a linear fit of $F([\text{Ne II}]) = 0.02 \times {F_{7.7+11.3}}^{0.99}$. The scatter in the [Ne II]–PAH relation increases for fainter fluxes, which may be related to the presence of IRAGN, which are more frequent in the sample at faint line fluxes.

In contrast, the [O IV] line shows almost no correlation with PAH emission, with a Spearman correlation coefficient of $\rho = 0.19$. Because [Ne II] correlates so well with the PAH emission, the relation in figure 2.12 suggests that the PAH emission correlates with the SFR. This is consistent with the findings of Diamond-Stanic & Rieke (2010) and Genzel et al. (1998). We also do not see any clear difference between the IRAGN and non-IRAGN in either the [Ne II] or [O IV] versus PAH emission

plot in figure 2.12, indicating further that the PAH features are likely tracing star formation in both subsamples, and that the presence of AGN do not increase (or decrease) PAH emission integrated over galaxies (Diamond-Stanic & Rieke, 2010).

The bottom panel in figure 2.12 shows a swath of eight galaxies with low PAH emission and high [O IV] emission. These galaxies lie above the upper dashed line, which is 4 times greater than the fit to the non-IRAGN (lower dashed line). Approximately one-half (5/11[3]) of the IRAGN have [O IV] emission above this line. In addition, three of the galaxies above this line are non-IRAGN. Removing these galaxies from the sample shows a correlation may be present (Spearman's $\rho = 0.60$) for galaxies without strong [O IV] emission. As stated in Section 2.3.3, the Stern et al. (2005) IRAC color-color method used to identify IRAGN selects more broad-line AGN, but only about 40% of narrow-lined AGN. Because excess [O IV] indicates the presence of ionization from an AGN, these three non-IRAGN galaxies likely harbor heavily-obscured AGN that are missed by the IRAGN selection.

2.6 Discussion

2.6.1 The Color-Magnitude Diagram for IR Luminous Galaxies

Because our IRS sample spans a nearly uniform distribution in optical color, we are able to study differences in the IR emission properties of galaxies with different positions on the optical color-magnitude relation. For the full sample (all galaxies in AGES with $f(24\mu\text{m}) > 1.2$ mJy and $0.02 < z < 0.6$, including both the IRAGN and non-IRAGN), we find the median values are $M(r)_{0.1}$ = -20.36 mag and $(u-r)_{0.1}$ = 1.97 mag. These differ from the median values for our IRS sample, which are $M(r)_{0.1}$ = -20.74 mag and $(u-r)_{0.1}$ = 2.23 mag). We attribute these differences

[3]Three do not have [O IV] detections due to the redshift of the source.

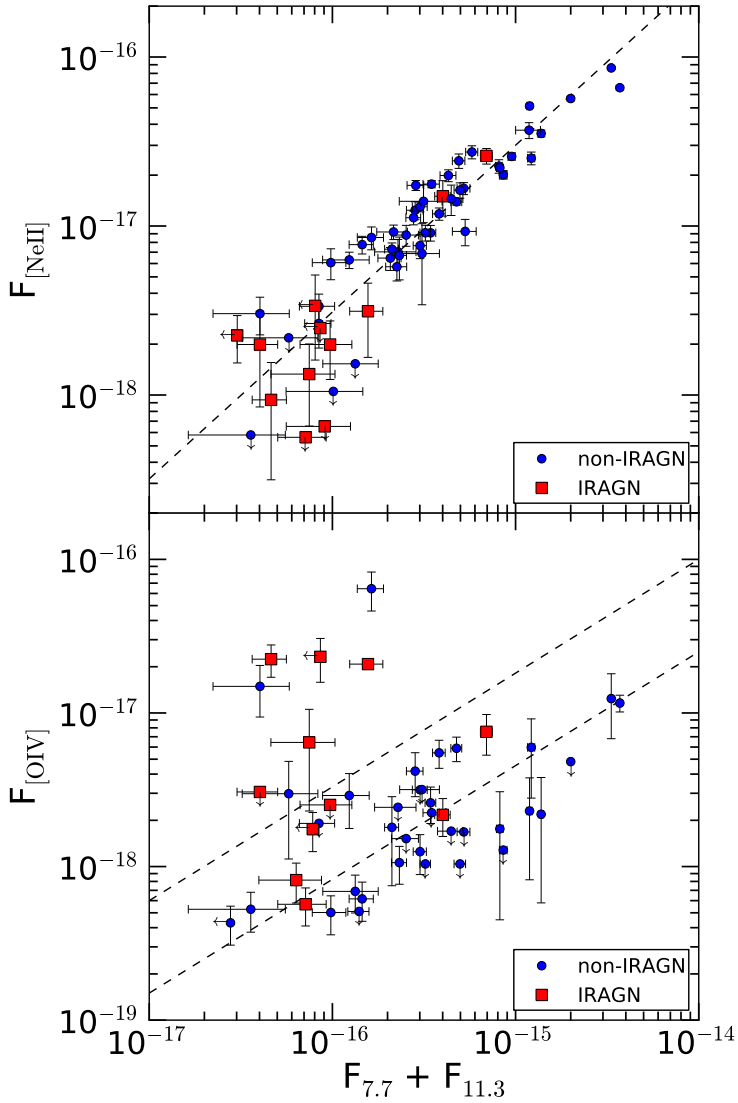

Figure 2.12 — The relationship between the PAH emission features and the [Ne II] (top panel) and [O IV] (bottom panel) emission lines. All units are in W/m^2. The top panel shows a correlation between the PAH emission and [Ne II] emission line suggesting PAH emission correlates with star formation. The dashed line represents a linear fit ($0.02\times F_{7.7+11.3}{}^{0.99}$) to the sample. The bottom panel shows that there is little, if any, correlation between PAH emission and [O IV], but there is a population of objects with low PAH emission and excess [O IV] emission. The upper dashed line is four times greater than the fit to the non-IRAGN subsample (lower dashed line) used to select the [O IV]-excess objects.

to the fact that our IRS sample has a uniform selection in $(u-r)_{0.1}$ optical color whereas the full sample is weighted toward bluer $(u-r)_{0.1}$ optical colors. In figure 2.13, we replot the location of the IR-luminous galaxies on the optical $M(r)_{0.1}$ versus $(u-r)_{0.1}$ color-magnitude diagram, and we denote galaxies by their IR luminosity as derived from their MIPS data (see section 2.5.2) in coarse bins of luminosity: low-luminosity galaxies ($L_{IR} = 10^{10} - 2.4 \times 10^{11}$ $L_{\odot}$), medium-luminosity ($L_{IR} = 2.4 \times 10^{11} - 4.5 \times 10^{11}$ $L_{\odot}$) and high-luminosity ($L_{IR} > 4.5 \times 10^{11}$ $L_{\odot}$), evenly splitting the medium and high luminosity bins ($\sim$100 galaxies for each bin) for the full sample to improve the statistics for comparison[4]. Using the full sample of galaxies with $f(24\mu m) > 1.2$ mJy, we find no difference in $(u-r)_{0.1}$ color as a function of IR luminosity. Each of the three IR luminosity bins have nearly equal median colors $(u-r)_{0.1} = 2.0$ mag with similar interquartile ranges. The only difference we measure is that the $(u-r)_{0.1}$ color distribution of the highest IR luminosities is slightly broader than for the lower luminosity galaxies.

In comparison, our IRS sample shows the low, medium and high-luminosity galaxies are also mostly distributed evenly in the color-magnitude relation. We observe slight evidence that the $(u-r)_{0.1}$ color *decreases* for *increasing* IR luminosity. We find the median $(u-r)_{0.1}$ colors are 2.34 mag, 2.25 mag, and 1.96 mag for the low, medium, and high-luminosity galaxies, respectively. However, we consider this trend not to be significant given the lack of any correlation in the full sample.

We compared the $(u-r)_{0.1}$ color distributions for galaxies classified as IRAGN and non-IRAGN from the full sample of galaxies with $f(24\mu m) > 1.2$ mJy from AGES (cyan points in figure 2.13). The median values, $M(r)_{0.1} \sim$ -20.34 mag and $(u-r)_{0.1} \sim 2.00$ mag for the IRAGN and for the non-IRAGN $M(r)_{0.1} \sim$ -20.36 mag

[4]If we use the traditional ULIRG identification ($L_{IR} > 10^{12} L_{\odot}$) for the full sample, we have only 9 galaxies for comparison.

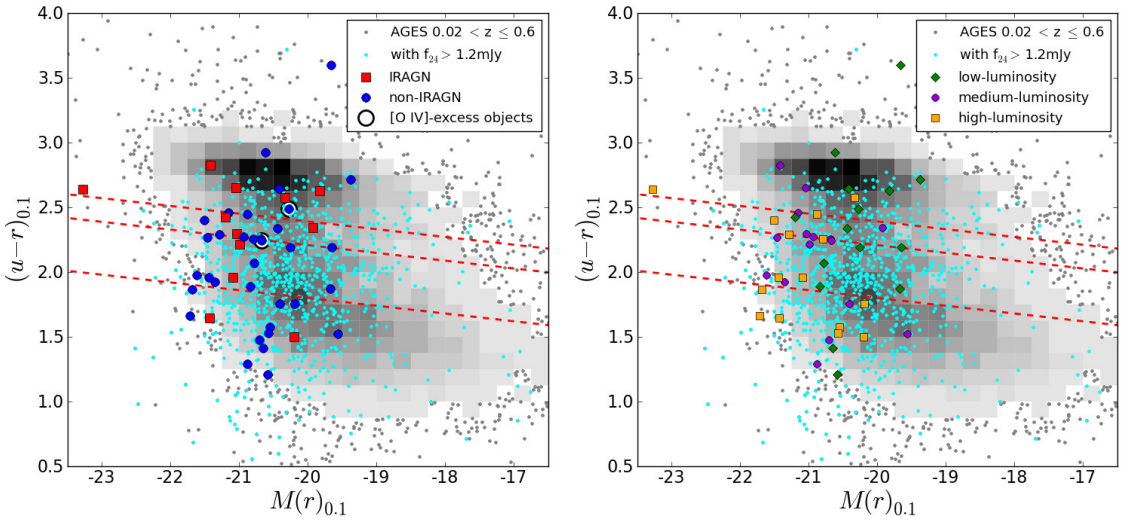

Figure 2.13 — Optical $(u-r)_{0.1}$ color-magnitude diagram. Both plots are similar to figure 2.1 except for symbol changes to the Boötes IRS sample. (*Top Panel*) The sample symbols denote IRAGN (red squares), non-IRAGN (blue circles), and non-IRAGN galaxies with excess [O IV] (defined in section 2.5.8, black open circles). (*Bottom Panel*) The sample symbols denote galaxy IR luminosity as low-luminosity galaxies ($L_{IR} = 10^{10} - 2.4 \times 10^{11}$ $L_{\odot}$, green diamonds), medium-luminosity galaxies ($L_{IR} = 2.4 \times 10^{11} - 4.5 \times 10^{11}$ $L_{\odot}$, purple circles), and high-luminosity galaxies ($L_{IR} > 4.5 \times 10^{11} L_{\odot}$, orange squares).

and $(u-r)_{0.1} \sim 1.96$ mag are similar. A K-S test applied to the distributions gives a D-statistic = 0.06 and a likelihood of 74.8%, which we interpret as evidence that there is no difference between the $(u-r)_{0.1}$ colors for IR luminous galaxies selected as IRAGN and non-IRAGN.

Considering only our IRS sample, the IRAGN span the range from the blue cloud to the red sequence, where 67% (8 of 12) are located in the "green valley" or the red sequence ($(u-r)_{0.1} + 3/50 \times (M[r]_{0.1} + 20) > 2.18$). The distribution of $(u-r)_{0.1}$ color for the non-IRAGN galaxies appears shifted toward bluer colors compared to the IRAGN. We find that the median $(u-r)_{0.1}$ color for the non-IRAGN is 2.13 mag compared to the median color for the IRAGN, 2.38 mag, shown in figure 2.13. However, because we see no difference between IRAGN and non-IRAGN in the full sample of IR luminous galaxies, we do not consider these differences significant.

Other studies of the optical colors for AGN have found that they populate a similar region of the color-magnitude relation compared to our IRAGN samples here (Nandra et al., 2007; Weiner et al., 2007). While our IRAGN span a similar $(u-r)_{0.1}$ color range as X-ray selected AGN (e.g. Nandra et al., 2007), so do the non-IRAGN. So it is unclear if the presence of an AGN is driving redder $(u-r)_{0.1}$ colors in our IRS sample of IR luminous galaxies. Therefore, in galaxies selected to be IR luminous (with $f(24\mu\text{m}) > 1.2$ mJy), there is no measurable difference between the optical $(u-r)_{0.1}$ colors for galaxies selected as IRAGN and non-IRAGN.

However, there is a difference in our interpretation of the $(u-r)_{0.1}$ colors for the IRAGN and non-IRAGN. Most of the IRAGN in our IRS sample have low [Ne II] and PAH luminosities, which may imply they have significantly lower SFRs compared to the non-IRAGN (figures 2.12 and 2.14). Therefore, the fact that the IRAGN in our samples lie in the "green valley" or red sequence may imply they have declining SFRs or a recent cessation of star-formation, similar to conclusions reached by Nandra et al.

(2007). This also implies that star-formation is not a necessary component for an AGN to persist.

2.6.2 AGN Effects on PAH Emission and AGN Contribution to L_{IR}

Previous studies have used anticorrelations in the [Ne III]/[Ne II] versus $L_{7.7\mu m}/L_{11.3\mu m}$ ratios (see figure 2.10) to conclude that galaxies with an increasing hardness of radiation field from an AGN have relatively less emission from shorter wavelength PAH features compared to longer wavelength PAH features (e.g. Smith et al., 2007; O'Dowd et al., 2009; Wu et al., 2010). One interpretation is that the smaller PAH molecules are preferentially destroyed in the presence of the AGN (Smith et al., 2007; O'Dowd et al., 2009). It is certainly the case that AGN do not *increase* PAH emission, as shown in figure 2.12 (see also Diamond-Stanic & Rieke, 2010).

In our sample, the luminosity for all PAH features is uniformly weaker in the IRAGN galaxies compared to the non-IRAGN and uniformly less frequent (see figures 2.5 and 8). Figure 2.5 shows that the mid-IR SEDs of the IRAGN in our sample show a weakly rising continuum with increasing wavelength (with possible silicate absorption at 9.7μm). Figure 2.12 shows that most of the IRAGN galaxies in our sample have low [Ne II] emission and PAH emission. Therefore, the IRAGN appear to have lower implied SFRs. Taken together, the data suggest that the reason IRAGN in our sample have lower PAH emission is a combination of higher mid-IR continuum from processes associated with the AGN combined with intrinsically lower SFRs. It is unclear if the AGN actually destroy PAH molecules but given the low [Ne II] fluxes, it seems more likely the lack of PAH emission is because the hosts of IRAGN have lower SFRs. It is possible that some other feedback mechanism from the AGN affects the SFR. We also have to be cautious about the selection effect for IRAGN that the AGN will boost the flux at 24μm and will select on a lower

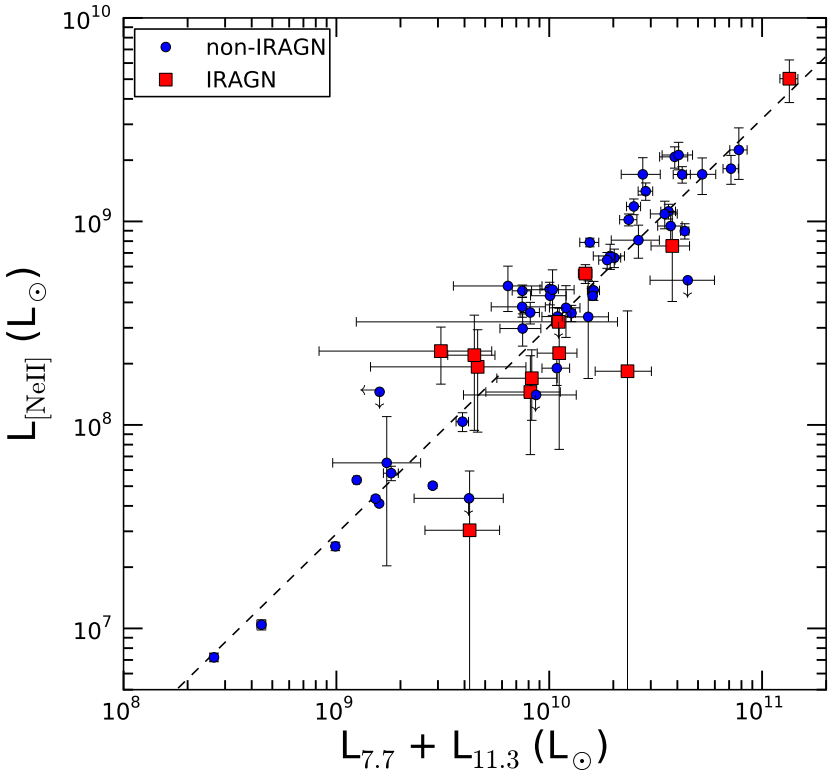

Figure 2.14 — The relationship between the luminosity of the PAH emission features and the [Ne II] emission line. The [Ne II] luminosity correlates strongly with the PAH luminosity, with a Spearman correlation coefficient of $\rho = 0.90$ and a linear fit (dashed line) of Log(L[Ne II]) = 1.02 ± 0.03 × Log($L_{7.7+11.3}$) - 1.71 ± 0.25.

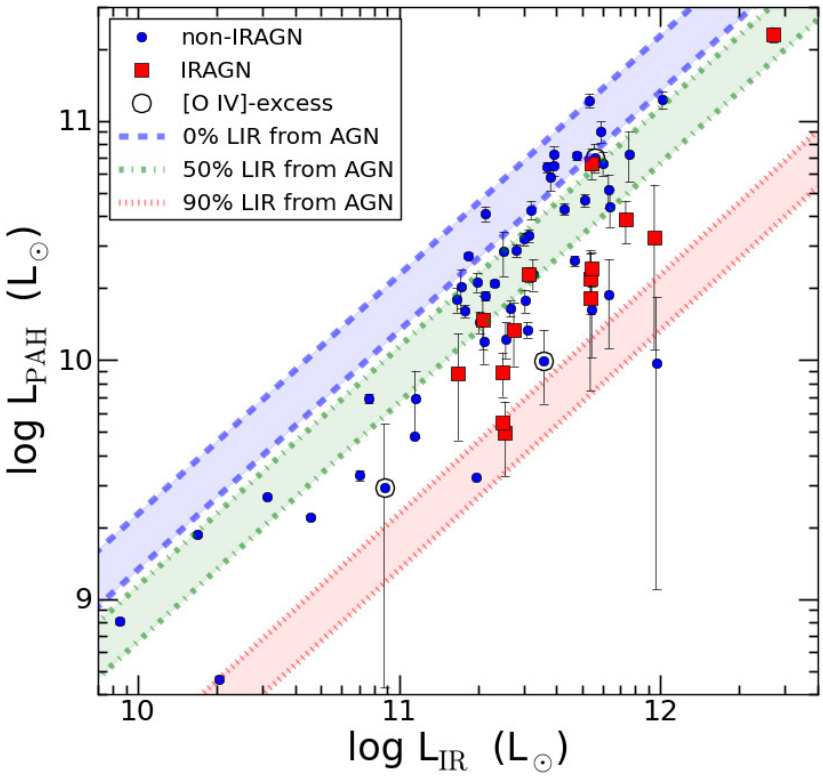

Figure 2.15 — The total IR luminosity versus the PAH luminosity as an indicator for the contribution of AGN luminosity to the L_{IR}. The shaded regions represent percent amounts, marked in the plot, for the contribution of AGN luminosity to the total IR luminosity for the IRAGN in our sample under the assumption that the PAH luminosity traces the total SFR (see section 2.6.2 for explanation).

star-formation threshold than a purely star-forming sample. Thus, this may result in weaker observed PAH emission for the IRAGN.

Figure 2.14 shows that the PAH luminosity correlates linearly with the [Ne II] luminosity (linear fit of Log(L[Ne II]) = 1.02 ± 0.03 × Log($L_{7.7+11.3}$) - 1.71 ± 0.25). Because the correlation is linear, we conclude that both are good tracers of the total SFR (Ho & Keto, 2007). We can then use the PAH luminosity and total IR luminosity to estimate the contribution of star-formation and AGN luminosity to the total IR luminosity for the IRAGN in our sample. In figure 2.15, we show our

estimated contribution of AGN luminosity to the total IR luminosity for the IRAGN. We make the implicit assumption that the non-IRAGN galaxies with the highest L_{PAH}/L_{IR} ratios have no contribution from AGN luminosity to their L_{IR}. Under this assumption the contribution of AGN to the IR luminosity is a lower limit, and could be higher by a *systematic* amount. However, the relative contribution of an AGN to the IR luminosity is robust under this assumption. Using this premise, we define our 0% AGN luminosity contribution for the IRAGN by fitting the range of the L_{PAH}/L_{IR} ratios for the upper quartile of non-IRAGN galaxies with $L_{IR} \geq 10^{11} L_{\odot}$ using a unity relation between the two luminosities. The shaded region represents the range of scatter in our sample as to which galaxies are completely star-forming. Using this definition, we attribute 50-90% of the total IR luminosity in the IRAGN to an AGN rather than star-formation (a similar result to Petric et al., 2011; Schweitzer et al., 2006; Veilleux et al., 2009, from studies of LIRGs, ULIRGs, and QSOs), except for one object where the AGN contributes $< 50\%$ of the total IR luminosity (and has one of the highest [Ne II] luminosities of the IRAGN). While star-formation is a significant contribution to the total IR luminosity for the IRAGN, the AGN is the dominant source of IR luminosity in these galaxies.

2.6.3 Emission Ratios of Short-to-Long Wavelength PAHs in IRAGN and non-IRAGN

O'Dowd et al. (2009) showed that the AGN in their sample have significantly lower $L_{7.7\mu m}/L_{11.3\mu m}$ values than the SF galaxies (similar to conclusions from Wu et al., 2010). Both O'Dowd et al. and Wu et al. found no significant difference in the $L_{6.2\mu m}/L_{7.7\mu m}$ ratio going from galaxies dominated by star-formation to those dominated by an AGN. Taken together, these observations suggest that galaxies with AGN show a reduction in the emission of shorter wavelength PAHs relative to longer

wavelength PAHs. In contrast, we see no difference in either the $L_{7.7\mu m}/L_{11.3\mu m}$ or $L_{6.2\mu m}/L_{7.7\mu m}$ ratio for the IRAGN and non-IRAGN in our sample. Here we discuss possible reasons for the differences seen between the samples.

As noted above, previous studies argued that the smaller dust grains responsible for the shorter wavelength PAH molecules are preferentially destroyed in the presence of an AGN (Smith et al., 2007; O'Dowd et al., 2009; Wu et al., 2010). Diamond-Stanic & Rieke (2010) investigated possible destruction of PAH grains by AGN-driven shocks as X-ray heating was shown not to be as important as shock excitation (Roussel et al., 2007). While the effects of AGN-driven shocks on the observed PAH emission are complex and uncertain, one possible effect is that shocks leave uneven structures in the surviving dust grains that do not contribute to the PAH emission. However, Diamond-Stanic & Rieke (2010) noted that the molecules responsible for the 11.3μm feature are not strongly suppressed by shocks, and this can explain the observed lower $L_{7.7\mu m}/L_{11.3\mu m}$ ratios.

Diamond-Stanic & Rieke (2010) also found that AGN-dominated sources (the nuclei of local Seyfert galaxies) with low $L_{7.7\mu m}/L_{11.3\mu m}$ ratios have strong H_2 emission (H_2 S(3) rotational line at 9.67μm) indicating the presence of shocks[5]. This is consistent with observations of Roussel et al. (2007) and Smith et al. (2007) who observe stronger H_2 emission and lower $L_{7.7\mu m}/L_{11.3\mu m}$ ratios in local galaxies with AGN from SINGS. We do not have many sources with detected H_2 emission in the 9.67μm line (10/65 galaxies have H_2 flux detections at $\geq 3\sigma$). This suggests that, if shocks are present, they may not be strong enough to modify the short-to-long PAH ratios observed or to produce strong emission in this H_2 line.

As our sample has the highest median redshift ($z_{med} = 0.28$) of other recent studies

[5]refer to Diamond-Stanic & Rieke (2010) for further description of other studies with similar results

(O'Dowd et al., 2009; Wu et al., 2010, $z_{med} = 0.08$ and $z_{med} = 0.144$, respectively) we view more integrated light from a galaxy and this may result in a significant difference not associated with the effects of an AGN. The discussion above only takes into account the differences seen between active galaxies and SF galaxies in short-to-long PAH ratios. As O'Dowd et al. (2009) discuss, the age and evolution of metallicity in a galaxy can also have an effect on the observed short-to-long PAH ratios.

2.6.4 Galaxies with Excess [O IV] λ25.9μm Emission

Eight galaxies in our IRS sample show unusually high [O IV] emission relative to their PAH luminosities (figure 2.12), including three galaxies classified as non-IRAGNs (IDs 6, 50, and 55). The excess [O IV] indicates the presence of a hard ionizing field, mostly likely from an AGN that is otherwise undetected in the IR. Here we discuss these "[O IV]-excess" objects in detail.

Figure 2.16 shows the IRS spectra of all three galaxies (IDs 6, 50, and 55). Both galaxies IDs 6 and 50 have spectra similar to the IRAGN composite spectrum (figure 2.5) and the spectra of the other IRAGN (figure 2.4), in our sample. In contrast, galaxy ID 55 has an IRS spectrum more characteristic of the other non-IRAGN (see figures 2.4 and 2.5).

We looked for other indications of obscured AGN in the optical spectroscopy (see figure 2.17) of galaxy IDs 6 and 50, both of which have optical spectra from AGES (galaxy ID 55 lies in the FLS and has optical spectra from Papovich et al. 2006, but the spectral coverage does not extend to Hα and [N II]). We show the portion of the optical spectrum covering the emission lines of [O III] λ5007Å, Hβ λ4861Å, [N II] λ6583Å, and Hα λ6563Å. The optical spectra of all three galaxies (IDs 6, 50, and 55) are typical of star-forming galaxies, and therefore the AGN in these

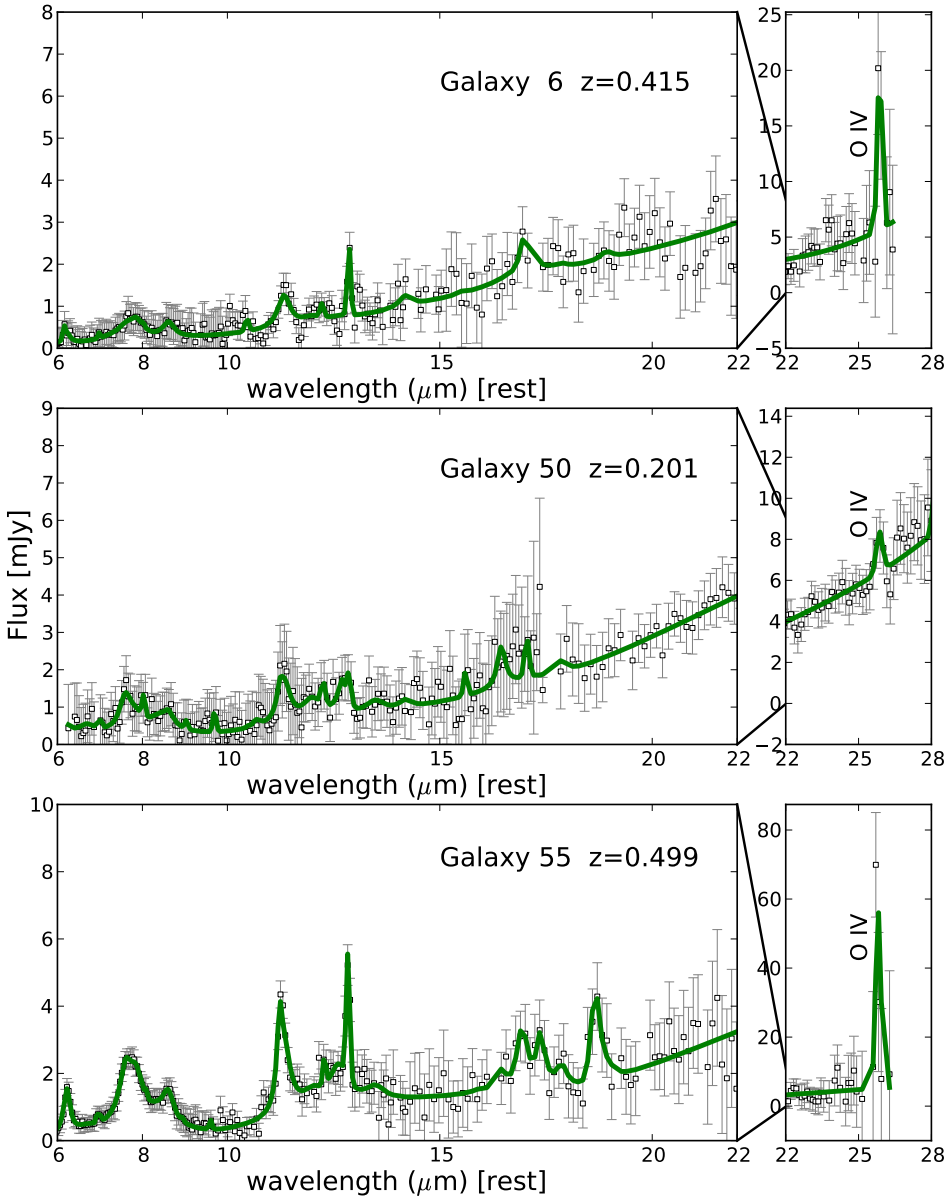

Figure 2.16 — The IRS mid-IR spectra of three non-IRAGN galaxies in our IRS sample with excess [O IV] emission and no other indications of an AGN. The continuous spectrum of each galaxy is shown, but split to better show the spectrum and excess [O IV] emission. Note range of y-axis differs from left to right panel for each spectrum. The open circles are the measured flux densities from the *Spitzer* IRS data observations with error bars representing the uncertainties in those measurements and the green line represents the best fit from spectral decomposition of PAHFIT. All three galaxies show clear emission from [O IV] at 25.9μm.

galaxies must be very obscured. Using an optical Baldwin, Phillips, and Terlevich (BPT) classification (Kewley et al., 2001; Kauffmann et al., 2003) of the galaxies, the galaxies would likely be classified as either star-forming or composite sources. Galaxy ID 50 has all four emission lines used for optical classification and is the most likely source showing any indication of an AGN being present in its optical spectrum.

Of the three non-IRAGN with unusually high [O IV] emission (figure 2.12, bottom panel), galaxy IDs 6 and 50 both have low L_{PAH}/L_{LIR} ratios, and are quite similar to the values observed in the IRAGN. Galaxy ID 55 has one of the highest L_{PAH}/L_{LIR} ratios in the entire IRS sample. As expected, galaxy IDs 6 and 50 both have low [Ne II] luminosities similar to the five IRAGN with high [O IV] emission (and most of the IRAGN, shown in figure 2.12). Further evidence for galaxy IDs 6 and 50 being obscured AGN may be seen in that they have optical colors and magnitudes located in the "green valley", similar to the other IRAGN. Furthermore, galaxy No. 55 is about the same as the median value of the non-IRAGN subsample's [Ne II] luminosity (refer to table 2.2 for fitted flux values). Therefore, galaxy ID 55 is clearly a candidate for an IR-luminous galaxy with a deeply obscured AGN that is otherwise undetected. Further studies of these galaxies would allow for tests of galaxies with deeply obscured AGN, including multi-wavelength observations.

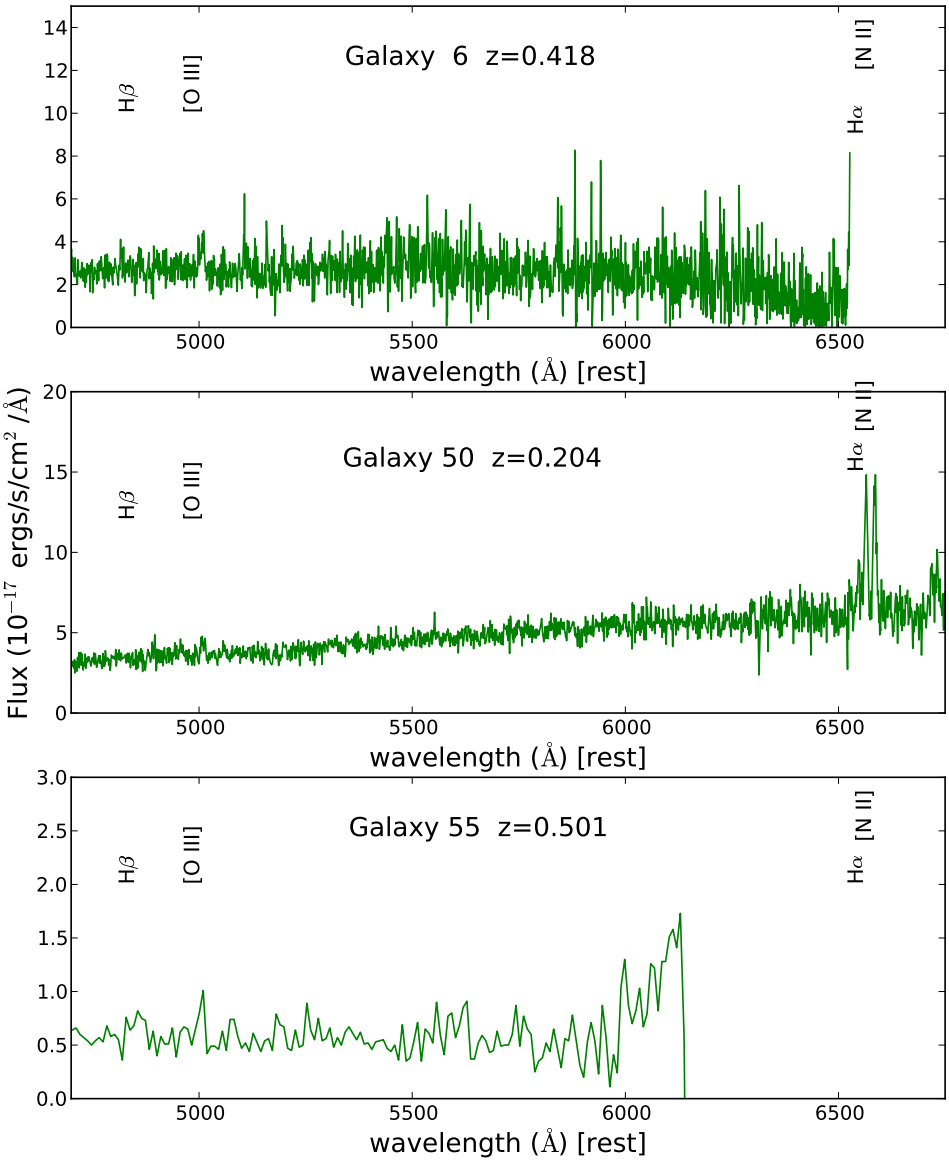

Figure 2.17 — The optical spectra of three non-IRAGN galaxies in our IRS sample with excess [O IV] emission and no other indications of an AGN. Galaxy IDs 6 and 50 are optical spectra from AGES. Galaxy 55 is from the FLS and has an optical spectrum from Papovich et al. (2006). The emission lines of [O III] λ5007Å, Hβ λ4861Å, [N II] λ6583Å, and Hα λ6563Å have been marked to indicate the atomic lines used for optical classification of galaxies as star-forming, composite, or AGN (Kewley et al., 2001; Kauffmann et al., 2003). The redshifts listed for each galaxy are the given optical redshifts from AGES (see table 2.1).

3. A NEW STAR-FORMATION RATE CALIBRATION FROM POLYCYCLIC AROMATIC HYDROCARBON EMISSION FEATURES: APPLICATION TO HIGH REDSHIFT GALAXIES

3.1 Background

Star-formation is a fundamental property of galaxy formation and evolution. Understanding the exact rate of star-formation and how it evolves with time and galaxy mass has deep implications for how galaxies form. Measuring accurate star-formation rates (SFRs) through cosmic time is therefore paramount for understanding galaxy evolution itself. Much work has been applied to calibrating emission from the UV, nebular emission lines, far-IR, X-ray and radio as tracers of the SFR in distant galaxies (see the review by Kennicutt & Evans, 2012).

Previous studies of deep Infrared (IR) surveys with the *Spitzer* and *Herschel* Space Telescopes have revealed that the majority of star-formation at redshifts of z $\sim 1-3$ occurs in dust enshrouded galaxies (e.g. Elbaz et al., 2011; Murphy et al., 2011); and that luminous IR galaxies (LIRGs; L $\gtrsim$ $\times 10^{11}$ $L_{\odot}$) are much more prevalent during this epoch ($1 < z < 3$) than today (Chary & Elbaz, 2001; Pérez-González et al., 2005; Magnelli et al., 2009; Murphy et al., 2011; Elbaz et al., 2011; Lutz, 2014, and references therein). This epoch is also particularly interesting as it corresponds to the peak cosmic SFR density in the universe (Madau & Dickinson, 2014, and references therein). Therefore, it is important to be able to measure accurately SFRs of heavily obscured galaxies. But this becomes challenging at high redshifts or when galaxies contain active galactic nuclei (AGN), because most of the familiar SFR diagnostics (H recombination lines, IR luminosity or UV luminosity) are either difficult to measure, suffer large and uncertain extinction corrections, or

are contaminated by emission associated with black hole accretion.

Because some of the most intense stages of star-formation and supermassive blackhole (SMBH) accretion (i.e., AGN) occur in dust-obscured galaxies, many optical/near-IR diagnostics are not reliable. There is a need for a SFR indicator that can peer into these dust enshrouded galaxies and disentangle the amount of emission from ongoing star formation from that associated with SMBH accretion. Previous work has focused on the [O II] λ3727 Å emission line for quasars. The [O II] emission line should be an equally effective tracer of star-formation in the host galaxies of quasars as star-forming galaxies. But quasar spectra generally show little or no [O II] emission beyond that expected from the AGN (Ho, 2005).

Recent work suggests that the polycyclic aromatic hydrocarbon (PAH) emission, which emit strongly in the mid-IR ($3-19\mu$m), correlates with the total SFR in star-forming galaxies. For galaxies with AGN the PAH features have been shown to continue to trace the SFR from the integrated light of the galaxy for AGN that are not the dominant source of the integrated light (Shipley et al., 2013). Furthermore, the 11.3μm PAH feature even in the presence of an AGN is not significantly attenuated around the nuclei by a study looking at this effect for nuclear versus off nuclear regions in Seyfert galaxies (Diamond-Stanic & Rieke, 2010). Therefore, the integrated PAH emission from a galaxy offers a tracer of the SFR even in galaxies with AGN. We discuss the utility of using the PAH emission to study the SFR in galaxies over a large range of total IR luminosity and AGN activity (from starbursts to quasars) to determine as a function of AGN luminosity if or when this relation break down, which we plan for a future paper to study the co-evolution of star-formation and SMBH accretion (Shipley et al., in preparation).

The luminosity in the mid-IR PAH emission bands is very strong for galaxies with ongoing star-formation. The total PAH emission can contribute as much as 20% of

the total IR luminosity and the 7.7μm PAH band may contribute as much as 50% of the total PAH emission (e.g., Shipley et al., 2013; Smith et al., 2007; Wu et al., 2010). Certain PAH bands are made up of several dust emission features (e.g., 7.7μm, 8.6μm, 11.3μm, 12.7μm, and 17.0μm PAH bands) and so we will use the general term "feature" to describe the PAH emission bands. Because the PAH luminosities are so bright, these PAH features provide a well-calibrated SFR measurement for distant galaxies, and have the potential to provide accurate SFRs for deeply obscured galaxies and galaxies with AGN.

There have been previous attempts to calibrate the PAH emission as a SFR indicator. These either focus on high-luminosity objects and calibrate against the total IR luminosity, which contains an unknown contribution from AGN and/or optical depth effects (Pope et al., 2008; Lutz et al., 2008; Fu & Stockton, 2009). Other studies have focused on the broadband emission in the mid-IR which contains contributions both from the continuum and PAH emission (Calzetti et al., 2007; Fumagalli et al., 2014; Battisti et al., 2015). There is a need for a PAH SFR indicator calibrated over a range of bolometric luminosity using the luminosity in the PAH emission features themselves.

In this study we take advantage of these bright PAH emission features by using a sample of galaxies with *Spitzer*/IRS spectroscopy out to z $<$ 0.4. This is the first attempt to calibrate the PAH emission against robust SFR measures of the integrated light for distant galaxies over a large range of total IR luminosity (section 3.5). This is the calibration that is needed to interpret SFRs from *Spitzer* spectroscopy (and future *JWST* spectroscopy) of cosmological distant galaxies.

Specifically, we can apply PAH SFRs to archival studies of *Spitzer*/IRS spectroscopy that will be sensitive out to z $\lesssim$ 4. This will also be important for future observations using the Mid-Infrared Instrument (MIRI; 5-28μm) on board *JWST*.

It will be important to have calibrated SFR tracers from bright emission features in order to maximize the science efficiency with *JWST*. The PAH features, using *JWST*/MIRI, will allow us to probe galaxies in the mid-IR down to much lower luminosities ($L_{IR} \lesssim 10^{11}$ $L_{\odot}$) out to $z \lesssim 2.5$ with much greater sensitivity than any previous observations.

The outline for the rest of this paper is the following. In § 4.2, we define our calibration and application samples. In § 3.3, we describe our analysis of the derived quantities. In § 3.4, we present our SFR relations of the PAH luminosity. In § 3.5, we discuss previous calibrations of the PAH luminosity as a SFR indicator. In § 3.6, we demonstrate our PAH SFR relations on a high redshift lensed galaxy sample. In § 5, we present our conclusions. The ΛCDM cosmology we assume is $H_0 = 70$ km $s^{-1}Mpc^{-1}$, $\Omega_m = 0.3$, and $\Omega_\lambda = 0.7$ throughout this work (previous studies we reference throughout this work predominantly use this cosmology and we adopt it as well to be consistent as much as possible). We assume a "Kroupa" initial mass function (IMF) throughout this chapter. The "Kroupa" IMF has the slope $\alpha = 2.3$ for stellar masses $0.5 - 100$ $M_{\odot}$, and a shallower slope $\alpha = 1.3$ for the mass range $0.1 - 0.5$ $M_{\odot}$. The "Kroupa" IMF is more consistent with recent observations of the Galactic field IMF (e.g., Chabrier, 2003; Kroupa & Weidner, 2003).

3.2 Sample and Data

3.2.1 Calibration Samples

For proper calibration of the PAH features as a reliable SFR indicator, we carefully selected galaxies that had full coverage of the *Spitzer*/IRS spectrum with *Spitzer*/MIPS 24μm observations. We required the galaxies in our sample have complete optical coverage of the important emission lines needed (specifically Hβ, [O III] λ5007 Å, Hα and [N II] λ6583 Å) to measure dust-corrected SFRs from the

Hα emission line luminosity (Kennicutt et al., 2009), estimate ionization state (Kewley et al., 2001; Kauffmann et al., 2003) and the gas-phase metallicity (Pettini & Pagel, 2004). We also required that the galaxies be sufficiently distant that the *Spitzer*/IRS contains the majority of the integrated light in the slit. In effect, this limits us to $z > 0.01$ or where robust aperture corrections are available (see below).

We identified three literature galaxy samples that fulfill our selection criteria. We use these three samples as our **calibration sample** to perform our calibration and establish the PAH luminosity as a SFR indicator. The full calibration sample includes 286 galaxies and is built from O'Dowd et al. (2009), Shipley et al. (2013) and Brown et al. (2014) samples (specific steps taken for data reduction of the spectra can be found therein). Optical and IR aperture corrections were performed by both O'Dowd et al. (2009) and Brown et al. (2014) and can be found therein. For Shipley et al. (2013), IR aperture corrections were performed and can be found in the reference. Optical aperture corrections were on average $\sim$10% for the Shipley et al. (2013) sample. The calibration sample includes a broad range of galaxies allowing for a robust calibration of the PAH luminosity for vastly different systems. A few sources from Brown et al. (2014) are below our redshift requirement of z $>$ 0.01. We keep these galaxies in our primary and secondary calibration samples because Brown et al. (2014) achieved such accurate aperture corrections to construct their spectral energy distributions (SEDs), but this may introduce some bias as the aperture corrections may not be the same between the nuclear regions used for spectroscopy and the galaxy outskirts.

We excluded from our full calibration sample those objects with poor data quality, where measured line/feature fluxes are upper limits in one or more of the required emission features for Hα, the three brightest PAH features (6.2μm, 7.7μm and 11.3μm features) or the MIPS 24μm band. Various reasons exist for the need to exclude

galaxies from the full calibration sample: not all galaxies in Brown et al. (2014) have *Spitzer* IRS coverage; the sources in the *Spitzer* First Look Survey (FLS) from Shipley et al. (2013) do not have optical spectroscopy covering Hα. We discuss these reasons in detail in the following sections for each sample. This reduced our calibration sample to 227 galaxies.

Finally, we restricted our calibration sample to include only star-forming galaxies with no indications of AGN (which can contribute both to the Hα and 24μm emission) and we required all galaxies have approximately solar gas-phase metallicity (see § 3.3.4 below). These restrictions reduced our calibration sample to 105 galaxies fitting all the requirements. This constitutes our **primary calibration sample**. In what follows, we focus the PAH SFR calibration on this primary calibration sample of 105 galaxies, which span redshift $0.0 < z < 0.4$ and IR luminosity $10^9 < L_{IR}/L_{\odot} < 10^{12}$. We also consider a secondary calibration sample of 25 galaxies that satisfy all our selection criteria, but have sub-solar metallicity (see § 3.3.4 and § 3.4.3).

3.2.1.1 O'Dowd et al. (2009) Sample

The O'Dowd et al. (2009) sample consists of 92 galaxies that covers a range in total IR luminosity of $L_{IR} = 10^9 - 10^{11}$ $L_{\odot}$ that complements the lower luminosity galaxies in Brown et al. (2014) with a redshift of $0.03 < z < 0.22$ and varying AGN activity (from starbursts to AGN). Compared to the solar oxygen abundance, $12 + \log(O/H) = 8.69$ (Asplund et al., 2009), the galaxies in the O'Dowd et al. (2009) sample span a narrow range around solar ($12 + \log(O/H)_{N2} = 8.6$ to 8.8 with one galaxy at 9.0). This sample has complete coverage of the optical spectra (using the emission line fluxes from the SDSS DR7), IRS spectra and MIPS 24μm photometry taken from the published data. 63 galaxies from this sample fit our primary calibration sample criteria.

3.2.1.2 Shipley et al. (2013) Sample

The Shipley et al. (2013) sample consists of 65 galaxies covering a range in total IR luminosity of $L_{IR} = 10^{10} - 10^{12}$ $L_{\odot}$ with mostly higher IR luminosity compared to the Brown et al. (2014) and O'Dowd et al. (2009) samples. The sample has a redshift of $0.02 < z < 0.6$ of varying AGN activity (from starbursts to AGN). Compared to the solar oxygen abundance, $12 + \log(O/H) = 8.69$ (Asplund et al., 2009), the galaxies in the Shipley et al. (2013) sample span a range around solar ($12 + \log(O/H)_{N2} =$ 8.4 to 8.8) but have metallicities that bridge the other two samples in comparison. This sample has complete IR coverage of the IRS and MIPS 24μm photometry and complete optical spectroscopic data for 26 of the galaxies in the sample. 12 galaxies from this sample fit our primary calibration sample criteria. Two galaxies fit the secondary calibration sample criteria.

3.2.1.3 Brown et al. (2014) Sample

The Brown et al. (2014) study included 129 galaxies, covering a large range in total IR luminosity ($L_{IR} = 10^{9} - 10^{12}$ $L_{\odot}$) and diverse range in morphology (from dwarf irregulars to ellipticals) with a redshift of $0.0 < z < 0.06$ and varying AGN activity (from starburst to AGN). Because of the lower redshift and mostly lower IR luminosity range of the the Brown et al. (2014) sample, it contains lower metallicity galaxies ($7.8 < 12 + \log(O/H)_{N2} < 8.8$) compared to the O'Dowd et al. (2009) and Shipley et al. (2013) samples. The Brown et al. (2014) sample also includes clearly merging systems. This extends the study of the PAH emission as a SFR indicator over a range of activity and metallicity. This sample has complete optical spectra and MIPS 24μm photometry coverage from the given SEDs and includes IRS spectra for 111 of the galaxies in the sample (galaxies without IRS spectra are passive). We use these for our calibration sample. 30 galaxies from this sample fit our primary

calibration sample criteria. 23 galaxies fit the secondary calibration sample criteria.

Because the redshift distribution of the Brown et al. (2014) sample is lower, the aperture corrections for light lost outside the slit is higher. Brown et al. (2014) provided aperture corrections at 8μm and 12μm, and caution must be applied when these differ significantly. For the Brown et al. (2014) galaxies in our primary calibration sample, most (23/30 galaxies) have 8μm and 12μm aperture corrections consistent with the sample (the aperture corrections are $\sim$1.37 and $\sim$1.34 for 8μm and 12μm, respectively). The remaining seven galaxies have larger differences (the aperture corrections are $\sim$2.52 and $\sim$2.35 for 8μm and 12μm, respectively), but a visual inspection of the spectra show no obvious discontinuities and none of our results would change if we exclude these galaxies.

3.2.2 Application Sample of High Redshift Galaxies

To demonstrate an application of the PAH SFR calibration, we use *Spitzer*/IRS data for a sample of high-redshift ($1 < z < 3$) galaxies that have been gravitationally lensed by foreground massive galaxies and/or galaxy clusters. In many cases the gravitational lensing is substantial, boosting the flux from the background galaxies by factors of $\mu =\sim 3 - 30$. Because of the lensing factors the sensitivity is what can be expected for "typical" distant galaxies observed with *JWST*/MIRI. *JWST*/MIRI will be able to observe the 6.2μm and 7.7μm PAH features for galaxies with SFRs as low as $\sim$10 $M_\odot$ yr^{-1} to $z \lesssim 2.5$ by covering a wavelength range from 4.9μm to 28.8μm with greater sensitivity than any previous IR mission[1].

We use the sample and results reported in Rujopakarn et al. (2012), which include line flux measurements (or limits) for Paα or Brα and the PAH features. The Paα and Brα emission lines are "gold standard" SFR indicators as they trace the ionization

[1]see: http://ircamera.as.arizona.edu/MIRI/performance.htm

from the same star-forming populations as Hα, but Paα and Brα suffer substantially less extinction owing to longer wavelengths in the near-IR. In addition, we reprocess the *Spitzer*/IRS data for the 8 o'clock arc as Rujopakarn et al. (2012) did not report measurements for the PAH features in the mid-IR spectroscopy for this galaxy. We used their values for the redshift and lensing magnification for each galaxy (and references therein), including the 8 o'clock arc to be consistent for the sample[2]. We define these seven high-redshift lensed galaxies from Rujopakarn et al. (2012) as our **application sample**.

The *Spitzer*/IRS data in the application sample provide line fluxes for the Paα and Brα recombination lines, which are well-studied SFR indicators. We focus our comparison of the estimated PAH SFRs to the estimated Paα and Brα SFRs in our application of the PAH SFR calibration (see § 3.6). Depending on the redshift and *Spitzer*/IRS channels observed, only one of these SFR indicators was available for each galaxy. In general, Brα emission is available for the z < 2 galaxies and Paα is available for z > 2 galaxies due to the channels used for the *Spitzer*/IRS observations. The galaxy cB58 (Seitz et al., 1998; Teplitz et al., 2000, at z=2.729 and $\mu \sim 30$), however, had upper limit fluxes for both emission lines. The galaxies with measured Brα fluxes are A2218b (Rigby et al., 2008, at z=1.034 and $\mu = 6.1$) and A2667a (Rigby et al., 2008, at z=1.035 and $\mu = 17$). The galaxies with measured Paα fluxes are the Clone (Hainline et al., 2009; Lin et al., 2009, at z=2.003 and $\mu = 27 \pm 1$), A2218a (Rigby et al., 2008; Papovich et al., 2009; Finkelstein et al., 2011, at z=2.520 and $\mu = 22 \pm 2$), A1835a (Smail et al., 2005; Rigby et al., 2008, at z=2.566 and $\mu = 3.5 \pm 0.5$), and the 8 o'clock arc (Allam et al., 2007; Finkelstein et al., 2009b, at

[2]The approximate magnification of a lensed galaxy introduces a large uncertainty in the estimated SFR as the actual magnification may differ by a factor of a few to that of the measured. As a result, other studies may use a different magnification; which can cause the estimated SFRs to be over- or underestimated in comparison to ours.

z=2.731 and $\mu \sim 8$).

For the 8 o'clock arc, we reprocessed *Spitzer* data taken from program 40443 (PI: C. Papovich). We reduced the spectroscopic data for the 8 o'clock arc using the S17.2.0 version of the processing software from the basic calibrated data (BCD) for the IRS SL2 and LL1 modules by following the *Spitzer* Data Analysis Cookbook, Recipe 17[3]. As in Rujopakarn et al. (2012), we were able to de-blend the flux by performing PSF photometry to measure the flux of the arc. We reduced the IRAC and MIPS 24μm data using S16.1.0 version of the processing software from the BCD images by following the data reduction steps outlined in Papovich et al. (2009). We used three apertures of 1.8$''$ each centered on the three components identified by (Finkelstein et al., 2009b) using the *Spitzer* APEX source extraction software to extract the IRAC flux from the 5.8μm band. We estimate that the aperture corrections are 30$-$50% with the contamination from the nearby LIRG at the 30$-$50% level and the corrections cancel each other.[4]

To calibrate the absolute flux density of the IRS spectra for the 8 o'clock arc, we integrated the SL2 module with the IRAC 5.8μm transmission function and the LL1 module with the MIPS 24μm transmission function. We took the ratio of the observed flux density as measured directly from the IRAC and MIPS observations to the flux density synthesized from the IRS spectra as an aperture correction. We did this to account for contamination from the foreground luminous IR galaxy or light that is lost outside the spectroscopic slits from the 8 o'clock arc. Figure 3.1 shows the extracted, flux calibrated IRS SL2 and LL1 spectra for the 8 o'clock arc. We use this flux-corrected spectra to measure the Paα emission line from the IRS/SL2 spectrum and the PAH features from the IRS/LL1 spectrum. We extracted line fluxes from

[3]see: http://irsa.ipac.caltech.edu/data/SPITZER/docs/dataanalysistools/cookbook/23/
[4]see: http://irsa.ipac.caltech.edu/data/SPITZER/docs/irac/iracinstrumenthandbook/

the IRS data for the 8 o'clock arc and the galaxies in our calibration sample using the methods described in § 4.3.1.

3.3 Derived Quantities

3.3.1 IRS Spectral Fitting

To determine flux estimates for the PAH features in the IRS spectra of our calibration sample, we used the PAHFIT spectral decomposition code (Smith et al., 2007), designed for *Spitzer* IRS data. PAHFIT uses a χ^2 minimization routine to fit a non-negative combination of multiple emission features and continua to the one-dimensional spectra of our sources. The features included in PAHFIT are the dust emission features from PAHs (modeled as Drude profiles), thermal dust continuum, continuum from starlight, atomic and molecular emission lines (modeled as Gaussians), and dust extinction. The PAH emission features at (e.g. 7.7, 11.3, and 17 μm) are blends of multiple components, and PAHFIT treats these complexes as individual emission "features".

We take the published PAH fluxes from O'Dowd et al. (2009) and Shipley et al. (2013), which used the same PAHFIT input parameters as we use here for the Brown et al. (2014) sample (see references for specific parameters used). We fit the features in the IRS spectrum for each galaxy in Brown et al. (2014) that had an IRS spectrum (111/129 galaxies).

For the application sample, the published values for the *Spitzer*/IRS spectra were fit using PAHFIT with the same parameters as our calibration sample. We use these flux measurements of the Paα, Brα emission lines and PAH features to estimate the SFRs. We fit the 8 o'clock arc spectra with the same procedure. It was important to have the flux measurement fit the same way for each sample to have an accurate comparison between our PAH SFRs and the SFR indicators (Paα and Brα) available

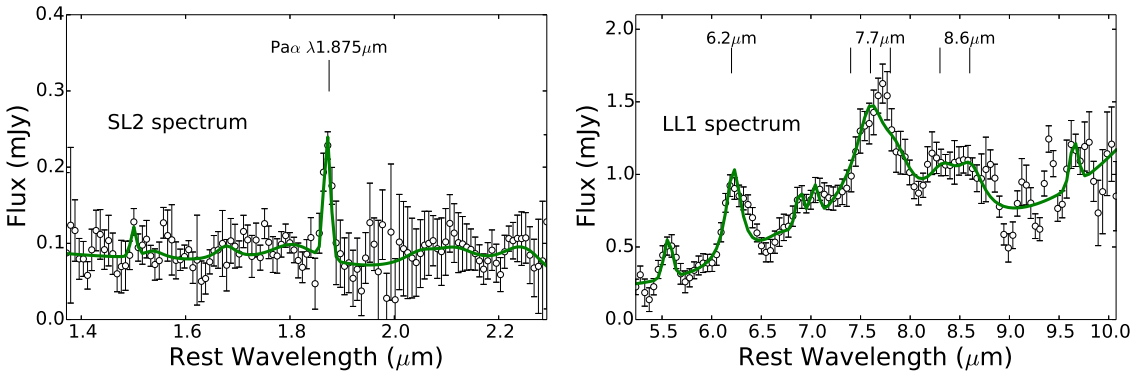

Figure 3.1 — In each panel, the open circles are the measured flux densities from the *Spitzer*/IRS data observations with error bars representing the uncertainties in those measurements and the green line represents the best fit from spectral decomposition of PAHFIT. The (Right) panel shows the *Spitzer*/IRS LL1 spectrum of the strongly gravitationally lensed galaxy, the "8 o'clock arc" (see § 3.2.2 and table 3.5). Because of the galaxy's high redshift, z=2.731, not all PAH features are accessible, but the 6.2μm SFR = 302 ± 20.0 $M_\odot$ yr^{-1} and the 7.7μm SFR = 262 ± 36.7 $M_\odot$ yr^{-1}. In contrast, the *Spitzer*/IRS SL2 spectrum (Left) panel gives a consistent SFR from Paα, SFR = 265 ± 29.6 $M_\odot$ yr^{-1}.

in Rujopakarn et al. (2012).

Our measured flux values for the 8 o'clock arc are $L_{Pa\alpha} = 7.4 \pm 0.8 \times 10^{-16}$ erg s^{-1} cm^{-2} and $L_{6.2\mu m} = 21.1 \pm 1.4 \times 10^{-15}$ erg s^{-1} cm^{-2}, $L_{7.7\mu m} = 80.0 \pm 11.2 \times 10^{-15}$ erg s^{-1} cm^{-2}. But as suggested in Rujopakarn et al. (2012), the resulting spectrum (for the LL1) has signal-to-noise (S/N) too low for PAHFIT to fit accurately the continuum and emission features due to the contamination of the nearby sources. We do see this to some extent as PAHFIT failed to converge and yield a more accurate fit to the PAH features in the *Spitzer*/IRS LL1 spectrum (figure 3.1).

3.3.2 Optical Spectral Fitting

For the O'Dowd et al. (2009) sample, we used optical line flux measurements (Hβ, [O III] λ5007 Å, Hα and [N II] λ6583 Å) from the updated line flux measurements

from SDSS DR7 (MPA/JHU value-added galaxy catalog, Tremonti et al., 2004). For Shipley et al. (2013), we used the line flux measurements from the AGN Galaxy Evolution Survey (AGES), reported in table 3.1. For Brown et al. (2014), we fit the emission lines as simple gaussians using a least squares routine to obtain the best fit. We fit the Hα and [N II] doublet simultaneously using three Gaussians, with the ratio of the central wavelengths fixed. Figure 3.2 shows representative spectra and our fits for a star-forming galaxy and AGN in the Brown et al. (2014) sample.

The relationship between the Hα/[N II] λ6583 Å and Hβ/[O III] λ5007 Å emission line ratios provides a test for ionization from a central AGN using an optical Baldwin, Phillips and Terlevich (BPT) classification (Kewley et al., 2001; Kauffmann et al., 2003). We adopted the SDSS DR7 measured emission line fluxes for the O'Dowd et al. (2009) sample. We note that a few of the galaxy classifications are changed to those in O'Dowd et al. (2009), that used the SDSS DR4 flux measurements. For the Shipley et al. (2013) sample, we used the measured fluxes in table 3.1 for classification. For the Brown et al. (2014) sample, we use their reported optical BPT classifications.

3.3.3 Dust-Corrected Hα Emission from Rest-Frame MIPS 24 μm Flux

We estimate dust-corrected Hα line luminosities using the sum of the observed Hα emission line and a fraction of the 24μm monochromatic luminosity as defined by Kennicutt et al. (2009),

$$\mathrm{L}_{\mathrm{H}\alpha}^{\mathrm{corr}}\ (\mathrm{erg\ s^{-1}}) = \mathrm{L}_{\mathrm{H}\alpha}^{\mathrm{obs}} + 0.020\ \mathrm{L}_{24\mu\mathrm{m}}\ (\mathrm{erg\ s^{-1}}) \tag{3.1}$$

For Brown et al. (2014) this was straightforward considering the given SEDs for their galaxies were given in the rest-frame. We used the 24μm filter from *Spitzer*/MIPS and integrated the rest-frame spectra over the filter to obtain the estimated 24μm

Table 3.1. Optical Fluxes and BPT Classification for Shipley et al. (2013) Sample

ID	Hβ (10^{-16})	[O III] λ5007 Å (10^{-16})	Hα (10^{-16})	[N II] λ6583 Å (10^{-16})	BPT Class
1	22.4 ± 0.33	41.8 ± 0.32	89.6 ± 0.44	16.0 ± 0.27	SF
2	...	...	...	...	...
3	0.99 ± 0.34	...	...	...	...
4	9.88 ± 0.30	1.22 ± 0.20	63.2 ± 0.37	21.9 ± 0.28	SF
5	60.5 ± 1.18	18.6 ± 1.00	414. ± 2.29	155. ± 1.79	SF
6	1.70 ± 0.30	1.49 ± 0.32	11.9 ± 0.51	7.40 ± 0.47	SF/AGN
7	51.7 ± 0.43	10.7 ± 0.33	258. ± 1.56	98.9 ± 0.62	SF
8	1.83 ± 0.30	1.78 ± 0.26	13.8 ± 0.39	13.8 ± 0.35	AGN
9	0.56 ± 0.12	0.49 ± 0.10	4.32 ± 0.20	3.32 ± 0.19	SF/AGN
10	2.92 ± 0.24	2.38 ± 0.22	22.4 ± 0.51	12.7 ± 0.50	SF/AGN
11	0.36 ± 0.09	0.24 ± 0.12	1.32 ± 0.24	...	...
12	6.93 ± 0.26	7.52 ± 0.28	40.9 ± 0.75	17.0 ± 0.64	SF/AGN
13	...	...	...	...	...
14	0.82 ± 0.28	...	4.33 ± 0.76	2.64 ± 0.49	...
15	10.0 ± 0.26	5.75 ± 0.25	65.6 ± 1.00	29.4 ± 0.77	SF
16	...	1.36 ± 0.27	...	...	...
17	4.52 ± 0.17	3.37 ± 0.16	38.0 ± 0.50	17.5 ± 0.39	SF/AGN
18	21.7 ± 0.35	12.4 ± 0.34	120. ± 0.72	42.6 ± 0.59	SF
19	2.14 ± 0.13	3.42 ± 0.09	11.0 ± 0.36	2.57 ± 0.27	SF
20	2.42 ± 0.20	0.69 ± 0.18	14.4 ± 0.41	7.04 ± 0.44	SF
21	1.51 ± 0.24	8.42 ± 0.25	7.22 ± 0.62	5.65 ± 0.60	AGN
22	7.71 ± 0.35	13.9 ± 0.37	39.3 ± 1.65	25.4 ± 1.16	SF/AGN
23	10.4 ± 0.75	4.74 ± 0.65	75.6 ± 2.34	30.5 ± 2.04	SF
24	0.94 ± 0.26	12.3 ± 0.24	...	...	...
25	5.66 ± 0.38	4.95 ± 0.40	28.1 ± 1.10	18.1 ± 1.19	SF/AGN
26	...	4.77 ± 0.42	...	...	...
27	1.46 ± 0.25	4.45 ± 0.27	7.11 ± 1.15	6.72 ± 0.95	AGN
28	3.43 ± 0.13	1.66 ± 0.15	22.5 ± 0.82	6.31 ± 0.71	SF
29	2.01 ± 0.28	5.83 ± 0.31	...	...	...
30	2.42 ± 0.24	2.01 ± 0.18	...	...	...
31	4.92 ± 0.21	1.83 ± 0.16	...	...	...
32	1.76 ± 0.10	0.58 ± 0.10	...	...	...
33	1.21 ± 0.29	...	7.17 ± 0.64	2.78 ± 0.44	...
34	1.81 ± 0.14	0.92 ± 0.11	...	...	...
35	2.00 ± 0.47	...	...	...	...
36	1.01 ± 0.16	...	...	...	...
37	0.47 ± 0.08	1.53 ± 0.09	2.97 ± 0.29	1.67 ± 0.19	AGN
38	...	0.81 ± 0.13	...	...	...
39	...	...	...	...	...
40	0.51 ± 0.14	...	6.08 ± 0.62	5.79 ± 0.54	...
41	...	0.71 ± 0.20	3.08 ± 0.33	5.53 ± 0.36	...
42	1.16 ± 0.19	1.27 ± 0.21	10.3 ± 0.81	9.67 ± 0.73	AGN
43	...	...	...	...	...
44	1.58 ± 0.27	9.40 ± 0.34	...	...	...
45	1.22 ± 0.22	2.93 ± 0.26	...	...	...
46	2.75 ± 0.26	3.15 ± 0.20	12.1 ± 0.32	2.55 ± 0.21	SF
47	7.01 ± 0.29	3.68 ± 0.22	40.5 ± 0.51	14.9 ± 0.55	SF
48	5.45 ± 0.17	1.62 ± 0.19	59.2 ± 2.79	26.0 ± 2.99	SF
49	4.16 ± 0.71	18.0 ± 1.29	20.9 ± 4.05	13.4 ± 4.39	AGN
50	...	...	...	...	...

Note. — Column 1 is the galaxy identification defined in Shipley et al. (2013). Columns 2−5 are the measured fluxes for the emission lines Hβ, [O III] λ5007 Å, Hα and [N II] λ6583 Å, respectively (in units of erg s^{-1} cm^{-2}). Column 6 is the BPT classification from the measured fluxes.

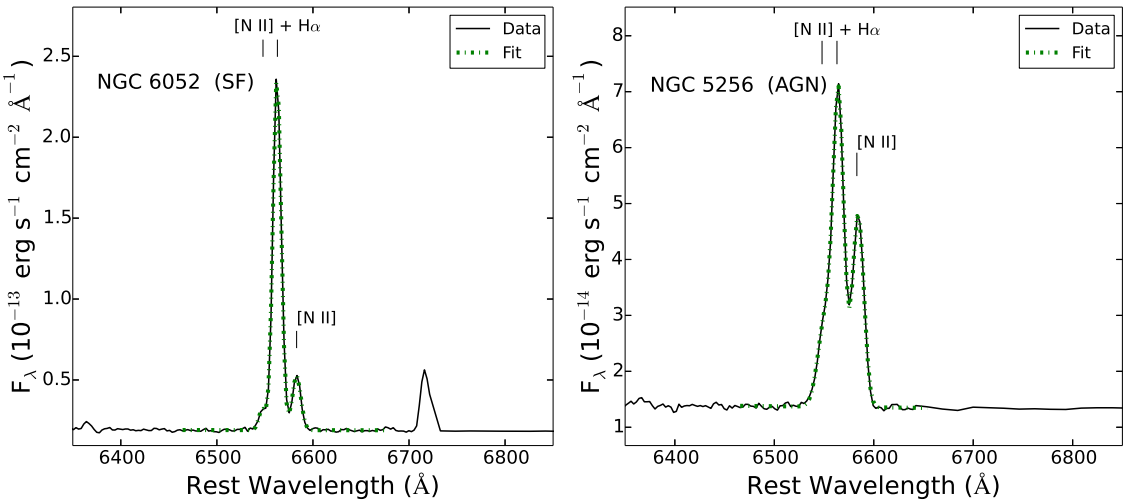

Figure 3.2 — Examples of our fits (green dot-dashed line) to the optical spectra (solid black line) for Brown et al. (2014) for the Hα and [N II] emission lines (see § 3.3.2 for fitting procedure). Here, we show NGC 6052 (star-forming) and NGC 5256 (AGN) that is representative of the entire Brown et al. (2014) sample for each classification (see § 3.3.2 for classification).

flux.

For O'Dowd et al. (2009) and Shipley et al. (2013) we used the best fit SEDs (see § 3.3.5) in the rest-frame for each galaxy and again integrated over the MIPS 24μm transmission function to obtain the estimated 24μm flux for each galaxy. This was necessary for these two samples to be consistent with each other as a significant amount of the galaxies' IRS spectra at rest-frame 24μm are shifted out of the IRS spectrum or dominated by noise due to the redshift of the galaxies (49/142 galaxies for the combined samples). Using the best fit SEDs gave us a reasonable representation of each galaxy's rest-frame 24μm flux.

We determined this by comparing the rest-frame 24μm flux from the best fit SED to that of the spectrum using only galaxies with $z < 0.15$ ($z \geq 0.15$ shifted the rest-frame 24μm flux into the noise dominated part of the IRS spectrum). This redshift

cut selected 93/142 galaxies from the combined samples of O'Dowd et al. (2009) and Shipley et al. (2013). We found that for 92/93 galaxies there was less than a 15% difference in the measured 24μm flux. If only the star-forming galaxies (61 galaxies) are considered there was less than an 11% difference in the measured 24μm flux. We feel confident that the differences are small enough for the primary and secondary calibration samples that any difference is represented in the uncertainty of the PAH SFR relations (see § 3.4.2).

In most cases the Hα dust corrections are substantial. Figure 3.3 shows the relation between the dust-corrected Hα luminosity and the ratio of observed Hα luminosity (uncorrected for dust extinction) to the dust-corrected Hα luminosity. Most of the galaxies in our primary and a few in the secondary calibration samples have dust corrections of more than a factor of 2 to the Hα luminosity. The median correction factor is 4.2 and the interquartile range (25−75 percentiles) is 2.5 − 5.9.

3.3.4 Gas-Phase Metallicities

The PAH emission from a galaxy is known to depend on the gas-phase metallicity. Engelbracht et al. (2005) demonstrated this dependence using 8μm-to-24μm ratios of galaxies above and below a metallicity of $12 + \log(\mathrm{O/H}) = 8.2$, where they attributed the smaller ratios for galaxies with low metallicity to a decrease in the mid-IR emission bands (attributed to PAHs). Calzetti et al. (2007) showed star-forming galaxies with low metallicities have less than expected mid-IR dust emission (presumably from PAH emission) based on a linear fit to their calibration of extinction corrected Pα to the 8μm dust emission. This trend is not seen in their calibration of extinction corrected Paα to Hα + 24μm luminosities, illustrating the PAH emission dependence on metallicity.

We calibrate the relation between metallicity, PAH emission, and SFRs using the

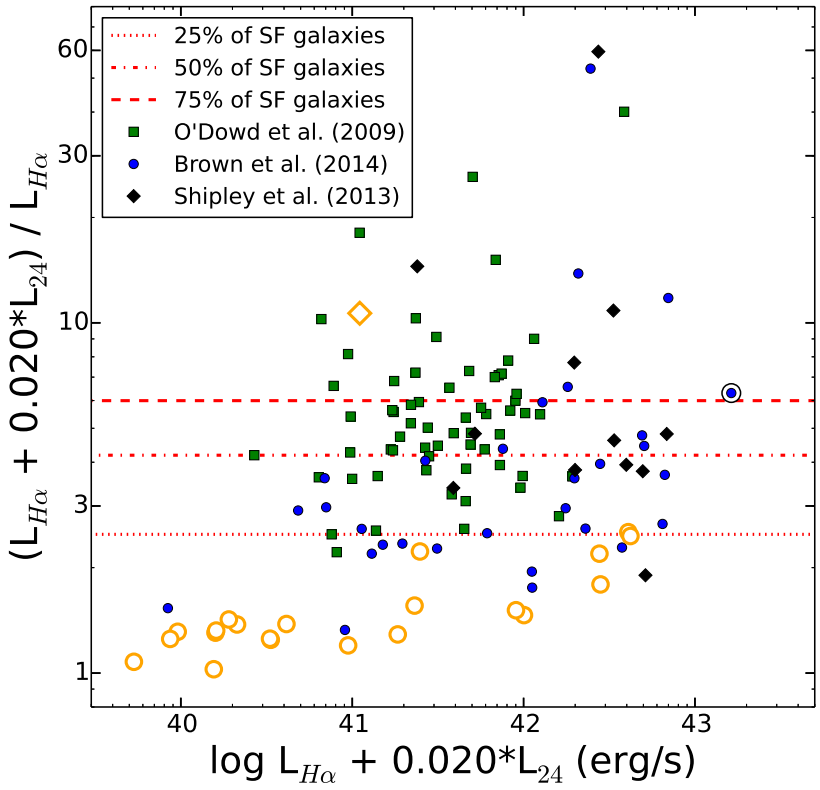

Figure 3.3 — The relation between the dust-corrected Hα luminosity and the dust correction factor, defined as the ratio of the dust-corrected Hα to observed (uncorrected) Hα. The horizontal lines show the 25, 50, and 75 percentiles of the distribution. The median correction factor is 4.2 and the interquartile range (25−75 percentiles) is 2.5 − 5.9. The orange symbols are low metallicity galaxies as defined in § 3.3.4. The blue point enclosed by a black circle denotes II Zw 096, see § 3.4.4.

data in our samples. For all galaxies in the calibration sample, we estimate the gas-phase oxygen abundance using the $N2$ index, $N2 \equiv \log$ [N II] λ6583 Å/Hα, using the relation from Pettini & Pagel (2004),

$$12 + \log(\mathrm{O/H}) = 8.90 + 0.57 \times N2 \tag{3.2}$$

We use $12 + \log(\mathrm{O/H})_{N2}$ because the $N2$ index is available for all galaxies in our calibration sample. Figure 3.4 shows the distribution of oxygen abundance for the galaxies in our primary and secondary calibration samples. Most sources fall in a tight distribution ($\pm$0.2 dex) around the solar abundance ($12 + \log(\mathrm{O/H}) = 8.69$, Asplund et al., 2009) with a long tail to lower abundances. This is unsurprising because of the well-known mass-metallicity relation (Tremonti et al. 2004). Most sources in the calibration samples have $L_{\mathrm{IR}} > 10^{10}$ $\mathrm{L}_{\odot}$, and likely have higher stellar mass, and therefore higher abundance (e.g., based on Tremonti et al., 2004, galaxies with stellar mass $> 10^9$ $\mathrm{M}_{\odot}$ have > 0.5 $\mathrm{Z}_{\odot}$). We use star-forming galaxies with $12 + \log(\mathrm{O/H})_{N2} \geq 8.5$ for the primary calibration sample.

3.3.5 Total Infrared Luminosity

We estimate the total IR luminosity ($\mathrm{L_{IR}} = \mathrm{L}_{8-1000\mu\mathrm{m}}$) using the MIPS 24$\mu$m flux densities (70$\mu$m and 160$\mu$m, where available in Shipley et al., 2013) using the method in Shipley et al. (2013). We use the Rieke et al. (2009) IR SEDs because for star-forming galaxies the total IR luminosities derived from these templates using the 24μm flux density only are closest to the IR luminosities derived when more IR photometric bands are available. We use this to understand the range of total IR luminosity over which our PAH SFRs are calibrated. We were able to determine the contributing total IR luminosity range for the Brown et al. (2014) sample by using the values reported in Haan et al. (2013) for the majority of the galaxies.

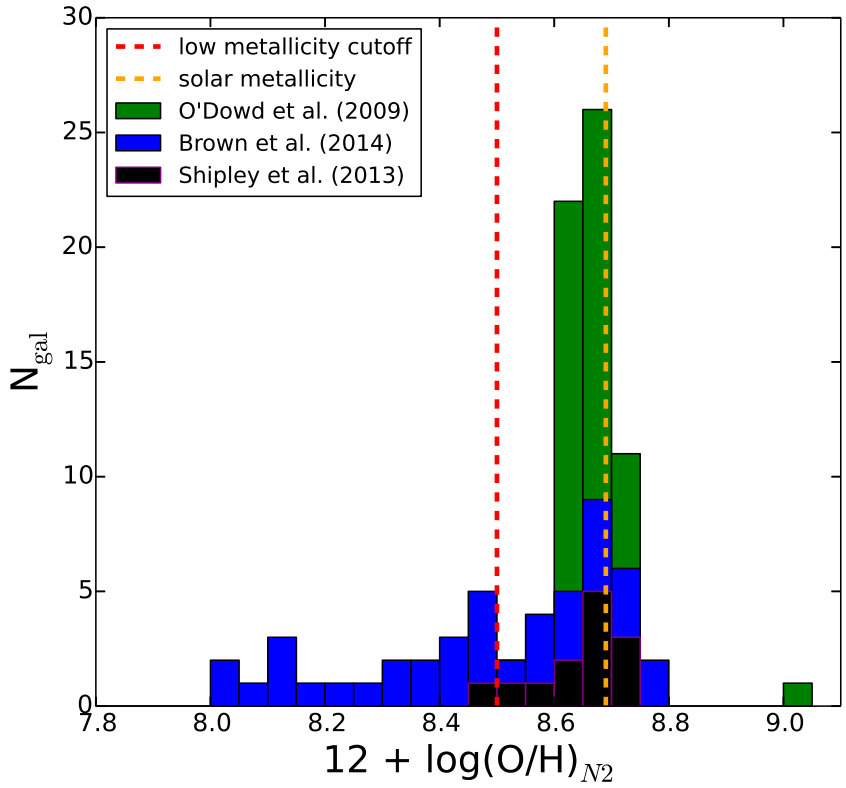

Figure 3.4 — Histogram of the metallicities for all the star-forming galaxies in the calibration sample, where the metallicities are 12 + log(O/H)$_{N2}$. For the calibration of the SFR relations using PAH luminosity we used galaxies with 12 + log(O/H)$_{N2}$ $\geq$ 8.5 (red dashed line) for our primary calibration sample. The resulting cut being $\sim$0.65 the solar abundance (12 + log(O/H) = 8.69, Asplund et al., 2009, orange dashed line).

3.4 The PAH SFR Calibration

Previous studies have showed that the Hα luminosity is a robust indicator of the SFR once corrected for dust extinction (e.g., Kennicutt, 1998). More recent work has shown that the Hα luminosity summed with a fraction of the monochromatic 24μm light provides a linear fit against extinction corrected Hα and Paα emission (Calzetti et al., 2007; Kennicutt et al., 2007, 2009; Treyer et al., 2010). Here we use the dust-corrected Hα from the 24μm monochromatic emission as our SFR calibrator, using Kennicutt et al. (2009),

$$\text{SFR } (\text{M}_\odot \text{ yr}^{-1}) = 5.5 \times 10^{-42}[\text{L}(\text{H}\alpha) + 0.020 \text{ L}(24\mu\text{m})] \text{ (erg s}^{-1}) \qquad (3.3)$$

We assume a "Kroupa" initial mass function (IMF) for our SFR calibration. The "Kroupa" IMF has the slope $\alpha = 2.3$ for stellar masses $0.5 - 100$ M$_\odot$, and a shallower slope $\alpha = 1.3$ for the mass range $0.1 - 0.5$ M$_\odot$.

3.4.1 PAH SFR Relations

We compare the relation between the luminosity in the PAH features to the dust-corrected Hα luminosity. Because different PAH features are accessible at different wavelengths depending on the redshift of the source and wavelength capabilities of the telescope/instrument, we calibrate both the individual lines at 6.2μm, 7.7μm and 11.3μm, as well as sums of these lines. It is also worth noting that Hα probes very young star-formation from OB stars, whereas it is likely that the PAH features cover a broader range of ages (presumably from A and F stars) and that different SFR indicators are sensitive to slightly different effects from the star-formation measured.

Figure 3.5 shows the correlation between the the total PAH luminosity (L_{PAH}=

$L_{6.2\mu m}$ + $L_{7.7\mu m}$ + $L_{11.3\mu m}$)[5] and the dust-corrected Hα luminosity for the 227 galaxies in our calibration sample. For star-forming galaxies with high metallicity, the total PAH luminosity correlates linearly with the dust-corrected Hα luminosity. Using the primary calibration sample, we find a linear fit of $L_{PAH} = 10^{1.30\pm0.055}\times[L_{H\alpha}$ + 0.020 $L_{24\mu m}]^{1.00\pm0.03}$. The scatter about this relation is very small, <0.15 dex. This implies that the total PAH emission correlates linearly with the SFR. The scatter is the same as that measured for the dust-corrected Hα (Kennicutt, 1998) and Paα (Calzetti et al., 2007) relations, which implies that as a SFR indicator the PAH luminosity has intrinsic scatter as small as dust-corrected Hα and Paα and may be as accurate as SFRs from Hydrogen recombination lines.

It is clear from Figure 3.5 (orange points) that there is a need to remove the low metallicity (and low S/N; S/N < 5) galaxies from our primary calibration sample. As the low metallicity (and low S/N) galaxies have low L_{PAH}/L_{fit} ratios (figure 3.5, bottom), where L_{fit} is defined as the unity relation fit to the primary calibration sample for the expected luminosity of the PAH luminosity for a given $L_{H\alpha}$ + 0.020×$L_{24\mu m}$ luminosity. We mark the galaxy II Zw 096 as it is an outlier (see § 3.4.4) in the figures (figures 3.5, 3.6 and 3.8) but do not omit it as it does not significantly affect our calibration of the PAH features (we discuss this interesting galaxy in § 3.4.4).

Our derived relations between the dust-corrected Hα luminosity and the total PAH luminosity are

$$\log L_{PAH} = (1.30 \pm 0.03) + \log(L_{H\alpha} + 0.020\times L_{24\mu m}) \quad (3.4)$$

[5] L_{PAH} we use to denote the PAH luminosity for the total luminosity of the 6.2μm, 7.7μm and 11.3μm features. All other instances of PAH luminosity will be denoted by the included PAH features (e.g. $L_{6.2\mu m}$). However in figures, we label explicitly which features are used.

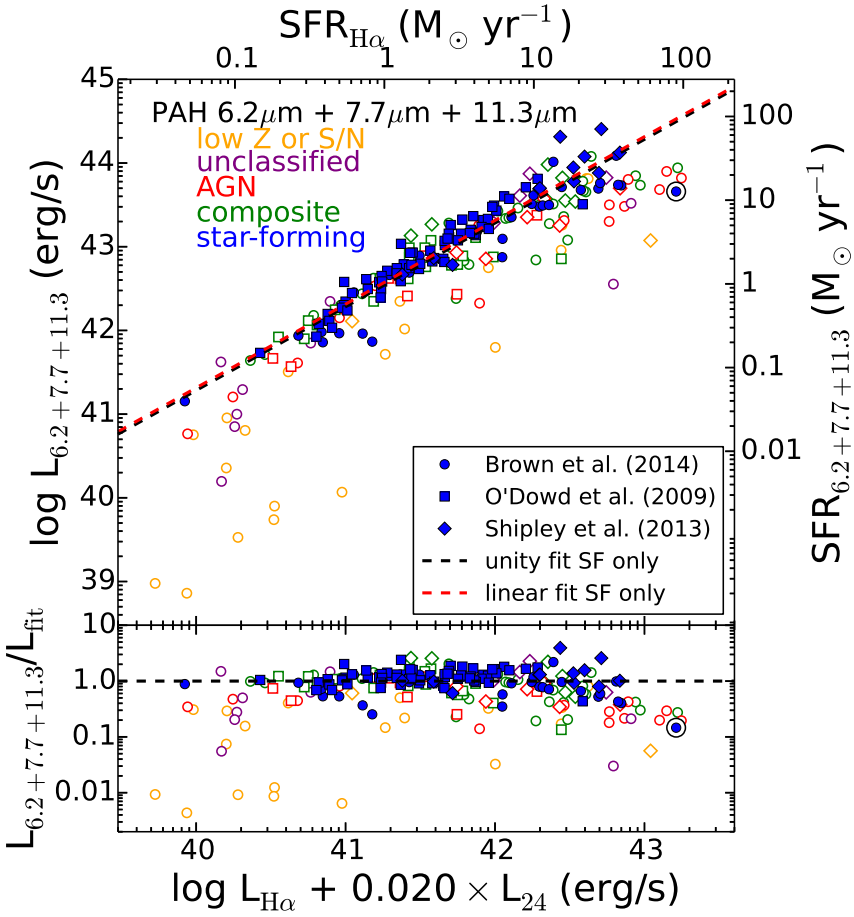

Figure 3.5 — The dust corrected Hα luminosity ($L_{H\alpha}$ + 0.020×$L_{24\mu m}$, Kennicutt et al., 2009) versus the total PAH luminosity ($L_{6.2\mu m}$ + $L_{7.7\mu m}$ + $L_{11.3\mu m}$ PAH features, top panel). We fit a unity relation to the primary calibration sample (solid black line) and use this line as L_{fit} to show the ratio of the total PAH luminosity to the unity relationship as a function of dust-corrected Hα luminosity (bottom panel). We classify galaxies as star-forming (blue points), composite (green points) or an AGN (red points) based on the location of their emission line ratios on a BPT diagram. Unclassified galaxies (purple points) did not have all lines required for BPT classification and galaxies with low metallicity or S/N (orange points) we exclude for the fit (see text for more detail). The blue point enclosed by a black circle denotes II Zw 096, see § 3.4.4.

for the unity relation and

$$\log L_{PAH} = (1.30 \pm 0.03) + (1.00 \pm 0.03) \log(L_{H\alpha} + 0.020 \times L_{24\mu m}) \quad (3.5)$$

for the linear relation. Using equation 3.3, this yields the following calibrations for the total PAH luminosity as a SFR indicator,

$$\log \text{SFR } (M_\odot \text{ yr}^{-1}) = (-42.56 \pm 0.03) + \log L_{PAH} \text{ (erg s}^{-1}) \quad (3.6)$$

and using the linear fit we find,

$$\log \text{SFR } (M_\odot \text{ yr}^{-1}) = (-42.56 \pm 0.03) + (1.00 \pm 0.03) \log L_{PAH} \text{ (erg s}^{-1}) \quad (3.7)$$

Showing there is statistical uncertainty of ≈0.03 dex and scatter of ≈0.135 dex on the total PAH luminosity unity SFR relationship.

We observe small offsets from the dust-corrected $L_{H\alpha}$ and L_{PAH} calibration between the different calibration samples. Comparing the differences in the samples, we measure average offsets of L_{PAH}/L_{fit} = 0.06, 0.06, -0.10 for the O'Dowd et al. (2009), Shipley et al. (2013) and Brown et al. (2014) samples, respectively. This may imply there is an additional systematic uncertainty of 0.1 dex (i.e., 20%) on the PAH SFR calibration from differences in aperture corrections or data processing and analysis.

We also calibrate the luminosity from the individual PAH features and combinations of them as SFR indicators as in some cases only one or two PAH features may be useable to get a SFR, such as high redshift galaxies (see § 3.6). Figure 3.6 shows the relations between the dust-corrected Hα luminosity and the individual PAH features and the total PAH luminosity for the primary calibration sample.

Figure 3.7 shows the distribution of residuals between the PAH luminosity and the fit, and shows both the scatter computed from the median absolute deviation (MAD, Beers et al., 1990) and a Gaussian fit, both of which are consistent. The scatter is smallest, $\sigma_{\rm MAD} = 0.14$ dex (i.e., 40%) whenever the 7.7μm feature is involved in the fit. This implies this feature may provide the most robust measure of the SFR. The relation against the 6.2μm feature has the highest scatter, $\sigma_{\rm MAD} = 0.21$ dex (i.e., 60%), which may indicate more variation in galaxies between the luminosity in this feature and the SFR.

Our derived relations between the dust-corrected Hα luminosity and the individual PAH luminosities are

$$\begin{aligned}
\log \mathrm{L}_{6.2\mu\mathrm{m}} &= (0.47 \pm 0.08) + \log(\mathrm{L}_{\mathrm{H}\alpha} + 0.020{\times}\mathrm{L}_{24\mu\mathrm{m}}) \\
\log \mathrm{L}_{7.7\mu\mathrm{m}} &= (1.11 \pm 0.05) + \log(\mathrm{L}_{\mathrm{H}\alpha} + 0.020{\times}\mathrm{L}_{24\mu\mathrm{m}}) \\
\log \mathrm{L}_{11.3\mu\mathrm{m}} &= (0.54 \pm 0.07) + \log(\mathrm{L}_{\mathrm{H}\alpha} + 0.020{\times}\mathrm{L}_{24\mu\mathrm{m}})
\end{aligned} \tag{3.8}$$

for the unity relations and the linear relations are

$$\begin{aligned}
\log \mathrm{L}_{6.2\mu\mathrm{m}} &= (-1.20 \pm 0.09) + (1.04 \pm 0.04)\ \log(\mathrm{L}_{\mathrm{H}\alpha} + 0.020{\times}\mathrm{L}_{24\mu\mathrm{m}}) \\
\log \mathrm{L}_{7.7\mu\mathrm{m}} &= (1.12 \pm 0.06) + (1.00 \pm 0.03)\ \log(\mathrm{L}_{\mathrm{H}\alpha} + 0.020{\times}\mathrm{L}_{24\mu\mathrm{m}}) \\
\log \mathrm{L}_{11.3\mu\mathrm{m}} &= (2.87 \pm 0.08) + (0.94 \pm 0.03)\ \log(\mathrm{L}_{\mathrm{H}\alpha} + 0.020{\times}\mathrm{L}_{24\mu\mathrm{m}})
\end{aligned} \tag{3.9}$$

In every instance, the linear relations are consistent with a unity slope between the PAH luminosities and the SFR. Again, using the relation from Kennicutt et al. (2009) given in equation 3.3, this yields the following calibrations for the individual PAH

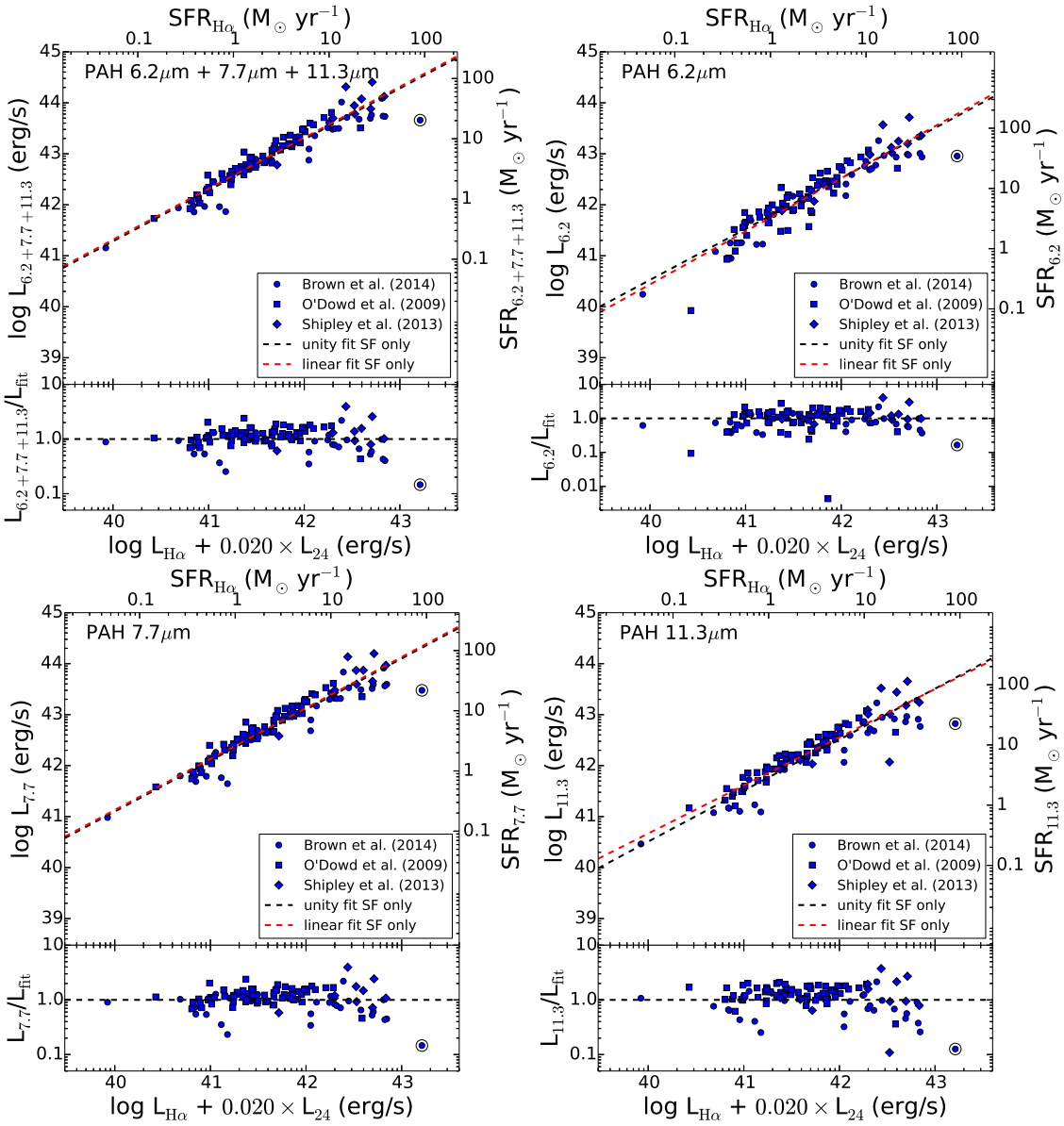

Figure 3.6 — The dust corrected Hα luminosity ($L_{H\alpha}$ + 0.020×$L_{24\mu m}$, Kennicutt et al., 2009) versus L_{PAH} (top left) and for the 6.2μm (top right), 7.7μm (bottom left) and 11.3μm (bottom right) PAH features separately. This illustrates that the small scatter persists for the individual PAH features ($\sigma_{MAD} \lesssim 0.2$ dex). We fit a unity relation to the primary calibration sample (solid black line) and use this line as L_{fit} to determine residuals of expected L_{PAH} values (bottom for each panel). We used this fit to determine a SFR relation for L_{PAH} and each PAH feature shown individually (see § 3.4.1). The blue point enclosed by a black circle denotes II Zw 096, see § 3.4.4.

Table 3.2. Unity PAH Luminosity SFR Relations

PAH Feature(s)	C	$\sigma_{\rm MAD}$
6.2 + 7.7 + 11.3	-42.56 ± 0.03	0.135
6.2	-41.73 ± 0.08	0.214
7.7	-42.37 ± 0.05	0.131
11.3	-41.80 ± 0.07	0.187
6.2 + 7.7	-42.47 ± 0.04	0.135
6.2 + 11.3	-42.09 ± 0.04	0.160
7.7 + 11.3	-42.48 ± 0.04	0.120

Note. — The calibration sample consisted of 105 galaxies used to determine the PAH SFR relations (see § 3.2.1). Column 1 defines which PAH features were used in the SFR relation. Column 2 gives the values for the unity SFR relations (defined as log SFR [$M_\odot$ yr^{-1}] = C + log $L_{PAH,\lambda}$ [erg s^{-1}]). Column 3 is the 1σ scatter in the SFR relation for the galaxies used in the fit (using the median absolute deviation, MAD ($\sigma_{\rm MAD}$) to represent the scatter).

luminosities as SFR indicators,

$$\begin{aligned}
\log \text{SFR } (M_\odot \text{ yr}^{-1}) &= (-41.73 \pm 0.08) + \log L_{6.2\mu\text{m}} \text{ (erg s}^{-1}) \\
\log \text{SFR } (M_\odot \text{ yr}^{-1}) &= (-42.37 \pm 0.05) + \log L_{7.7\mu\text{m}} \text{ (erg s}^{-1}) \\
\log \text{SFR } (M_\odot \text{ yr}^{-1}) &= (-41.80 \pm 0.07) + \log L_{11.3\mu\text{m}} \text{ (erg s}^{-1})
\end{aligned} \tag{3.10}$$

and using the linear fits we find,

$$\begin{aligned}
\log \text{SFR } (M_\odot \text{ yr}^{-1}) &= (-40.06 \pm 0.09) + (0.96 \pm 0.04) \log L_{6.2\mu\text{m}} \text{ (erg s}^{-1}) \\
\log \text{SFR } (M_\odot \text{ yr}^{-1}) &= (-42.38 \pm 0.06) + (1.00 \pm 0.03) \log L_{7.7\mu\text{m}} \text{ (erg s}^{-1}) \\
\log \text{SFR } (M_\odot \text{ yr}^{-1}) &= (-44.14 \pm 0.08) + (1.06 \pm 0.03) \log L_{11.3\mu\text{m}} \text{ (erg s}^{-1})
\end{aligned} \tag{3.11}$$

All of these SFR relations coefficients as well as the scatter for each can be found

Table 3.3. Linear PAH Luminosity SFR Relations

PAH Feature(s)	A	B	σ_{AB}	σ_{MAD}
6.2 + 7.7 + 11.3	-42.56 ± 0.03	1.00 ± 0.03	-0.03	0.138
6.2	-40.06 ± 0.09	0.96 ± 0.04	-0.07	0.233
7.7	-42.38 ± 0.06	1.00 ± 0.03	-0.03	0.138
11.3	-44.14 ± 0.08	1.06 ± 0.03	-0.04	0.166
6.2 + 7.7	-42.05 ± 0.04	0.99 ± 0.03	-0.03	0.137
6.2 + 11.3	-42.52 ± 0.05	1.01 ± 0.03	-0.04	0.144
7.7 + 11.3	-42.85 ± 0.04	1.01 ± 0.03	-0.03	0.139

Note. — The calibration sample consisted of 105 galaxies used to determine the PAH SFR relations (see § 3.2.1). Column 1 defines which PAH features were used in the SFR relation. Columns 2 and 3 give the values for the linear SFR relations (defined as log SFR [$M_\odot$ yr^{-1}] = A + B log $L_{PAH,\lambda}$ [erg s^{-1}]). Column 4 is the 1σ measurement in the covariance of the linear fit (see § 3.4.2). Column 5 is the 1σ scatter in the SFR relation for the galaxies used in the fit (using the median absolute deviation, MAD (σ_{MAD}) to represent the scatter).

in table 3.2 (unity relation defined as log SFR ($M_\odot$ yr^{-1}) = C + log $L_{PAH,\lambda}$ (erg s^{-1})) and table 3.3 (linear relation defined as log SFR ($M_\odot$ yr^{-1}) = A + B log $L_{PAH,\lambda}$ (erg s^{-1})), which includes all possible PAH feature combinations. We note there are two galaxies (galaxies SSGSS 52 and 83 from the sample of O'Dowd et al., 2009) for the 6.2μm calibration that are well off the relation. We attribute this to the "problematic 6.2μm feature fits" discussed in O'Dowd et al. (2009). These galaxies did not affect our calibration of the 6.2μm feature, and the uncertainties decrease only slightly when excluding them from the PAH SFR relations.

3.4.2 Uncertainties for Derived SFR Relations

We determined uncertainties for our PAH SFR relations using a robust linear fit to the 105 galaxies in the primary calibration sample that utilizes a least squares fitting routine. This routine determines residuals for the fit of the luminosities and

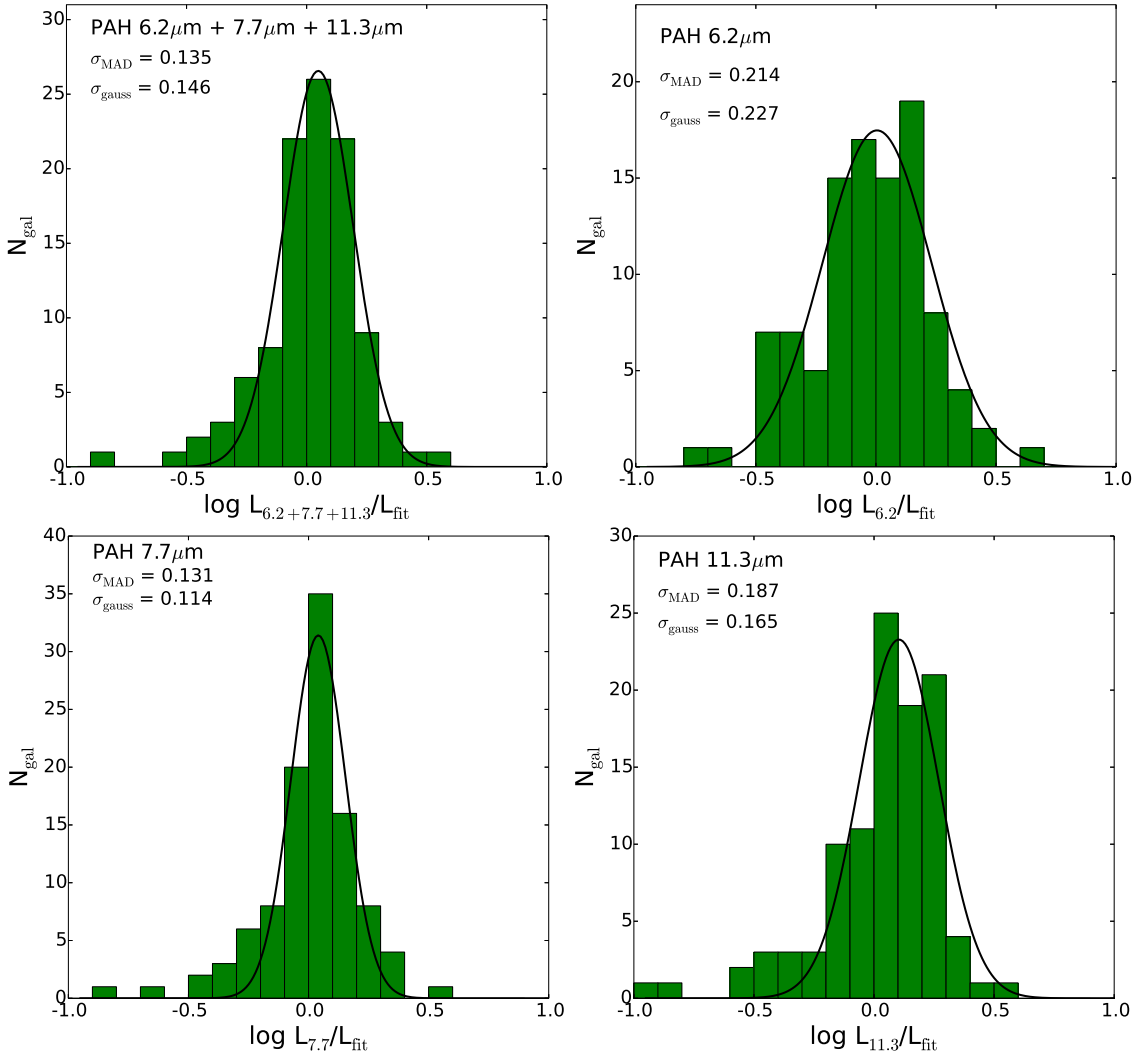

Figure 3.7 — A histogram of the ratio of L_{PAH}/L_{fit}, where L_{fit} is the unity relation to the star-forming galaxies shown in figure 3.6, demonstrating the scatter in the sample and consistency of L_{PAH} as a SFR indicator in comparison to dust-corrected Hα for the 6.2μm (top right), 7.7μm (bottom left), 11.3μm (bottom right) PAH features individually and L_{PAH} (top left). The bin size used is 0.1 log L_{PAH}/L_{fit} and N_{gal} represents the number of galaxies in each bin. We fit a gaussian distribution to determine the standard deviation of the scatter (σ_{gauss}, shown in plot) and calculated the median absolute deviation (σ_{MAD}, shown in plot) detailed in Beers et al. (1990) to accurately represent the uncertainty of $L_{PAH,\lambda}$ as a SFR indicator.

estimates a 1σ uncertainty on the mean of the estimated values returned for the fit (slope and intercept for the linear fits). We then propagate these uncertainties for the derived PAH SFR relations. As the slope and intercept are dependent on each other for the linear SFR relations, we calculate this dependence on the 1σ uncertainties from the covariance matrix for these fits (see equation 3.12) and are reported in table 3.3.

$$cov = \begin{pmatrix} \sigma_{\rm A}^2 & \sigma_{\rm AB} \\ \sigma_{\rm AB} & \sigma_{\rm B}^2 \end{pmatrix} \tag{3.12}$$

The fact that the off diagonal elements of the covariance matrix are < 0 means that A and B are not independent and are anti-correlated. The diagonal elements are the variance on the parameters (i.e., $\sigma_{\rm A}$ is the uncertainty on the intercept and $\sigma_{\rm B}$ is the uncertainty on the slope).

3.4.3 Correction to PAH Luminosity for Low Metallicity Galaxies

For our secondary calibration sample of 25 galaxies, we limited the oxygen abundance of the galaxies to $12 + \log({\rm O/H})_{N2} \leq 8.55$ as shown in figure 3.8. Figure 3.8 shows that galaxies at lower oxygen abundances have lower PAH luminosities compared to that expected from our fit between the total PAH luminosity and dust-corrected Hα for the higher metallicity galaxies. While the metallicity cut between the primary and secondary calibration samples is arbitrary, it defines the location where we observe a break in the $\rm L_{PAH}/L_{fit}$ ratios in figure 3.8. The strength of the PAH features is known to decline with decreasing metallicity (Engelbracht et al., 2005; Calzetti et al., 2007), which is likely driving the trend we see in figure 3.8.

We fit the secondary calibration sample with a robust linear fit routine (same as the PAH SFR relations) as shown in figure 3.8 for $12 + \log({\rm O/H})_{N2} \leq 8.55$. We derive metallicity-dependent corrections to the PAH luminosity for each PAH

Table 3.4. Metallicity Corrections

PAH Feature(s)	A
6.2 + 7.7 + 11.3	4.1 ± 0.3
6.2	4.0 ± 0.3
7.7	4.0 ± 0.3
11.3	3.7 ± 0.3
6.2 + 7.7	4.1 ± 0.4
6.2 + 11.3	3.8 ± 0.3
7.7 + 11.3	4.1 ± 0.3

Note. — Column 1 defines which PAH features were used for the fit (see figure 3.8, bottom). Column 2 is the linear relation coefficients for the metallicity corrections (defined as $\log L^{corr}_{PAH,\lambda} = \log L_{PAH,\lambda}$ - A[Z - ($Z_\odot$ + Z_0)], where Z_0 = -0.14).

combination as

$$\log L^{corr}_{PAH,\lambda} = \log L_{PAH,\lambda} - A[Z - (Z_\odot + Z_0)] \text{ for } 12 + \log(O/H)_{N2} \leq 8.55 \quad (3.13)$$

We define $Z_0 = Z_\odot - 8.55 = -0.14$. We do not have a sufficient number of low metallicity star-forming galaxies to determine if the fit between metallicity and $L_{PAH,\lambda}/L_{fit}$ is linear or more complex. For galaxies with $12 + \log(O/H)_{N2} > 8.55$, we force the ratio of L_{PAH}/L_{fit} to be unity. We need more super-solar metallicity galaxies to determine if this assumption is accurate. The metallicity corrections for each combination of PAH features is listed in table 3.4.

3.4.4 The Interesting Galaxy: II Zw 096

II Zw 096 is a high luminosity galaxy ($L_{IR} \sim 10^{12}$ $L_\odot$, Goldader et al., 1997; Haan et al., 2013) with almost solar metallicity ($\sim$0.8 $Z_\odot$) that is currently in the process of a merger (Brown et al., 2014). The PAH luminosity is much lower than

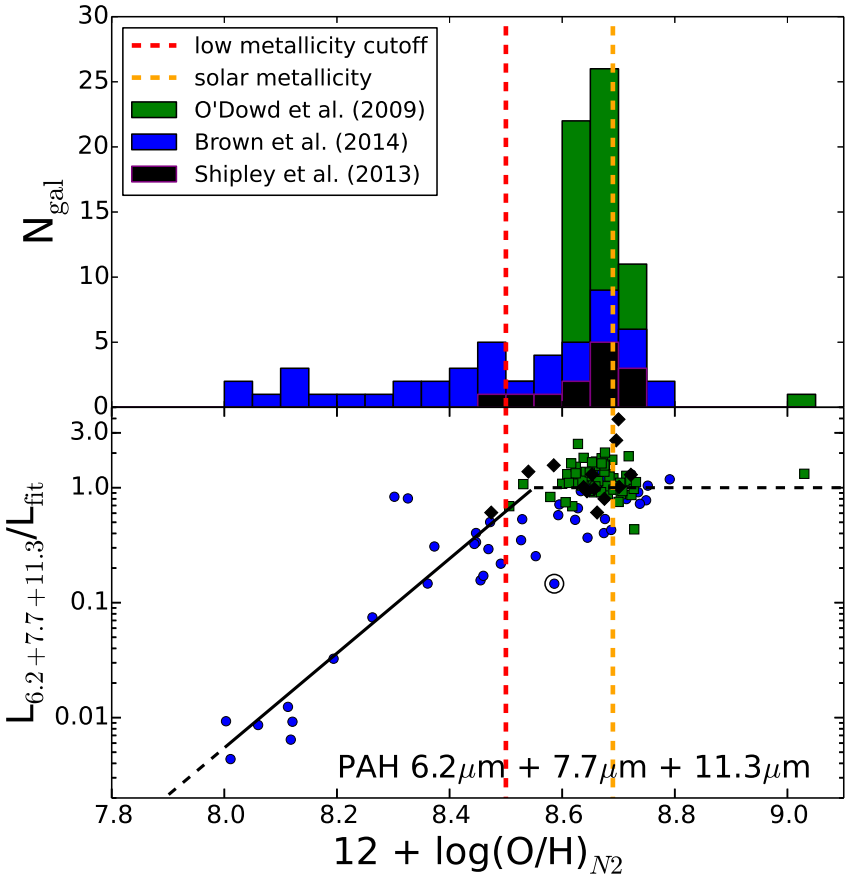

Figure 3.8 — The (Top) panel shows the same metallicity distribution for the star-forming galaxies in the calibration sample as figure 3.4. The (Bottom) panel shows the L_{PAH}/L_{fit} ratios for the star-forming galaxies as a function of oxygen abundance. This shows how the low metallicity galaxies result in weaker observed PAH emission than expected from the correlation. For the corrections to the PAH luminosity we used galaxies with $12 + \log(O/H)_{N2} \leq 8.55$. We determined a correction to the PAH luminosity by fitting a line (solid black line) for the galaxies below Z_0 ($Z_0 = Z_\odot - 8.55 =$ -0.14) and extrapolations (dashed black lines) beyond the sample limit (low end) and the fit (high end, see § 3.4.3 for more details). The blue point enclosed by a black circle denotes II Zw 096, see § 3.4.4.

that expected from the SFR calibration, and this makes II Zw 096 an interesting case study. Our primary calibration sample includes other merging systems (NGC 6090 and possibly SSGSS 18, Brown et al., 2014; Battisti et al., 2015) that lie on the relations and thus is not unique as to why II Zw 096 lies off the relations. We discuss here possible reasons for lower PAH emission that would shift it down from the SFR relations or other reasons that would shift it to the right of the SFR relations or a combination of both.

Interestingly, II Zw 096 does not have a low dust correction to the Hα luminosity ($\sim$6.2 , which resides in the bottom quartile shown in figure 3.3) as is the case for the low metallicity galaxies that would shift it to the right of the SFR relation and help explain this behavior. However, this does not rule out excess emission from Hα but allows for the possibility of increased 24μm luminosity, which results in an increased mid-IR emission that suppresses the PAH emission (Diamond-Stanic & Rieke, 2012; Shipley et al., 2013).

Goldader et al. (1997) identified four regions of intense star-formation, two associated with galactic nuclei of the system and two attributed to deeply obscured regions. The two nuclei star-forming regions show indications of hot ($T > 1000$ K) dust with the other two regions having considerably lower dust temperatures ($T < 750$ K). We see indications of this from the odd IR spectrum shape in Brown et al. (2014). Three of the regions are suspected to be very young starburst regions rich in OB stars, based on similarities to other merging systems in a similar evolutionary stage. Based on this picture this allows for the possibility the system has increased Hα emission from these very young starbursts where the formation of OB stars is not in equilibrium with their destruction (possibility for the low metallicity galaxies resulting in excess Hα emission for them). Furthermore, the two regions that are deeply obscured would lead to an increased 24μm luminosity and increased

mid-IR continuum possibly suppressing the PAH emission even further; thus shifting II Zw 096 to the right and down of the SFR relations and explaining its behavior.

Van Dokkum et al. (2005) showed evidence for shock ionization due to strong galactic winds can increase high ionization emission lines that mimics Seyfert-like line ratios, using models from Dopita & Sutherland (1995). This evidence for shock ionization would increase the $N2$ measured gas-phase metallicity for II Zw 096. This poses the possibility that the metallicity for II Zw 096 is intrinsically lower and the high [N II] λ6583 Å/Hα ratio indicates large quantities of shocked gas due to strong galactic winds. This would result in lower than expected PAH emission and shift II Zw 096 down from the SFR relations. For these reasons, we may expect that the SFR from Hα and the PAHs may disagree. It will be interesting to identify the frequency of these kinds of systems (merger induced recent star-formation) at high redshift, which will be possible by comparing SFR indicators of high redshift galaxies with *JWST*.

3.5 Comparison to Previous Studies of PAH SFR Calibrations

In this section, we discuss previous SFR calibrations for the PAH emission from single PAH features or combinations of features against various SFR indicators (total IR luminosity and atomic emission lines). This is a census of SFR calibrations derived for PAH luminosity. In the following sections, we discuss the differences for the selected methods and samples for each study separately. However, we summarize the main points from the comparison to the previous PAH SFRs in the following paragraphs. We note that the SFR relations in Kennicutt (1998) use a Salpeter IMF and our derived PAH SFRs are based on a Kroupa IMF as given in Kennicutt et al. (2009), which results in a scaling of 0.66 to those assuming a Salpeter IMF (Rieke et al., 2009). We take this into account and convert all SFR calibrations to a Kroupa

IMF when comparing the previous published PAH SFRs in this section that use the Kennicutt (1998) SFR relations.

A common theme presents itself in the comparison to other SFR calibrations. We have calibrated the PAH luminosity as a SFR tracer only for SFRs of $\approx 0.1 - 100$ $M_\odot$ yr^{-1} (see Figure 3.5). At SFRs $\gtrsim 100$ $M_\odot$ yr^{-1} ($L_{IR} \gtrsim 10^{12}$ $L_\odot$), this calibration may depart from the linear relation. As we discuss in this section, this may explain the discrepancy that the PAH SFR calibrations generally agree for IR luminoisities $< 10^{12}$ $L_\odot$, but diverge at higher IR luminosities. The PAH SFR calibrations in the literature can vary by up to an order of magnitude, and are calibrated over a wide range of L_{IR} (see Diamond-Stanic & Rieke, 2012; Hernán-Caballero et al., 2009; Sargsyan & Weedman, 2009; Treyer et al., 2010; Farrah et al., 2007; Fu & Stockton, 2009; Lutz et al., 2008; Pope et al., 2008). As we argue below, these differences likely arise from a combination of optical depth effects, and contributions from AGN to the thermal IR emission. Because we have carefully selected our primary calibration sample to be star-forming galaxies with about solar metallicity, we expect our sample to provide the most robust calibration of the PAH features.

There is possible evidence that the PAH SFR departs at IR luminosities $> 10^{12}$ $L_\odot$ from our PAH SFR calibration, even when previous samples have been carefully culled for indications of AGN. This may be expected because of optical depth effects in very dense, star-forming regions (Rieke et al., 2009). The SED templates from Rieke et al. (2009) show decreasing PAH emission with increasing IR luminosity. In particular, Rieke et al. (2009, figure 6) demonstrated this by normalizing the spectra to the same integrated flux and all the high luminosity SEDs overlap beyond 25μm, even as the PAH emission decreases with increasing luminosity.

Another potential effect is the contribution of AGN to the thermal IR emission. At IR luminosities $> 10^{12}$ $L_\odot$, AGN contribute to the overall IR emission (Sanders

& Mirabel, 1996), and deeply embedded AGN may be missed. This is evident from the previous PAH SFR calibrations for samples of ULIRGs that have significant contributions from AGN (see below). Because nearly all previous studies of ULIRGs give higher SFRs at fixed L_{PAH}, this may indicate an excess of AGN contribution to the SFR indicator (usually the total IR luminosity).

However, it is difficult to quantify the effect each has on this departure in the PAH SFR calibration we see for these high-luminosity objects with the current samples. Only further studies between PAH luminosities and accurate SFR indicators (such as dust-corrected Hydrogen recombination lines) of samples carefully screened for AGN will confirm these trends. Such a study would be adding star-forming ULIRGs to our current primary calibration sample presented here.

Given the various methods and samples used to derive previous PAH SFRs, it is remarkable the difference in the calibrations is relatively small (less than a factor of 2 for non-ULIRGs and the ULIRG samples agree within a factor of a few and we discuss this further in § 3.5.1 and § 3.5.2 for the individual studies). This possibly indicates that the PAH luminosity as a SFR indicator is generally robust regardless of redshift, sample selection or calibration method used that points to its accuracy over a broad range of conditions.

3.5.1 Comparison to PAH SFRs Calibrated to the Total Infrared Luminosity

Primarily, studies of PAH emission and its corresponding calibration as a SFR indicator have focused on calibrating the PAH luminosity with the total IR luminosity accomplished by using L_{PAH}/L_{IR} ratios and the L_{IR} SFR calibration from Kennicutt (1998), where the contribution of AGN to the total IR luminosity is assumed to be negligible.

3.5.1.1 Pope et al. (2008) Calibration

Pope et al. (2008) used a sample of eight galaxies (mostly ULIRGs) from a sample of 13 high-redshift sub-millimeter galaxies (SMGs), combined with local starburst galaxies to derive linear relations between PAH luminosity and total IR luminosity. Although, the SMGs fit on the trend their scatter is significantly more, likely due to lower S/N and possible contamination from AGN to the total IR luminosity. However, using the local starburst galaxies doesn't significantly change the linear relations between the total IR luminosity and the PAH luminosity for each PAH feature, but does result in larger scatter on the relations. From this, Pope et al. (2008) derived a SFR for the 6.2μm PAH feature using the IR SFR from Kennicutt (1998). The resulting PAH SFR scales by a factor of $\times$8 to our 6.2μm PAH SFR.

3.5.1.2 Lutz et al. (2008) Calibration

Lutz et al. (2008) used the L_{PAH}/L_{FIR} ratio derived in Schweitzer et al. (2006, and references therein) for 12 starburst-like ULIRGs, with an unknown contribution from AGN to the far-IR. They combine this with the IR SFR calibration from Kennicutt (1998) to derive a PAH SFR calibration, noting this relation assumes ULIRG-like physical conditions in the ISM of the observed galaxy. The calibration of Lutz et al. (2008) is different from the one here by a factor of $\times$5.5. This may be related to contribution from AGN to the total IR luminosity or to the definition of the total IR luminosity as the L_{FIR} from Lutz et al. (2008) is based on that of Sanders & Mirabel (1996) and differs from that in Kennicutt (1998).

3.5.1.3 Hernán-Caballero et al. (2009) Calibration

Hernán-Caballero et al. (2009) derived a PAH SFR using the L_{PAH}/L_{IR} ratios of seven bright, starburst-dominated galaxies at $0.6 < z < 1.0$ and the Kennicutt

(1998) IR SFR calibration. They derive SFR calibrations for each PAH feature (6.2μm, 7.7μm and 11.3μm). Compared to our results, the PAH SFR calibrations agree to within factors of $\times$1.4, 2 and 2.5 for the 6.2μm, 7.7μm and 11.3μm PAH features, respectively (the 11.3μm PAH SFR was mis-reported and should be 1.52×10^{-8}). Their estimated PAH SFRs can have uncertainties as large as factors of 2 due to the nature of the L_{PAH}/L_{IR} ratios (see Hernán-Caballero et al., 2009, for further discussion of issues that contribute to these uncertainties, as well as estimates from previous studies), when considering these uncertainties their SFR relations are brought more in line with our derived PAH SFR relations.

3.5.1.4 Fu & Stockton (2009) Calibration

Fu & Stockton (2009) used L_{PAH}/L_{IR} ratio from Veilleux et al. (2009) with the Kennicutt (1998) IR SFR relation to derive their SFRs. Veilleux et al. (2009) used 74 ULIRGs to determine the $L_{7.7\mu m}/L_{IR}$ ratio (reported as $L_{PAH}/L_{IR} = 0.0061$ in Fu & Stockton, 2009) with the average derived AGN contribution to the L_{IR} of 35-40%, which would result in an overestimation of the derived PAH SFR. Taking into account the average AGN contribution for the ULIRGs, the derived $L_{7.7\mu m}$ SFR (Fu & Stockton, 2009) results in a scaling factor of $\times$7 to our 7.7μm PAH SFR, interestingly a similar result to the previous studies (Lutz et al., 2008; Pope et al., 2008) for ULIRGs.

3.5.1.5 Sargsyan & Weedman (2009) Calibration

Sargsyan & Weedman (2009) investigated the PAH luminosity as a SFR indicator by comparing the radio emission (1.4GHz) and UV continuum estimated SFRs to the peak of the 7.7μm PAH feature by calibrating its PAH luminosity with the total IR luminosity using the Kennicutt (1998) IR SFR to derive a PAH SFR relation. The resulting PAH SFR agrees within a factor of $\times$0.4 to our PAH SFR for the

7.7μm feature. However, Treyer et al. (2010, see below) showed the $L_{IR}/L_{7.7\mu m}$ ratios resulted in an order of magnitude decrease from the integrated 7.7μm PAH feature flux to that of the peak. Their motivation for using the peak of the emission feature is if wavelength coverage is limited or the spectra have poor S/N such as might be the case in high redshift sources a SFR can still be estimated from the observed PAH emission. Only using the peak flux of the PAH features, however, does introduce possible issues with continuum contribution from AGN (increasing the mid-IR continuum flux as shown in Shipley et al., 2013) and will not be reliable in galaxies that host an AGN. Sargsyan & Weedman (2009) determined this not to be an issue for their sample of 287 starburst galaxies that have PAH $EW_{6.2} > 0.4\mu$m, which likely don't have strong AGN or a significant nuclear component contributing to the continuum flux. But introduces the possibility of composite sources that can increase the peak luminosity and/or low metallicity dwarf galaxies that have been shown to have weak PAH emission (see figures 3.5 and 3.8 and Calzetti et al., 2007; Engelbracht et al., 2005), where the former increases the estimated SFRs and the latter decreases the estimated SFRs resulting in larger scatter and uncertainties in the estimated SFR relation.

3.5.1.6 Treyer et al. (2010) Calibration

Treyer et al. (2010) performed an analysis similar to Kennicutt et al. (2009) for various Hα to IR luminosity ratios by considering smaller aperture corrections on the Hα emission (derived by Brinchmann et al., 2004) to estimate scaling factors for the various ratios using the star-forming galaxies from the SSGSS sample (O'Dowd et al., 2009, one of the three samples used to make our full calibration sample). They found consistent ratios to that of Kennicutt et al. (2009), especially for the 24μm luminosity and scatter and derived a new IR luminosity SFR (see Treyer et al., 2010,

for a detailed description of the derivation). The resulting PAH SFRs from this analysis agreed with our PAH SFRs within factors of $\times$1.3 and 1.6 for the 7.7μm and 11.3μm PAH features, respectively. Interestingly, the reported $L_{H\alpha}^{corr}/L_{PAH}$ ratios agree within factors of $\times$0.74 and 0.86 for the 7.7μm and 11.3μm PAH features, respectively.

3.5.1.7 Diamond-Stanic & Rieke (2012) Calibration

Diamond-Stanic & Rieke (2012) used SED templates (Rieke et al., 2009) to get a SFR from the 11.3μm PAH feature, which they found to be the most resistant to the influence of an AGN (Diamond-Stanic & Rieke, 2010). The estimated 11.3μm PAH SFR relation was derived for nuclear star-formation of AGN host galaxies using the Rieke et al. (2009) derived IR SFR relation and L_{PAH}/L_{IR} ratio for 11.3μm feature for galaxies with $L_{IR} < 10^{11}$ $L_{\odot}$. Diamond-Stanic & Rieke (2012) determined an uncertainty of 0.2 dex on the 11.3μm PAH feature SFRs and 0.2 dex uncertainty on the L_{IR} measurements so an uncertainty of 0.28 dex when combining the uncertainties in quadrature. The resulting relation agrees well with our sample (to within a factor of $\times$1.6), considering it is for nuclear star-formation in Seyfert galaxies and has a larger but consistent scatter.

3.5.2 Comparison to PAH SFRs Calibrated to mid-IR Atomic Emission Lines

Farrah et al. (2007) derived a PAH SFR from a sample of 53 ULIRGs using the 6.2μm and 11.3μm PAH features calibrating against the [Ne II] λ12.81μm and [Ne III] λ15.55μm emission lines. The choice for the PAH features and the reason to use both together was motivated by the fact that the PAH strengths of the individual PAH features can have variations observed between different starburst galaxies. The 6.2μm and 11.3μm PAH features were specifically used because of being bright and in a less crowded part of the spectrum, unlike the 7.7μm feature which can blend

with the less bright 8.6μm PAH feature. The calibration of the PAH features with the [Ne II] + [Ne III] luminosity resulted in SFR ($M_\odot$ yr^{-1}) = 1.18 $\times$ $10^{-41}L_{PAH}$ (erg s^{-1}) using the combined luminosity of the 6.2μm and 11.3μm PAH features to reduce the scatter (and assuming a Salpeter IMF).

Farrah et al. (2007) derived the relation using Ho & Keto (2007) for the [Ne II] λ12.8μm + [Ne III] λ15.6μm luminosity with their fit to the PAH luminosity and using an updated conversion of the Lyman continuum flux and star formation rate. They include a correction factor to account for the shorter timescales, "bursts", of star-formation to occur in ULIRGs as opposed to the assumed longer timescales used for the updated conversion in the Lyman continuum flux and the SFR derived from the Ne emission lines. Farrah et al. (2007) states that the errors on the derived SFRs are difficult to quantify. The errors on the SFR can be at least 50% for individual objects due to the uncertainty of the conversion of the Lyman continuum flux to star-formation rate and the large scatter in the calibration of the sample. However, galaxies showing signs of an AGN being present were not taken into account as the sample appears to have only 16 pure star-forming galaxies (AGN contribution on average is $\sim$25%). This would result in lower observed PAH emission and increase in [Ne II] + [Ne III] luminosity from contribution to the [Ne III] emission line. The conversion to a SFR from the PAHs would then lead to an overestimation, which may account for the differences observed in our calibration compared to that of Farrah et al. (2007).

3.6 SFRs of High Redshift (Lensed) Galaxies: A Preview for *JWST*

We demonstrate the utility of the PAH SFRs by measuring SFRs for the application sample of lensed high-redshift galaxies (§ 3.2.2). As mentioned previously, this provides a preview of studies possible with *JWST*, which will be sensitive to the

Table 3.5. Application Sample SFRs

SFR Indicator	A2218b	A2667a	The Clone	A2218a	A1835a	cB58	8 O'clock
Paα	...	...	< 6.5	61.2 ± 12.9	557. ± 105.	< 22.0	266. ± 29.4
Brα	78.6 ± 16.5	2.6 ± 6.6	...	...	...	< 52.4	...
6.2 + 7.7 + 11.3	27.2 ± 0.5	10.8 ± 0.3	8.3 ± 0.3	...	...	...	...
6.2	27.5 ± 0.3	8.1 ± 0.1	15.0 ± 0.6	68.6 ± 3.4	211. ± 39.4	11.1 ± 0.8	302. ± 20.0
7.7	28.5 ± 0.7	11.7 ± 0.4	7.3 ± 0.2	53.3 ± 1.3	168. ± 10.3	8.5 ± 0.4	262. ± 36.7
11.3	25.3 ± 1.0	11.4 ± 0.7	7.6 ± 1.2	...	...	...	...
6.2 + 7.7	27.9 ± 0.6	10.8 ± 0.3	8.6 ± 0.2	55.3 ± 1.2	173. ± 11.0	8.8 ± 0.4	265. ± 29.6
6.2 + 11.3	25.1 ± 0.5	9.4 ± 0.4	10.5 ± 0.7	...	...	...	...
7.7 + 11.3	27.7 ± 0.6	11.5 ± 0.4	7.3 ± 0.3	...	...	...	...

Note. — Column 1 denotes the SFR indicator that was used to derive the SFR for each galaxy (PAH SFRs were estimated using the unity relations given in table 3.2). Columns 2−8 are the estimated SFRs for each galaxy in the application sample (see § 3.6).

PAH emission from star-forming galaxies with SFRs as low as 10 $M_\odot$ yr^{-1} out to z < 2.5.

We derive SFRs for the application sample using measured line fluxes of the Paα and Brα emission lines, and assuming Case B recombination at electron temperature T_e = 10,000K and density N_e = 100 cm^{-3} (Osterbrock, 1989). We estimate the SFRs from the PAH features for the galaxies in the application sample using the PAH SFR calibration in Table 3.2. Table 3.5 lists the PAH-derived SFRs for the different combinations of PAH features for the application sample. Table 3.5 also lists Paα and Brα SFRs for these galaxies. Figure 3.9 shows a graphical comparison of the different SFRs for each galaxy in the application sample. Our PAH SFRs are consistent with the available SFR indicator for each galaxy, either Paα or Brα (see table 3.5). We see the most dramatic differences between our PAH SFRs and Brα for A2218b (section 3.6.1) and Paα for A1835a (section 3.6.2) and discuss possible reasons for these differences below. Figure 3.10 show this result for the 7.7μm PAH feature.

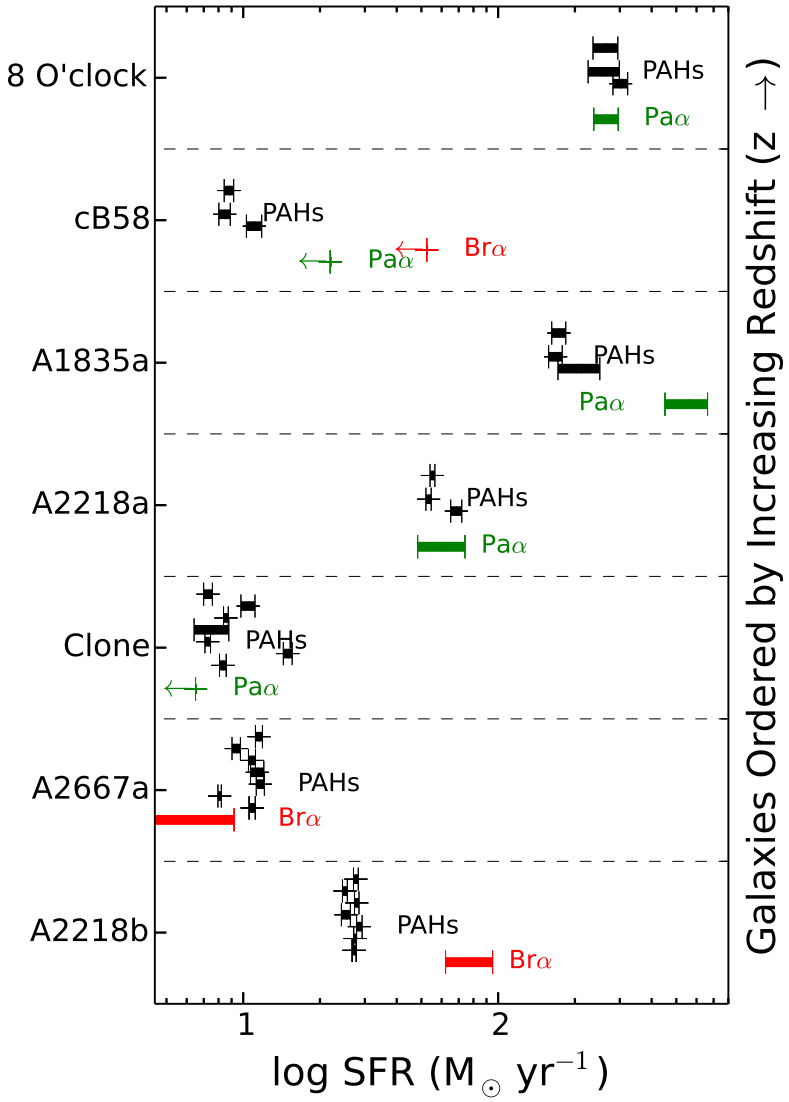

Figure 3.9 — SFRs for the application sample (labeled on the vertical axis with the galaxy's name) as given in table 3.5. We indicate the different SFR indicators as Paα, Brα and all the PAH features with green, red and black lines, respectively for the range in uncertainty of the estimated SFRs. The estimated PAH SFRs agree closely to each other as well as the other SFR indicators for most of these galaxies. In all cases, we do not increase the PAH SFRs for effects of low metallicity (see, e.g., § 3.6.2).

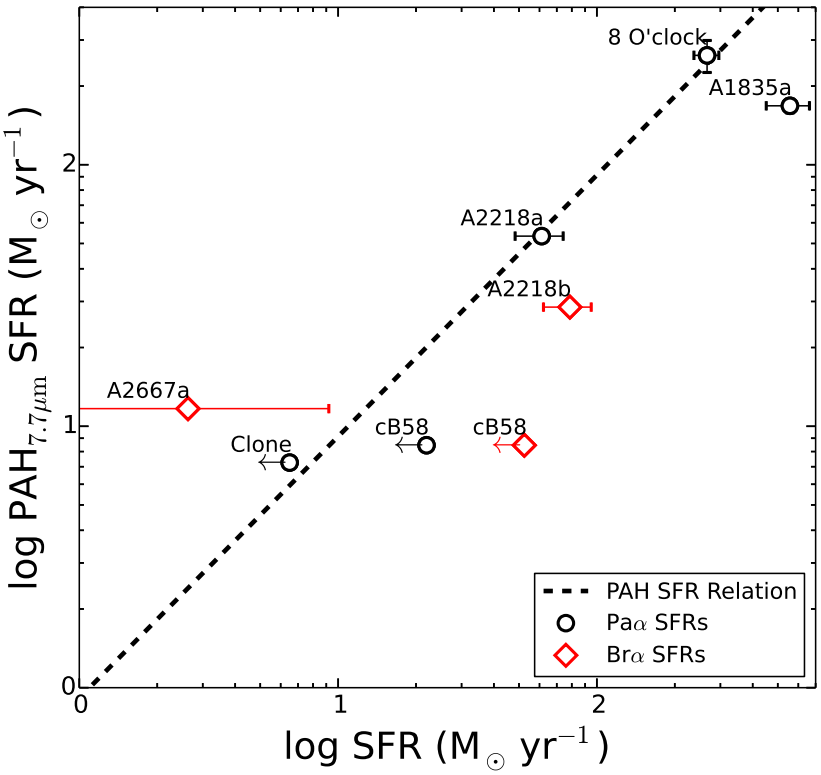

Figure 3.10 — The estimated SFRs from the PAH 7.7 μm in comparison to the estimated Paα (open black circles) and Brα (open red circles) SFRs for the application sample (some of the statistical uncertainties are smaller than the symbol size, primarily for the vertical axis; see § 3.6 for discussion). The line shown is the unity PAH 7.7 μm SFR relation from our calibration sample (§ 3.4.1) to the Paα and Brα SFR relations. Excluding the galaxies with upper limits or uncertainties larger than the measured fluxes (A2667a, The Clone and cB58) the galaxies lie along the relation for both SFR indicators to that of the PAH 7.7 μm SFR. Furthermore the galaxies (A2218b and A1835a) both show possible indications of an AGN, which would potentially cause an overestimation of their Paα and Brα SFRs resulting in a shift left back to the SFR relations, illustrating the robustness of the PAH SFRs.

3.6.1 SFRs for Galaxies at $z \sim 1$

For A2218b, the Brα SFR compared to the PAH SFRs is almost a factor of 3 larger. Inspection of the spectra in Rujopakarn et al. (2012, figure 2a) shows that the Brα emission line is weakly detected, with S/N < 5. Given the extended nature of this galaxy, aperture corrections may also be an issue, especially given likely contamination from a nearby (foreground) object in the slit. In contrast, the PAH emission is strongly detected with S/N $> 10 - 30$ for all features, where object contamination is less in the mid-IR. We therefore attribute the difference in SFRs to larger statistical and systematic uncertainties. This galaxy also highlights the fact that the PAH features are among the strongest SFR tracers in high-redshift galaxies that suffer minimal extinction effects.

A2667a has a large uncertainty on the Brα measurement, S/N < 1, and we treat it as an upper limit. This results in a low SFR for A2667a but agrees favorably with the PAH SFRs, the 1σ upper limit on the Brα SFR is within 20% of the PAH SFR. Interestingly, the log([N II]/Hα) ratio of -0.40 suggests the possibility of an AGN being present but is not definitive (Finkelstein et al., 2009a, figure 2) discussed similarly by Rujopakarn et al. (2012). This should result in a higher Brα SFR to that of the PAH SFRs (see figure 3.5, green and red symbols) as galaxies with AGN when observing the integrated light of a galaxy do not significantly affect PAH emission (Diamond-Stanic & Rieke, 2010; Shipley et al., 2013). However, the upper limit on the Brα emission does not allow for more quantitative comparisons.

3.6.2 SFRs for Galaxies at $2 < z < 3$

The Paα emission line is a stronger Hydrogen recombination line and it is detected at higher S/N in more galaxies compared to the Brα emission line. In two cases, A2218a, and the 8 oclock arc, the Paα SFRs and PAHs are highly consistent, as are

limits for The Clone and cB58. For A1835a, the Paα emission implies a SFR much higher than the SFR from the PAH emission. We discuss this galaxy, and the others in the $2 < z < 3$ application sample below.

A2218a is the best comparison between the different SFR indicators, in the application sample, due to the fact it has a very clean spectrum and reliable measured fluxes as discussed previously (see Rigby et al., 2008, section 4.1) and further shown for the atomic emission lines (see Rujopakarn et al., 2012, figure 3). A2218a gives the most consistent PAH SFRs to that of the Paα SFR and agree within the estimated statistical uncertainties in the application sample.

For the 8 o'clock arc, we derive SFR(6.2μm) = 302 $\pm$ 20 $M_\odot$ yr^{-1}, SFR(7.7μm) = 262 $\pm$ 37 $M_\odot$ yr^{-1} and SFR(6.2μm + 7.7μm) = 265 $\pm$ 30 $M_\odot$ yr^{-1}after correcting for the gravitational magnification. The *Spitzer*/IRS SL spectrum gives SFR(Paα) = 266 $\pm$ 29 $M_\odot$ yr^{-1} and the SFRs are comparable to those previously published from the rest-frame UV and other emission lines (Allam et al., 2007; Finkelstein et al., 2009b; Volino et al., 2010, accounting for different cosmologies and magnifications). The SFR derived from the 6.2μm feature is higher than that from the 7.7μm feature, although they are consistent within 1σ. This could also indicate that the PAH luminosity ratios of the ionized PAH features (6.2μm and 7.7μm PAH features, Draine & Li, 2001) may change, perhaps because of the higher ionization in these data (see Finkelstein et al., 2009b; Erb et al., 2014). However, the S/N of the data preclude more quantitative comparisons.

The Clone has only an upper limit for Paα for comparison. The galaxy is well detected in the PAH features, showing that the PAH features may be the brightest SFR indicator in distant galaxies. However, the Clone has been studied extensively and this allows for a more detailed comparison to previously published SFRs. The upper limit for Paα is based on a weak-detection of the emission line and the spectrum

shows an unknown emission feature that can not be attributed to Paα due to the redshift it would be at z$\sim$2.15 (see Rujopakarn et al., 2012, figure 4). The resulting upper limit Paα SFR is less than any of the estimated PAH SFRs. However, the previous published SFR of 32 $M_\odot$ yr^{-1} (Hainline et al., 2009; Lin et al., 2009) are higher than any of the PAH SFRs. We showed in figure 3.8 and discussed in § 3.4.3 that low metallicity results in weak PAH emission as this may be a possible reason for the underestimated PAH SFRs, where the Clone has a metallicity of $12 + \log(\mathrm{O/H})_{N2} = 8.49$. If we apply our metallicity correction (see equation 3.13) to the PAH luminosity, the estimated PAH SFRs increase by 75% to 15 $M_\odot$ yr^{-1}, in better agreement with the previously published values.

cB58 has upper limits for both Paα and Brα (see Rujopakarn et al., 2012). The upper limits provide Paα and Brα SFRs consistent with previously published SFRs, which range from $16 - 39$ $M_\odot$ yr^{-1} (e.g., Siana et al., 2008; Wuyts et al., 2012). The PAH SFRs fall slightly below the low end of this range. Again, we consider the likely lower metallicity of this galaxy, $12 + \log(\mathrm{O/H})_{N2} = 8.31$. Applying our metallicity corrections (see equation 3.13) results in an increase factor of $\times$9.5 and the mean SFR for cB58 becomes $\sim$85 $M_\odot$ yr^{-1}, well above more recent published values. We note for the metallicity correction to the PAH luminosity (§ 3.4.3) there are outliers that have the expected PAH luminosities even for lower metallicity galaxies (specifically, 2 galaxies at $12 + \log(\mathrm{O/H})_{N2} \sim 8.3$). If this is the case here, this would result in an overestimation (to an extent) of the PAH SFRs using the metallicity corrections.

For A1835a, the PAH SFRs are lower by a factor of 2 compared to the Paα SFR. Similar to A2667a, the presence of an AGN seems likely in A1835 given the log([N II]/Hα) emission line ratio of -0.25. To further explore this possibility we used X-ray data from Rigby et al. (2008) that quotes an upper limit on the total X-ray flux (0.5-8 keV) of 4.4×10^{-15} erg s^{-1} cm^{-2} resulting in a luminosity of $< 2.4 \times 10^{44}$

$L_\odot$. This upper limit of the X-ray luminosity does not rule out the possibility of an AGN. It therefore seems possible that the difference between the PAH and Paα SFRs results from an AGN contribution to the Paα emission line.

This provides encouraging evidence that our PAH SFR calibration is accurate for high-redshift ($1 < z < 3$) and very active (SFR $\sim 60 - 270$ $M_\odot$ yr^{-1}) galaxies. The PAH features may provide the most accurate SFRs that mitigate dust attenuation factors for distant galaxies, $z \lesssim 2.5$, with *JWST*/MIRI spectroscopy. The PAH features have much higher signal-to-noise ratios than Paα or Brα. This is because the PAH luminosities are brighter than the Paα and Brα emission lines by factors > 5. For this reason, the PAH features will be the brightest SFR indicators in high redshift galaxies, and the calibration we provide will have a large utility for studies with *JWST* of galaxies at the peak SFR density period in the Universe (Madau & Dickinson, 2014).

4. THE ROLE OF STAR-FORMATION IN GALAXIES FROM STARBURSTS TO QUASARS AS A FUNCTION OF TOTAL IR LUMINOSITY USING PAH EMISSION

4.1 Background

The coevolution of star-formation and supermassive black hole (SMBH) accretion in galaxies is one of the key problems in galaxy formation theory. This relation is important for understanding why at present the mass in galaxy bulges (on scales of kpc) correlates so tightly with the mass of galaxy central SMBHs (on scales of AU). Feedback from SMBH accretion is believed to be responsible for heating or expelling cold gas from galaxies, shutting off the fuel for star-formation and additional black hole growth. Did bulge formation proceed the formation of black holes, or vice versa, or are they contemporaneous or even unrelated? Understanding the exact rates of star-formation and SMBH growth, and how they evolve with time and galaxy mass has deep implications for how galaxies form.

One of the most surprising relations in astrophysics is that there exists a tight correlation between the mass of the SMBH and the bulges in galaxies (Ferrarese & Merritt, 2000; Gebhardt et al., 2000) now based on samples of nearly 100 galaxies (see Kormendy & Ho, 2013, for a recent review). Because the mass of the SMBH does not correlate with mass of galaxy disks or galaxy dark-matter halos, there is a now wide-spread belief that SMBHs and galaxy bulges coevolve by regulating each other's growth. It implies there is some connecting feedback mechanism in place that connects the growth of SMBHs to that of bulges.

The formation of a prominent bulge appears to be the driving reason for the quenching of star-formation in galaxies. As illustrated in a growing number of studies

(e.g., Franx et al., 2008; Wuyts et al., 2011; Bell et al., 2012; Papovich et al., 2012), galaxies with with large bulges have the lowest relative SFRs, and galaxies with pure disks have high relative SFRs. The reasons for this relation are not understood, but many theoretical models now attribute the cessation of star-formation in galaxies to feedback from accreting SMBHs (i.e., QSOs; Springel et al., 2005), which may expel cold gas from the galaxies altogether, shutting off the fuel for further star-formation and SMBH growth. This feedback mechanism and the physical processes that drive it are among the most active areas of astrophysical research, and significant questions remain. Understanding them is paramount for understanding galaxy evolution itself.

Mid-IR spectroscopy was first demonstrated to be an excellent tool for diagnosing processes related to star-formation and AGN for low-redshift sources (because of its inferior sensitivity) with *ISO* (e.g., Genzel et al., 1998; Rigopoulou et al., 1999; Laurent et al., 2000; Tran et al., 2001). More recently, *Spitzer* with the Infrared Spectrograph (IRS; Houck et al., 2004) provided the wavelength coverage and sensitivity to detect the mid-IR emission features in ultra luminous IR galaxies (ULIRGs) and classify them as AGN or star-formation powered out to $z \sim 3$ (Houck et al., 2005; Yan et al., 2005; Weedman et al., 2006; Armus et al., 2007; Spoon et al., 2007; Farrah et al., 2007, 2009; Hernán-Caballero et al., 2009; Veilleux et al., 2009; Diamond-Stanic & Rieke, 2010, 2012; Wu et al., 2010; Petric et al., 2011; Shipley et al., 2013). Many different mid-IR spectral diagnostics have been used to identify the contribution of AGN and star-formation to the total bolometric luminosity, including the strength of high ionization emission lines (e.g., [O IV] 25.9μm, [Ne V] 14.3μm) and the strength of PAH features (see Veilleux et al., 2009, for a summary). While many of these are very useful for bright sources with high-S/N data, the diagnostic features are faint, typically only detectable in bright, nearby objects with *Spitzer* or *ISO*.

Recent work suggests that the emission from polycyclic aromatic hydrocarbon

(PAH) molecules (which emit strongly in the mid-IR, 3-19 μm), correlates with the total SFR in star-forming galaxies. These features show strong variations between pure star-forming galaxies and those with AGN. Because they are so strong in mid-IR spectroscopic data, the PAHs potentially provide the most efficient means to quantify the amount of the bolometric emission from star formation. Several studies have used the PAH luminosities to estimate SFRs and the contribution of star-formation to the total IR (e.g., Pope et al., 2008; Kirkpatrick et al., 2012; Hernán-Caballero et al., 2009; Shipley et al., 2013). These studies on average find the AGN can contribute $\gtrsim$50% of the total IR luminosity. For galaxies with AGN the PAH features have been shown to continue to trace the SFR from the integrated light of the galaxy for AGN that are not the dominant source of the integrated light (Shipley et al., 2013). Furthermore, the 11.3μm PAH feature even in the presence of an AGN is not significantly attenuated around the nuclei by a study looking at this effect for nuclear versus off nuclear regions in Seyfert galaxies (Diamond-Stanic & Rieke, 2010). Therefore, the integrated PAH emission from a galaxy offers a tracer of the SFR even in galaxies with AGN.

From our previous work, we calibrated the PAH emission as a SFR indicator taking into account metallicity and AGN effects on the PAH features (Shipley et al., 2015) that we will utilize here for study of a sample of varying AGN activity (from starbursts to quasars) over a broad luminosity and redshift range. This study is intended to demonstrate the robustness of the PAH luminosity to trace star-formation in galaxies with strong AGN (i.e. quasars) and the possibility to study the role of star-formation and supermassive blackhole accretion contemporaneously in galaxies. The outline for the rest of this paper is the following. In § 4.2, we define our application sample and accompanying data. In § 4.3, we describe our analysis of the derived quantities for quasars in our application sample. In § 4.4, we present our distribution

function of the contribution from star-formation as a function total IR luminosity and the role of star-formation in quasars. In § 5, we present our conclusions. We assume a ΛCDM cosmology with $H_0 = 70$ km s^{-1}Mpc^{-1}, $\Omega_m = 0.3$, and $\Omega_\lambda = 0.7$ throughout this work.

4.2 Sample and Data

We carefully selected galaxies spanning a range of IR luminosity and nuclear activity that had full coverage of the *Spitzer*/IRS spectrum for the three brightest PAH features (6.2μm, 7.7μm and 11.3μm features) with *Spitzer*/MIPS 24μm observations and longer wavelength photmetry when available. We required the galaxies in our sample have reported gas-phase metallicities measured from the $N2$ index (Pettini & Pagel, 2004). We also required that the galaxies be sufficiently distant that the *Spitzer*/IRS contains the majority of the integrated light in the slit. In effect, this limits us to $z > 0.02$. The SL and LL modules of *Spitzer*/IRS have respective slit widths of $\sim$3$''$.7 and $\sim$10$''$.5, and the slits have physical sizes of 1.5 kpc and 4.3 kpc, respectively, at this redshift ($z > 0.02$). We set this requirement to properly determine the limits of the PAH luminosity to derive accurate SFRs in galaxies that host AGN. Furthermore, we needed galaxies that would cover the total IR luminosities from $10^9 - 10^{13}$ L$_\odot$ as best as possible for both star-forming and AGN classified galaxies. These criteria allow us to have starburst galaxies, low luminosity AGN and powerful quasars to better constrain the distribution functions, we intend to study.

We identified three samples that fit these criteria that have well calibrated *Spitzer*/IRS spectra and MIPS 24μm photometry. Also, many of the sources have longer wavelength photometry necessary to constrain the peak of the IR SED. The selected samples are from O'Dowd et al. (2009), Shipley et al. (2013) and Shi et al. (2014). We describe these samples in detail as they relate to our study in the following

sections. The resulting full sample includes 296 galaxies of the combined three independent samples covering $L_{IR} = 10^9 - 10^{12}$ $L_\odot$ for star-forming galaxies and $L_{IR} = 10^{10} - 10^{13}$ $L_\odot$ for the AGN.

We excluded from our full sample those galaxies with poor data quality, where we did not measure PAH feature fluxes in any of the three brightest PAH features (6.2μm, 7.7μm and 11.3μm features) or do not have measured MIPS 24μm band flux densities. We also excluded AGN from the Shi et al. (2014) sample that do not have MIPS 160μm and/or Herschel 160μm band flux densities as most are classified as quasars and longer wavelengths are necessary to estimate the total IR luminosity. We do include star-forming galaxies with only MIPS 24μm photometry as the estimated total IR luminosities agree closely when longer wavelength photometry is available. We further excluded galaxies that did not have gas-phase metallicities > 0.5 $Z_\odot$ from the $N2$ index (Pettini & Pagel, 2004), as described in Shipley et al. (2015), which results in a decrease of PAH emission. For this reason, we excluded galaxies from the First Look Survey (FLS) for the Shipley et al. (2013) sample that we do not have $N2$ gas-phase metallicities measurements. We do not have $N2$ index gas-phase metallicities for the Shi et al. (2014) sample. To handle this, we excluded galaxies below $L_{IR} < 10^{10}$ $L_\odot$. This decision was based on the well-known mass-metallicity relation (Tremonti et al., 2004). Most sources in the Shi et al. (2014) sample have $L_{IR} > 10^{10}$ $L_\odot$, and likely have higher stellar mass, and therefore higher abundance (e.g., based on Tremonti et al., 2004, galaxies with stellar mass $> 10^9$ $M_\odot$ have $>$ 0.5 $Z_\odot$). This reduced our full sample to 274 galaxies.

For the Shi et al. (2014) galaxies that remained in the full sample, we excluded galaxies with strong silicate emission at the 9.7μm feature. The reason for this is the spectral decomposition code we used to fit the *Spitzer*/IRS spectra does not treat or recover silicate emission that comes from AGN tori (see § 4.3.1). We excluded

galaxies with 9.7μm silicate feature strength > 0.2 (defined as $\ln(f^{\rm peak}/f^{\rm peak}_{\rm cont})$ in Shi et al., 2014). Furthermore, the silicate emission in some cases resembled blackbody emission and resulted in unreliable continuum fits. The final sample includes 220 galaxies that we define as the **application sample**. This allowed us to fit the mid-IR spectra for the application sample in the same method for all three samples.

4.2.1 O'Dowd et al. (2009) Sample

The O'Dowd et al. (2009) sample consists of 92 galaxies that covers a range in total IR luminosity of $L_{IR} = 10^9 - 10^{11}$ $L_\odot$ with a redshift of $0.03 < z < 0.22$ of mostly star-forming galaxies with few AGN systems of low luminosity. Compared to the solar oxygen abundance, 12 + log(O/H) = 8.69 (Asplund et al., 2009), the galaxies in the O'Dowd et al. (2009) sample span a narrow range around solar ($12 + \log(O/H)_{N2}$ $\approx$ 8.6 to 8.8). This sample has complete coverage of the optical spectra (using the emission line fluxes from the SDSS DR7, Tremonti et al., 2004, to estimate gas-phase metallicity and determine classification), IRS spectra and MIPS 24μm photometry taken from the published data. PAH luminosities are from O'Dowd et al. (2009, SSGSS sample) and total IR luminosities are from Shipley et al. (2013). All 92 galaxies from this sample fit our application sample criteria.

4.2.2 Shipley et al. (2013) Sample

The Shipley et al. (2013) sample consists of 65 galaxies covering a range in total IR luminosity of $L_{IR} = 10^{10} - 10^{12}$ $L_\odot$ with mostly higher IR luminosity compared to the O'Dowd et al. (2009) sample. The sample has a redshift of $0.02 < z < 0.6$ and half the sample comprised of galaxies with low luminosity AGN (classified as either composite or AGN sources). Compared to the solar oxygen abundance, 12 + log(O/H) = 8.69 (Asplund et al., 2009), the galaxies in the Shipley et al. (2013) sample span a range around solar ($12 + \log(O/H)_{N2} \approx$ 8.4 to 8.8). This sample

has complete IR coverage of the IRS and MIPS 24μm photometry with MIPS 70μm and 160μm photometry for many of the galaxies (see Shipley et al., 2013). The sample has complete optical spectroscopic data for 40 of the galaxies to determine optical classifications for the presence of AGN (only one ratio for BPT classification available for 14/40 sources). PAH luminosities and total IR luminosities are taken from Shipley et al. (2013). 50 galaxies from this sample fit our application sample criteria.

4.2.3 Shi et al. (2014) Sample

The Shi et al. (2014) sample consists of 139 galaxies covering a range in total IR luminosity of $L_{IR} = 10^{10} - 10^{13}$ $L_{\odot}$ of Palomar-Green (PG) and Two Micron All Sky Survey (2MASS) quasars. The sample has a redshift of $0.03 < z < 0.5$ and as described above gas-phase metallicities likely > 0.5 $Z_{\odot}$ from the total IR luminosities. This sample has complete IR coverage of the IRS with fully reduced and calibrated spectra publicly available for all sources (see Shi et al., 2014). The sample has complete MIPS 24μm photometry with MIPS 70μm and 160μm and/or Herschel 160μm photometry for many of the galaxies (2MASS quasars did not have Herschel 160μm photometry; refer to Shi et al., 2014). The optical classifications were identified from the respective PG and 2MASS surveys. As mentioned above, we excluded galaxies with the 9.7μm silicate emission feature > 0.2 from poor fits to the spectra continuum (see § 4.3.1). 78 galaxies from this sample fit our application sample criteria.

The PG quasars are defined by an average limiting B-band magnitude of 16.16, blue $U - B$ color (< -0.44), and dominant blackbody (star-like) appearance. All these sources show broad emission lines, and classified as type 1 quasars. As pointed out by Shi et al. (2014), due to the large photographic magnitude errors and the

simple selection based on color, the PG sample is incomplete (e.g., Goldschmidt et al., 1992; Jester et al., 2005), but the incompleteness is independent of the optical magnitude and color (Jester et al., 2005), this indicates that the PG quasar sample is representative of bright optically selected quasars. The 2MASS quasars represent a redder population with $J - K_s > 2$ (compared with a typical value of $J - K_s \sim 1.5$ for PG quasars), but have similar K_s-band luminosities ($M_{K_s} < -23$; Smith et al., 2002). The 2MASS sample includes sources with narrow to broad emission lines and thus be classified as type 1 and 2 quasars. Furthermore, the 2MASS sample is increasingly incomplete at Ks > 13 (Cutri et al., 2001).

4.3 Analysis of PG and 2MASS Quasars for Shi et al. (2014) Sample

We use the measured PAH luminosities and estimated total IR luminosities from our previous work (refer to § 4.2.1 and § 4.2.2) for the O'Dowd et al. (2009) and Shipley et al. (2013) samples and do not re-analyze them here. For this reason, our analysis focuses on the Shi et al. (2014) sample in the following sections to measure the PAH luminosities and estimate the total IR luminosities. We used the fully reduced and aperture corrected spectra provided by Shi et al. (2014) for our analysis here.

4.3.1 Spitzer IRS Spectral Fits

To determine flux estimates for the PAH features in the IRS spectra of our calibration sample, we used the PAHFIT spectral decomposition code (Smith et al., 2007), designed for *Spitzer* IRS data. PAHFIT uses a χ^2 minimization routine to fit a non-negative combination of multiple emission features and continua to the one-dimensional spectra of our sources. The features included in PAHFIT are the dust emission features from PAHs (modeled as Drude profiles), thermal dust continuum, continuum from starlight, atomic and molecular emission lines (modeled as

Gaussians), and dust extinction.

PAHFIT does not consider contributions from very hot (∼1000K) dust in strong AGN, and may not recover appropriate continuum levels in these types of sources. It also does not treat or recover silicate emission from AGN tori[1]. To address these limitations of the spectral decomposition code, with the goal of using it to have consistent fits for all three samples, we followed the procedure in Shi et al. (2014). The first modification was to model the hotter dust temperatures seen in AGN host galaxies. We used the dust temperatures given in Shi et al. (2014) that experimented on this set of spectra using the fixed temperatures of 1000, 580, 415, 210, 97, 58, 48, 41, 32, 29, and 26 K instead of the default set in PAHFIT. These temperatures were selected to avoid silicate absorption features (resulting in an underestimation of the continuum) and broad silicate emission features (that can mimic dust blackbody emission). Our other modification was to add in Gaussian emission to model the silicate emission at 9.7μm and 18μm with the goal of better fitting the continuum. We do this by adding in the Gaussian profiles to the default PAHFIT extinction model that we used for the other two samples. All other PAHFIT parameters are the same as used by O'Dowd et al. (2009) and Shipley et al. (2013) samples (see references for specific parameters used).

We fit the features in the IRS spectrum for each galaxy in Shi et al. (2014) for all 139 galaxies. Although, we were able to better fit the IRS spectra with our modification to PAHFIT; strong and/or broad silicate emission features are not well constrained. This resulted in poor continuum fits and over- or underestimation of the PAH feature flux densities (see figure 4.1). Our limit for reliable estimated PAH flux densities were for 9.7μm silicate feature strengths < 0.2 (defined as $\ln(f^{\rm peak}/f^{\rm peak}_{\rm cont})$ in Shi et al., 2014). We did not constrain ourselves to silicate emission at 18μm as

[1]see: http://tir.astro.utoledo.edu/jdsmith/research/pahfit.php

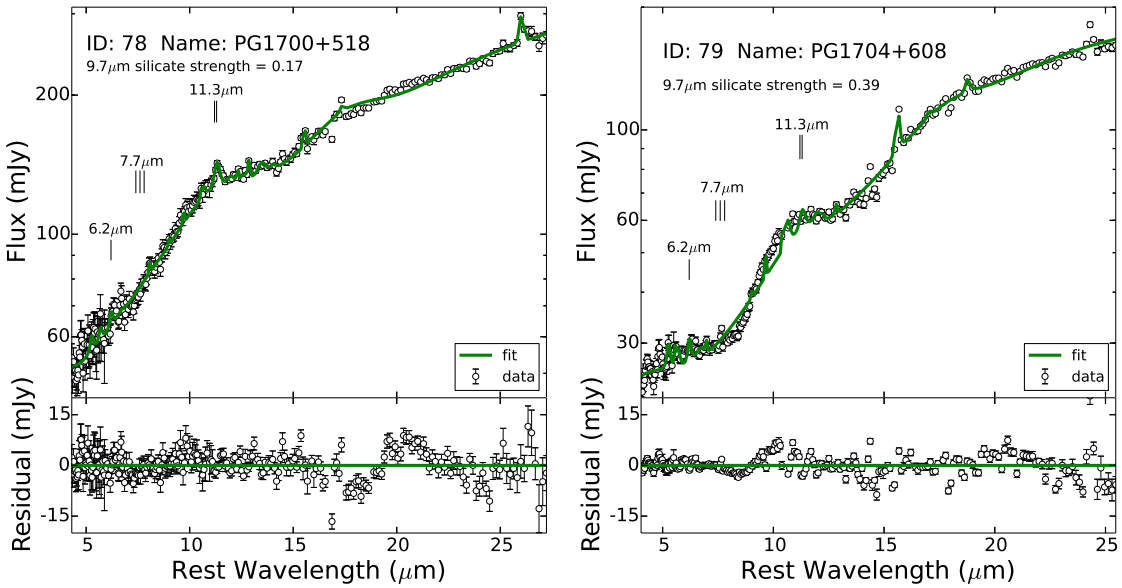

Figure 4.1 — In both panels, we show fits from the spectral decomposition code PAHFIT with our modifications to fit the silicate emission seen in the quasar sample from Shi et al. (2014). The open circles are the measured flux densities from the *Spitzer*/IRS data observations with error bars representing the uncertainties in those measurements and the green line represents the best fit from spectral decomposition of PAHFIT. The (Left) panel shows the best fit for a galaxy with silicate emission near our limit for reliable continuum fits with PAHFIT (9.7μm silicate strength = 0.17, see § 4.3.1). The (Right) panel shows the best fit for a galaxy with strong silicate emission beyond our limit for reliable continuum fits with PAHFIT (9.7μm silicate strength = 0.39, see § 4.3.1).

this did not effect our fits of our PAH features of interest (6.2μm, 7.7μm and 11.3μm features).

4.3.2 Total IR Luminosity

We estimate the total IR luminosity ($L_{IR} = L_{8-1000\mu m}$) using the MIPS 24μm, 70μm and 160μm and/or Herschel 160μm flux densities, when available from Shi et al. (2014) using the method in Shipley et al. (2013). We use the Rieke et al. (2009) IR SEDs because, for higher total IR luminosities, they took great care to

model the differences seen in the IR SEDs with increasing IR luminosities. This was important for properly estimating the total IR luminosity of the Shi et al. (2014) sample of PG and 2MASS quasars. For these reasons, it was important to have at least one longer wavelength band, preferably the 160μm band either from MIPS, Herschel or both to constrain the shape and peak of the IR SED to estimate accurate total IR luminosities.

To calculate the total IR luminosity, we simultaneously fit the available photometric bands (two to four bands) to the SEDs using a weighted mean with the uncertainty for each band. To avoid the 160μm band being overweighted, when both MIPS and Herschel photometry was available, we used a weighted mean for the two bands to create one 160μm photometric flux density with a corresponding uncertainty and then fit to the SEDs. We use these L_{IR} estimates with the previous L_{IR} estimates for the O'Dowd et al. (2009) and Shipley et al. (2013) samples from our previous work as described in § 4.2.1 and § 4.2.2, respectively.

4.4 Distribution Functions of Star-Formation and AGN Luminosities

4.4.1 Star-Formation as a Function of Total IR Luminosity

We estimate the SFRs from the PAH luminosity using the unity PAH SFR relations in Shipley et al. (2015). For our analysis here we use the three brightest features (6.2μm, 7.7μm and 11.3μm features) added together that we define as L_{PAH}. We also use the 11.3μm PAH feature alone as this has been shown to be the least affected by galaxies with AGN (Diamond-Stanic & Rieke, 2010; Shipley et al., 2013). Shipley et al. (2015) showed that L_{PAH} has a small scatter and uncertainty compared to the dust-corrected Hα luminosity. This should give the most robust measure of the SFR for galaxies over such a diverse range as this sample. The 11.3μm PAH SFR relation should offer a good comparison because of being the least affected PAH

feature in the vicinity of an AGN.

The sample covers a large range in total IR luminosity ($L_{IR} = 10^9 - 10^{13}$ $L_\odot$) resulting in PAH luminosities from $10^8 - 10^{11}$ $L_\odot$ with PAH SFRs from $0.1 - 200$ $M_\odot$ yr^{-1} (see figure 4.2) and a similar range for the 11.3μm feature only. The median total IR luminosities are 2.9×10^{10}, 2.8×10^{11}, 3.4×10^{11} $L_\odot$ for the O'Dowd et al. (2009), Shipley et al. (2013) and Shi et al. (2014) samples, respectively. We see that for increasing total IR luminosities their is an increase to the PAH luminosity (i.e. star-formation). Previous work has shown that the PAH features do not increase with increasing contribution from AGN (Smith et al., 2007; O'Dowd et al., 2009; Diamond-Stanic & Rieke, 2010; Wu et al., 2010; Shipley et al., 2013), indicating the SFR increases in all galaxies regardless of AGN activity with increasing total IR luminosity. The galaxies with strong AGN emission (i.e. quasars) have lower SFRs for similar IR luminosities compared to galaxies with little to no AGN emission (see figure 4.2). We discuss the quasars in more detail in § 4.4.2.

To estimate the contribution of luminosity from star-formation to the total IR luminosity, we converted the total IR luminosity into a SFR using the relations in Rieke et al. (2009). This was accomplished by estimating the IR SFRs using the 24μm luminosity as described in Rieke et al. (2009). We considered the uncertainties from the conversion of the purely star-forming SED derived SFRs to SFRs of galaxies with strong AGN emission. The 24μm estimated SFRs for quasars would be overestimated in this case. We corrected for this by using the linear relation to convert the total IR luminosity to 24μm luminosity given by Rieke et al. (2009).

$$\log L_{24\mu m} = (-1.529 \pm 0.156) + (1.058 \pm 0.016) \log L_{IR} \tag{4.1}$$

This allowed us to use the Rieke et al. (2009) 24μm SFRs, and yielded total IR

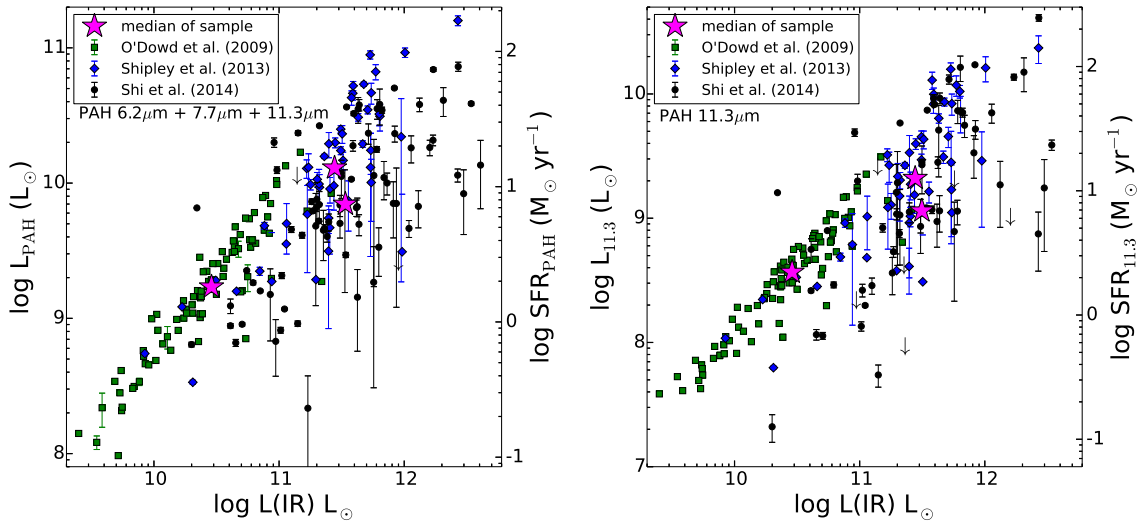

Figure 4.2 — In both panels, we show the total IR luminosity against the PAH luminosity (PAH SFR) for each sample (O'Dowd et al., 2009; Shipley et al., 2013; Shi et al., 2014, green squares, blue diamonds and black circles, respectively), where the magenta stars are the median values for each sample. The (Left) panel is the PAH luminosity from the three brightest PAH features (6.2μm, 7.7μmand 11.3μm), L_{PAH}. The (Right) panel is the PAH luminosity from the 11.3μm feature alone, which has been shown to be a better tracer of star-formation in galaxies with AGN (see § 4.4.1).

luminosity SFRs that do not overestimate the SFRs from 24μm luminosity alone. The 24μm SFR relations are defined differently for galaxies above and below $L_{IR} = 10^{11}$ $L_{\odot}$, where the 24μm luminosity peaks in comparison to the total IR luminosity. This method allowed the IR SFRs to be estimated using only the Rieke et al. (2009) SED templates to minimize uncertainties that may be introduced from using other IR SFR relations. We do notice this method to derive IR SFRs results in an underestimation of IR SFRs compared to the PAH SFRs at L_{IR} of $4 - 6 \times 10^{11}$ $L_{\odot}$. A possible reason for this is the linear fit to transform 24μm luminosity into IR SFRs above L_{IR} $= 10^{11}$ $L_{\odot}$. The relation shows a secondary peak for the 24μm luminosity compared to the total IR luminosity corresponding to this total IR luminosity range (Rieke et al., 2009). However, this simply could be due to individual galaxy variations or a combination of both effects.

In figure 4.3 for L_{PAH}, the median ratios for the total IR luminosity from star-formation to total IR luminosity ($L_{IR}(SFR_{PAH})/L_{IR}$) are 0.73 (interquartile range of 0.58 to 0.90, which contains the inner 50% of galaxies), 0.53 (interquartile range of 0.34 to 0.84) and 0.09 (interquartile range of 0.05 to 0.17) for the O'Dowd et al. (2009), Shipley et al. (2013) and Shi et al. (2014) samples, respectively. For the 11.3μm PAH feature only, the ratios for $L_{IR}(SFR_{11.3})/L_{IR}$ are 0.82 (interquartile range of 0.65 to 1.08), 0.56 (interquartile range of 0.33 to 0.94) and 0.10 (interquartile range of 0.05 to 0.24) for the O'Dowd et al. (2009), Shipley et al. (2013) and Shi et al. (2014) samples, respectively. This demonstrates for increasing total IR luminosity the contribution from star-formation decreases. The quasars from Shi et al. (2014) clearly show star-formation having contributions of $\sim$10% and ranging from 5% to 25%, but some of the quasars are dominated by SFR. This is possible evidence for quasars being an evolutionary stage of galaxies as many previous studies have developed models under this assumption (i.e., Hopkins et al., 2008, see below).

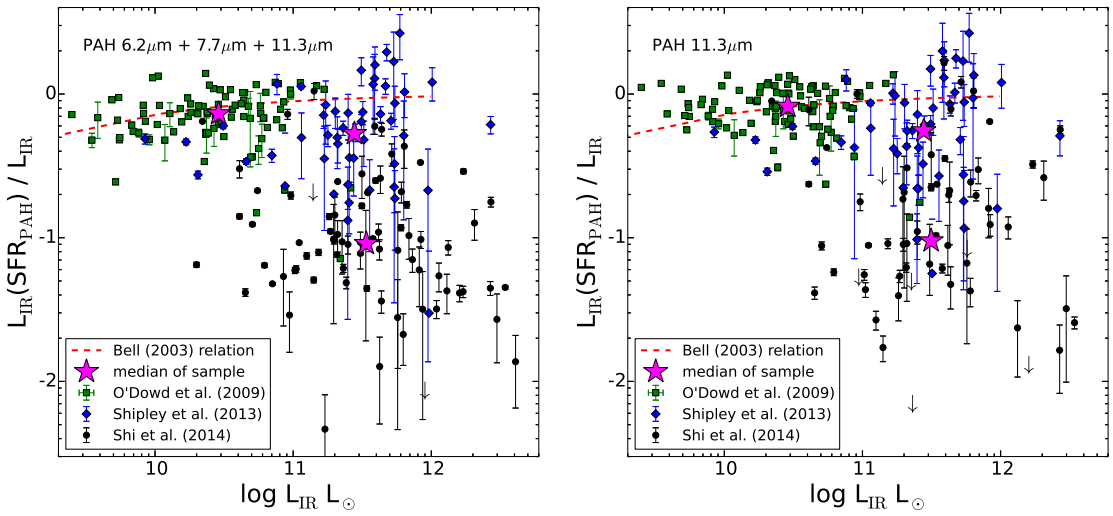

Figure 4.3 — The contribution of star-formation to the total IR luminosity as a function of the total IR luminosity. In both panels, we show the different star-formation contributions for each sample of O'Dowd et al. (2009, green sqaures), Shipley et al. (2013, blue diamonds) and Shi et al. (2014, black circles). The (Left) panel is for total PAH luminosity, L_{PAH}, where we see lower luminosity galaxies following the trend seen by Bell (2003) for IR excess emission (red dashed line) that lowers the star-formation contribution. The (Right) panel for the 11.3 μm feature follows the same trend but not as significantly as L_{PAH} for the lower SFRs at lower IR luminosities. The median values for the samples, in both panels, are given in § 4.4.1. This clearly shows a trend for decreasing contribution from star-formation with increasing IR luminosity. Furthermore, the contribution from star-formation during the quasar phase is significantly less than galaxies at similar IR luminosities.

There is a trend at lower total IR luminosities ($L_{IR} < 10^{11}$ $L_{\odot}$), where the PAH SFRs decrease with decreasing total IR luminosity. This relation arises from the total IR to far-ultraviolet (far-UV) attenuation corrections to the far-UV from the fact that galaxies at lower luminosities appear to be optically thin in the far-UV. This result indicates that the IR underestimates the SFR for low-luminosity galaxies (Bell, 2003). We fit the relation to this trend as characterized by (Bell, 2003).

$$\text{SFR } (M_{\odot}\ yr^{-1}) = 7.7 \times 10^{-11} L_{IR}(1 + \sqrt{\frac{10^9}{L_{IR}}})\ L_{\odot},\ \text{for } L_{IR} \leq 10^{11}\ L_{\odot}. \tag{4.2}$$

accounting for the differences in initial mass functions (IMFs). We have corrected the relation from Bell (2003) to account for the difference in IMF (going from Salpeter-like IMF in Bell 2003 to the "Kroupa" IMF here, which lowers the SFR by a factor of 0.66, see Rieke et al., 2009). Figure 4.3 illustrates the decrease seen in the SFRs at lower IR luminosities as the ratio of the PAH SFR to the IR SFR. The relation derived by Bell (2003) closely follows the purely star-forming galaxies in our sample (mostly the lower luminosity galaxies of O'Dowd et al., 2009, sample). This trend is also present for the 11.3μm feature but not as significantly as L_{PAH} (figure 4.3, right panel).

4.4.2 Star-Formation in Quasars

In figure 4.4, we demonstrate the estimated PAH SFRs for both SFR indicators (L_{PAH} and the 11.3μm feature). The PAH SFRs for both indicators agree quite well for the O'Dowd et al. (2009, $\sigma_{MAD} = 0.10$ dex) and the Shipley et al. (2013, $\sigma_{MAD} = 0.08$ dex) samples that include star-forming galaxies and low luminosity AGN sources. The Shi et al. (2014) sample of quasars agrees for the two PAH SFR indicators but with a larger scatter ($\sigma_{MAD} = 0.3$ dex). This larger scatter possibly

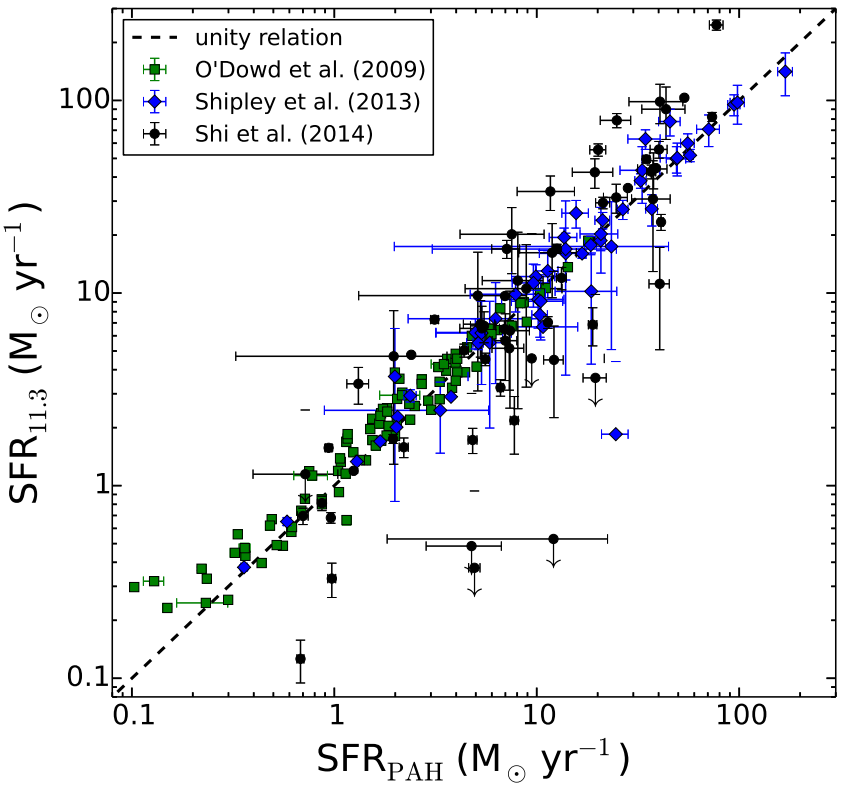

Figure 4.4 — PAH SFRs for the O'Dowd et al. (2009) sample (green squares), the Shipley et al. (2013) sample (blue diamonds) and the Shi et al. (2014) sample (black circles) estimated from L_{PAH} and the 11.3μm feature only. The SFRs span three orders of magnitudes from 0.1 to 300 $M_\odot$ yr^{-1}. The dashed black line represents a unity relation between the two SFR indicators.

resulting from the 11.3μm PAH feature being able to more accurately trace the SFR in the vicinity of an AGN. This would help to explain the higher estimated 11.3μm PAH SFRs for the higher IR luminosity quasars.

Figure 4.5 shows the derived SFRs for the quasars in the Shi et al. (2014) sample. The SFRs for the quasars are small (0.1 to 200 $M_\odot$ yr^{-1}) and generally fall in the range of $\sim$10 $M_\odot$ yr^{-1} with total IR luminosities $\sim$3 $\times 10^{11}$ $L_\odot$. The estimated SFRs for PG and 2MASS quasars are consistent with previous estimates from far-IR luminosity measurements (e.g., Shi et al., 2014). Furthermore, the luminosity

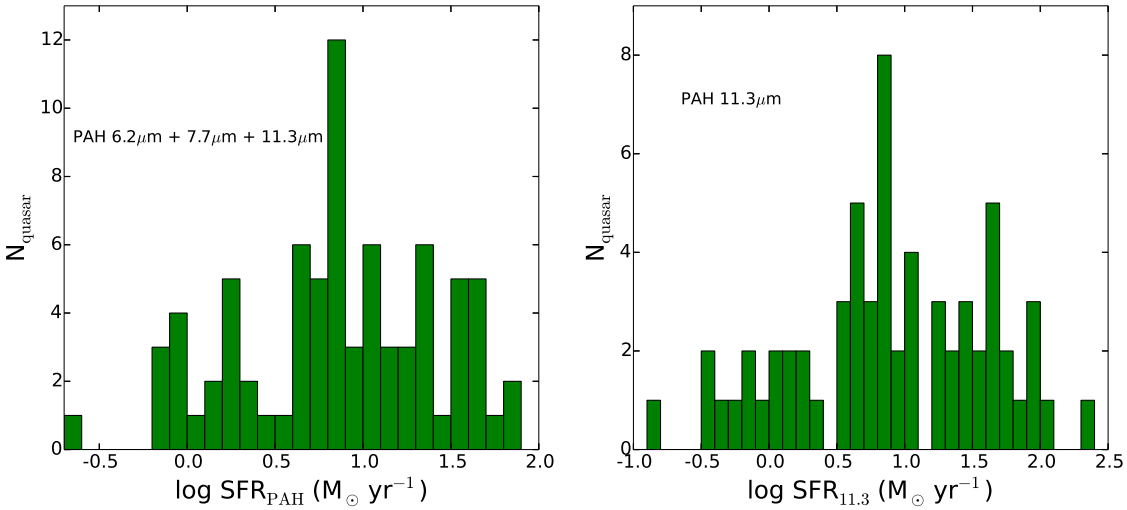

Figure 4.5 — SFRs for the quasars only from the Shi et al. (2014) sample estimated from L_{PAH} (Left) panel and the 11.3μm feature only (Right) panel. The SFRs span three orders of magnitudes from 0.1 to 200 $M_\odot$ yr^{-1} but the median and peak of the SFR in both panels is $\sim$10 $M_\odot$ yr^{-1}.

contribution from star-formation is assumed to be an upper limit (§ 4.4.1) as the majority of light does not come from the IR for these optically quasars, whereas most of the light for star-forming luminous IR galaxies is accounted for mostly by the total IR luminosity. This would lead to a greater separation then seen in our analysis here between the two types of activity.

4.5 Disscussion

4.5.1 The Correlation Between L_{SF} and L_{AGN}

A general correlation between SFR, i.e. IR luminosity from star-formation, and AGN luminosity for quasars has been observed by several previous studies (e.g., Lutz et al., 2008; Netzer, 2009; Shao et al., 2010). It has been suggested that the correlation implies a causal connection between star-formation and AGN activity. To evaluate these suggestions, I borrow from the derivation from Lei et al. (2015, in

preparation) the connection between the star forming luminosity and that of the AGN with the assumption the AGN hosts are normal galaxies, forming stars sufficiently to place them on the main sequence. For the purpose of the discussion the derivation given makes the assumption that their level of star formation is not necessarily affected by the presence of an AGN.

The first equation related the accretion rate of the blackhole mass expressed in terms of the Eddington limit to L_{AGN} (assuming an Eddington rate of $\epsilon \sim 0.1$ for luminous AGN). The next equation relates the SFR to the mass for galaxies on the main sequence and introduces the exponent β that has been derived for various studies ranging from 0.7 to 0.9, all consistent with 0.8. The last equation relates the SFR to L_{IR} for star-forming galaxies from Kennicutt (1998) taking into account the luminosity evolution of the star-formation by $\alpha \sim 3.2$ for $z < 1$ and smaller at higher redhifts. Combining the equations and the correlation for $M_*/M_\bullet = \eta \sim 700$ yields,

$$L_{SF} = C(1+z)^{\alpha}(\frac{\eta L_{AGN}}{\epsilon})^{\beta}, \tag{4.3}$$

The resulting equation is consistent with previous studies $L_{SF} \propto {L_{AGN}}^{\beta}$ with $\beta \sim 0.8$ (Lutz et al., 2008; Netzer, 2009; Shao et al., 2010). Lei et al. (2015, in preparation) found a best fit slope of $\beta = 0.59$. This derivation shows that this relation can arise through the dependence of both the SFR and the mass of the SMBH on the mass of the host galaxy, without any other connection between the two activity types.

In figure 4.6, we fit the relation between the SFR (i.e. luminosity of star-formation from PAHs) and the total IR luminosity ($L_{SF} \propto L_{IR}^{\beta}$) and as the star-formation only contributes ∼10%, this roughly relates to the total AGN luminosity for quasars ($L_{SF} \propto L_{AGN}^{\beta}$). We use a robust linear fit to the quasars and the best fit slope is found to be $\beta = 0.71 \pm 0.10$ for L_{PAH} and $\beta = 0.88 \pm 0.14$ for 11.3μm feature for

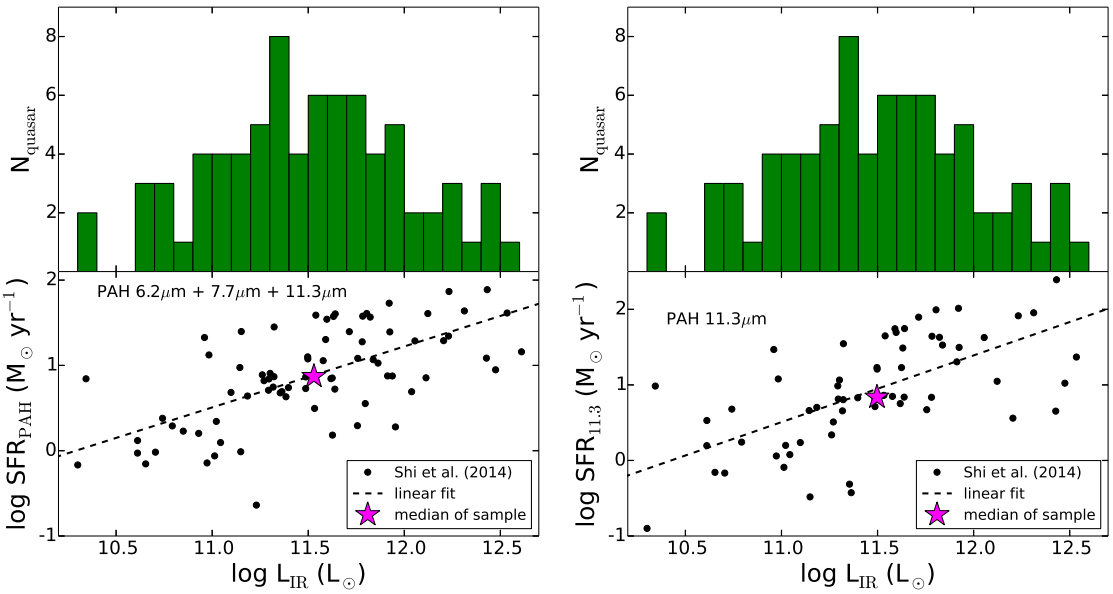

Figure 4.6 — In both panels, the top gives the total IR luminosities of the quasars from Shi et al. (2014) sample (interquartile range of $1-6\times10^{11}$ $L_\odot$. The bottom of each panel is the relation between the SFR (i.e. luminosity of star-formation) and the total IR luminosity ($L_{SF} \propto L_{IR}^{\beta}$) and as the star-formation only contributes ∼10% roughly the total AGN luminosity for quasars ($L_{SF} \propto L_{AGN}^{\beta}$). This demonstrates for increasing total IR luminosity the SFR increases. The best fit slope for this relation is $\beta = 0.71 \pm 0.10$ for L_{PAH} (Left) panel and $\beta = 0.88 \pm 0.14$ for 11.3μm feature (Right) panel for L_{IR}. If we remove the contribution from star-formation to the L_{IR} (i.e. L_{AGN}) we get a best fit slope of $\beta = 0.67 \pm 0.10$ for L_{PAH} and $\beta = 0.55 \pm 0.15$ for the 11.3μm feature, consistent with previous estimates of this relation (see § 4.5.1 for more detail).

the fit to L_{IR}. If we remove the contribution from star-formation to the L_{IR} (i.e. L_{AGN}) we get a best fit slope of $\beta = 0.67 \pm 0.10$ for L_{PAH} and $\beta = 0.55 \pm 0.15$ for the 11.3μm feature, consistent with previous estimates of this relation (see above). This provides encouraging evidence that the PAHs trace the SFR even in galaxies with strong AGN contributions as we did not remove the AGN component before estimating the PAH SFRs in the quasars.

4.5.2 Comparison to Models

Hopkins et al. (2008) developed a model connecting feedback from SMBH accretion (particular during the "Quasar" phase) during the merger of gas-rich progenitors. In this model, isolated galaxies form stars in gas-rich disks through normal disk instability processes. As the galaxies merge, torques drive gas to the nuclei where it fuels a massive starburst episode and SMBH growth. At later merger stages, the SMBH accretion and its luminosity peak, which drives radiative and mechanical winds, first shutting off star-formation and then the SMBH accretion itself. Such a model makes very strong predictions for the ratio of L(SFR) and L(AGN) as a function of total luminosity and merge state. For example, the peak period of $L_{\rm QSO}$ follows that of peak SFR, and this follows the "blow-out" phase which causes the cessation of star-formation. These predictions have yet to be tested because there has been no robust way to disentangle the contributions of star-formation and the AGN to the total luminosity. As we show here, PAHs offer a very promising way to measure simultaneously the distribution, $f(L(\mathrm{SFR}),\ L(\mathrm{SFR})/L(\mathrm{AGN}),\ L_{\rm tot})$ and how this evolves with redshift and galaxy morphological state. We study the quasar phase more closely in § 4.4.2, where we discuss the quasars from the Shi et al. (2014) sample separately.

If we assume the model in Hopkins et al. (2008) is correct, we can compare the median SFR in different luminosity bins to see if our estimated SFRs match the predictions with our limited data set. We chose to simply divide the luminosity into bins of $\mathrm{L_{IR}/L_\odot} \leq 10^{11}, 10^{11} < \mathrm{L_{IR}/L_\odot} < 10^{12}$ and $\mathrm{L_{IR}/L_\odot} \geq 10^{12}$. We find median SFRs in each $\mathrm{L_{IR}}$ bin of 2, 7 and 20 $\mathrm{M_\odot\ yr^{-1}}$ for $\mathrm{L_{PAH}}$ and median SFRs of 2, 7, 23 $\mathrm{M_\odot\ yr^{-1}}$ for the 11.3μm feature. The corresponding SFRs during the quasar phase for these luminosity bins from Hopkins et al. (2008) are ∼8, ∼15 and ∼100

$M_\odot$ $yr^{-1}$for the peak-up side before merger and ∼1, ∼8 and ∼100 $M_\odot$ $yr^{-1}$for the peak-down side after merger (the "qausar" phase). While, we do not agree for the highest luminosity bin ($L_{IR} > 10^{12}$ $L_\odot$) there is reasonable agreement for the two lower luminosities bins for both sides of the peak for L_{QSO}. Furthermore, the peak SFRs for Hopkins et al. (2008) model are ∼200 $M_\odot$ yr^{-1} consistent with our highest quasar SFRs. This may indicate these quasars are at the peak of the quasar phase and that the predictions from this model generally agree with our observations here.

5. SUMMARY AND CONCLUSIONS

In § 2, we have studied a sample of 65 galaxies with spectroscopic redshifts of 0.02 $<$ z $<$ 0.6 using *Spitzer* IRS mid-IR spectroscopy, combined with *Spitzer* imaging and ground-based observations that have flux densities of $f_\nu(24\mu\mathrm{m}) > 1.2$ mJy. The galaxies have a total IR luminosity from $\sim 10^{10}\mathrm{L}_\odot$ to more than $10^{12}\mathrm{L}_\odot$, with a median of $3.0\times10^{11}\mathrm{L}_\odot$, which we estimate using the observed MIPS 24 μm data (and 70 and 160 μm when available) combined with Rieke et al. (2009) IR SED templates.

We use an IRAC color–color selection (Stern et al., 2005) to identify IRAGN and non-IRAGN for galaxies in our sample. Our sample includes a wide range of IR-luminous galaxies at redshifts where such galaxies dominate the cosmic IR-luminosity density and SFR-density and they therefore provide insight into the physical processes within these galaxies.

We have shown the measured PAH emission can contribute 11% (75th percentile) or more of the total IR luminosity and half that or slightly more can come from the 7.7μm feature alone, for either the non-IRAGN or IRAGN. The detection frequency of PAH emission (for all features) in the non-IRAGN sample is uniformly more than twice that for IRAGN, except for the 11.3μm feature which is detected only about 1.5 times more frequently in non-IRAGN.

We do not see a significant difference between IRAGN galaxies and non-IRAGN galaxies for short-to-long PAH ratios (namely the 7.7μm-to-11.3μm ratio versus the [Ne III]/[Ne II] ratio) in contrast to other studies (Smith et al., 2007; O'Dowd et al., 2009; Wu et al., 2010). However, the sample galaxies used by these other studies include more nearby galaxies, where the IRS slit encompasses only the nuclear

emission. In our sample, the IRS slit contains more of the integrated emission from the galaxy. The data used by these other studies are therefore more sensitive to the destruction of smaller grains from AGN-driven shocks that lower the emission of shorter wavelength PAH features (6.2μm and 7.7μm features, Diamond-Stanic & Rieke, 2010). We investigated this by using the H_2 S(3) rotational line (at 9.67μm) and found that none of our galaxies had strong H_2 emission. In fact, we did not have many detections of H_2 emission (only 10 of 65 galaxies have H_2 flux detections at $\geq 3\sigma$) for our sample. This result suggests that if shocks are present in the members of our sample they are not strong enough to dramatically alter the observed short-to-long PAH ratios.

The PAH emission correlates very tightly with the [Ne II] emission. We conclude that both processes correlate with the total SFR, implying that we can use the PAH emission to estimate the contribution of star-formation to the total IR luminosity in the IRAGN. As expected for the IRAGN, the dominant source of IR luminosity comes from the AGN. In fact, we find only about 10%–50% of the contribution comes from star-formation for most of the IRAGN in our sample. The IRAGN have lower [Ne II] emission indicating that the presence of an AGN does not require strong star-formation, and/or that the presence of an AGN suppresses star-formation. The PAH emission does not correlate as well with [O IV] emission, which is more sensitive to the ionization radiation from the AGN. At a basic level, this shows that AGN do not increase PAH emission. We do identify a population of galaxies with low PAH emission and excess [O IV] emission, indicative of heavily-obscured AGN. Of the eight galaxies with excess [O IV] emission, three are non-IRAGN, with no other indications of AGN from their IRAC colors or optical spectroscopy. Nonetheless, two of these three have suppressed PAH features indicating they have obscured AGN; the third shows no such effects, and its AGN may be very strongly obscured.

Investigating the color-magnitude relation, the IRAGN span the full range of $(u-r)_{0.1}$ colors as do the non-IRAGN for the full sample of IR-luminous galaxies. The optical colors of the IRAGN are more consistent with the distribution of other AGN samples, mostly populating the top of the star-forming blue sequence to the red sequence (see, e.g., Nandra et al., 2007; Weiner et al., 2007). Because no significant difference is seen between IRAGN and non-IRAGN, it is unclear if the presence of an AGN is driving redder $(u-r)_{0.1}$ colors in the IRAGN of IR luminous galaxies. Moreover, most of the IRAGN have lower star-formation (because they show weak [Ne II] emission). Therefore, star-formation is not a necessary component for an AGN to persist.

In § 3, we have studied a sample of 105 star-forming galaxies covering a range of total IR luminosity, $L_{IR} = L(8\text{-}1000\mu m) = 10^9 - 10^{12}$ $L_\odot$ and redshift $0 < z < 0.4$ to calibrate the luminosity of the PAH features at $6.2\mu m - 11.3\mu m$ as SFR indicators. The total PAH luminosity ($6.2\mu m$ + $7.7\mu m$ + $11.3\mu m$ features) correlates linearly with the SFR as measured by the dust-corrected Hα luminosity (using the sum of the observed Hα emission and corresponding $24\mu m$ luminosity as established by Kennicutt et al., 2009), with a tight scatter of $\sim$0.15 dex. The scatter is comparable to the scatter between SFRs derived from the Paα (Calzetti et al., 2007) and dust-corrected Hα emission lines (Kennicutt, 1998), implying the PAH features may be as accurate a SFR indicator as the Hydrogen recombination lines.

We have provided a new robust star-formation rate (SFR) calibration using the luminosity emitted from the PAHs at $6.2\mu m$, $7.7\mu m$ and $11.3\mu m$ and all possible combinations. The scatter is smallest, $\sigma_{MAD} = 0.14$ dex (i.e., 40%) whenever the $7.7\mu m$ feature is involved in the fit. This implies this feature may provide the most robust measure of the SFR. The relation against the $6.2\mu m$ feature has the highest scatter, $\sigma_{MAD} = 0.21$ dex (i.e., 60%), which may indicate more variation in galaxies

between the luminosity in this feature and the SFR.

The PAH SFR calibration showed a dependency on galaxy gas-phase metallicity, where the PAH luminosity of galaxies with $Z \lesssim 0.7\ Z_{\odot}$ departs from the linear SFR relationship. We have calibrated a correction to the PAH SFRs using a simple empirical model that depends linearly on metallicity for a sample of 25 galaxies. Larger samples of low metallicity galaxies are necessary to improve the accuracy of these fits on the dependence of gas-phase metallicity and reduce the scatter seen in the metallicity relations.

We have presented a case study for observations from *JWST* that will be capable of measuring the PAH luminosities in galaxies to $z \lesssim 2.5$. Because the PAH features are so bright, our PAH SFR calibration enables an efficient way to measure SFRs in distant galaxies with *JWST* to SFRs as low as $\sim$10 $M_{\odot}\ yr^{-1}$. We used *Spitzer*/IRS observations of PAH features in seven lensed star-forming galaxies at $1 < z < 3$ to demonstrate the utility of the PAHs to derive SFRs as accurate as those available from any other indicator. For the galaxies (A2218a and 8 o'clock arc) with the best measured emission fluxes and most reliable spectra (A2218a), we see the most consistent SFRs between the PAH SFRs and Paα SFRs.

This illustrates the PAH features may provide the most accurate SFR measurements for distant galaxies, $z \lesssim 2.5$, with *JWST*/MIRI spectroscopy with much higher signal-to-noise ratios than other SFR indicators. This is because the PAH luminosities are brighter than most other SFR indicators (Paα and Brα) with S/N higher by factors of $> 5-10$ in comparable exposure times. For this reason, the PAH features will be the brightest SFR indicators in high redshift galaxies, and the calibration we provide will have a large utility for studies with *JWST* of galaxies in the distant universe.

In § 4, we have presented a study of the contribution of star-formation in galaxies

of varying AGN activity from star-forming galaxies to quasars as a function of total Infrared (IR) luminosity using a sample of 220 galaxies. The sample spans a range of total IR luminosity, L_{IR} = L(8-1000μm) = $10^9 - 10^{13}$ $L_\odot$ and redshift $0 < z < 0.6$ with about solar gas-phase metallicities. We use mid-IR spectroscopy from the *Spitzer* Infrared Spectrograph (IRS) and photometry from the MIPS 24μm, 70μm and 160μm bands with partial coverage of the sample with the Herschel 160μm band for the quasars. We derive distribution functions for the star-formation from the polycyclic aromatic hydrocarbon (PAH) star-formation rates (SFRs).

We found a similar result to previous studies for the correlation between SFR, i.e. IR luminosity, and AGN luminosity for quasars of $L_{SF} \propto L_{AGN}^{0.67\pm0.10}$ (and $L_{SF} \propto L_{AGN}^{0.55\pm0.15}$ for the 11.3μm PAH feature only). This may indicate the PAH luminosity remains a reliable tracer of the total SFR for galaxies with strong AGN contributions (i.e. quasars), as we did not subtract off the AGN component before measuring the star-formation from the PAH luminosity.

We found the distribution function of the luminosity from star-formation to the total IR luminosity decreases with increasing total IR luminosity. We estimate star-formation contributes $\sim$10% (interquartile range of 5%$-$20%) to the total IR luminosity for quasars. The 11.3μm PAH feature only gives a slightly larger result for the interquartile range (5%$-$25%), which has been shown to be more reliable in galaxies with AGN when observing the integrated light of a galaxy. For star-forming galaxies and low luminosity AGN, we estimate the contributions from star-formation to the total IR luminosity to be $\sim$70% (interquartile range of 50%$-$90%) and the 11.3μm PAH feature to be $\sim$80% (interquartile range of 55%$-$100%). We observed a decrease in the SFRs at lower IR luminosities for the ratio of the PAH SFRs to the IR SFRs. We found the relation derived by Bell (2003) closely follows the purely star-forming galaxies in our sample (mostly the lower luminosity galaxies of O'Dowd

et al., 2009, sample).

We have compared the predictions from Hopkins et al. (2008) to our sample of quasars and found the SFRs generally agree with the AGN luminosity during the quasar phase. While, we do not agree for the highest luminosity bin ($L_{IR} > 10^{12}$ $L_{\odot}$) there is reasonable agreement for the two lower luminosities bins for both side of peak L_{QSO}. However, the peak SFRs for Hopkins et al. (2008) model are $\sim$200 $M_{\odot}$ yr^{-1}consistent with our highest quasar SFRs. This may indicate these quasars are at the peak of the quasar phase and that the predictions from this model are consistent to our measured PAH SFRs.

This multistage study takes important steps to further our understanding of galaxy evolution, specifically calibrating a new SFR indicator (i.e. PAHs) to give valid SFRs in galaxies that host AGN. Further progress can still be made in calibrating the PAH features by adding pure star-forming ULIRGs to our primary calibration sample here. The reason to do this is the discrepancy between PAH SFR relations calibrated with samples of ULIRGs and non-ULIRGs as described in § 3.5. However, this currently remains a challenge as pure star-forming ULIRGs are rare.

Another future project is to obtain spectra that covers the important Paα emission line as an independent calibration for the PAH features (a less robust calibration of the mid-IR continuum was previously undertaken by Calzetti et al., 2007). The observations will be for a modified sample of my current calibration, that is allowed by the wavelength range of current telescopes/instruments (only excludes a few galaxies), plus star-forming ULIRGs (see above). The beneficial reason to do this is Paα has very little extinction compared to Hα, which currently I'm correcting using 24μm luminosity resulting in a significant contribution to the dust correction (see § 3.3.3), and comparison to Paα would allow this uncertainty to be removed. Using Paα allows for tests to better constrain the high mass end of the initial mass function (IMF), as

Paα probes O and B stars, where the correction from 24μm emission currently being used has significant contributions from A and F stars. Therefore, this will allow me to improve the calibration and help give better constraints on star-formation in galaxies that host AGN.

With future telescopes such as *JWST* it is possible to utilize the PAH features to measure valid SFRs from photometric observations with *JWST*/MIRI. This can be accomplished by taking the results presented in this thesis and calibrating the PAH features for photometric bands. An example is to calibrate the 8μm emission for the 7.7μm PAH feature that can be used for future *JWST*/MIRI observations as a star-formation indicator in star-forming galaxies out to z $<$ 3.

We have started to add quantitative descriptions to the interaction between star-formation and SMBH accretion in galaxies by measuring the star-formation of a large sample of galaxies from pure star-forming galaxies to quasars (i.e. luminous AGN). Future progress will be made by constructing a direct comparison to co-evolution models (i.e. Hopkins et al., 2008) to more thoroughly study this co-evolution. Many of the galaxies in the sample (and other samples we plan to add) have *HST* imaging that will allow us to determine evolutionary stages from morphology and construct a direct observation model of this co-evolution that are currently lacking.

Because of how bright the PAH features are it will be possible to determine if the modes of AGN are the same or different at higher redshift. Furthermore, studies of the co-evolution of star-formation and AGN will be to add better constraints for determining if AGN activity comes before the cessation of star-formation or is it concurrent in galaxies. Quantitive descriptions are currently lacking for these questions. From the work presented in this thesis, I will be poised to make contributions to help answer these questions.

The PAH features will be the brightest SFR indicators in high redshift galaxies,

and the calibration we provide will be useful for future studies of galaxies in the distant Universe. This new SFR indicator will be useful for probing the peak of the SFR density in the Universe ($1 < z < 3$). Furthermore, this study provides encouraging evidence that the PAHs trace the SFR even in galaxies with strong AGN contributions (i.e. quasars). These PAH SFR indicators will allow for direct studies of the co-evolution of star-formation and supermassive blackhole accretion contemporaneously in a galaxy (as demonstrated here) that will be an important tool in our understanding of galaxy evolution.

REFERENCES

Allam, S. S., Tucker, D. L., Lin, H., Diehl, H. T., Annis, J., Buckley-Geer, E. J., & Frieman, J. A. 2007, The 8 O'Clock Arc: A Serendipitous Discovery of a Strongly Lensed Lyman Break Galaxy in the SDSS DR4 Imaging Data, ApJ, 662, L51–L54

Allamandola, L. J., Tielens, A. G. G. M., & Barker, J. R. 1985, Polycyclic Aromatic Hydrocarbons and the Unidentified Infrared Emission Bands - Auto Exhaust Along the Milky Way, ApJ, 290, L25–L28

Allamandola, L. J., Tielens, A. G. G. M., & Barker, J. R. 1989, Interstellar Polycyclic Aromatic Hydrocarbons - The Infrared Emission Bands, the Excitation/Emission Mechanism, and the Astrophysical Implications, ApJS, 71, 733–775

Armus, L., Charmandaris, V., Bernard-Salas, J., Spoon, H. W. W., Marshall, J. A., Higdon, S. J. U., Desai, V., Teplitz, H. I., Hao, L., Devost, D., Brandl, B. R., Wu, Y., Sloan, G. C., Soifer, B. T., Houck, J. R., & Herter, T. L. 2007, Observations of Ultraluminous Infrared Galaxies with the Infrared Spectrograph on the Spitzer Space Telescope. II. The IRAS Bright Galaxy Sample, ApJ, 656, 148–167

Ashby, M. L. N., Stern, D., Brodwin, M., Griffith, R., Eisenhardt, P., Kozłowski, S., Kochanek, C. S., Bock, J. J., Borys, C., Brand, K., Brown, M. J. I., Cool, R., Cooray, A., Croft, S., Dey, A., Eisenstein, D., Gonzalez, A. H., Gorjian, V., Grogin, N. A., Ivison, R. J., Jacob, J., Jannuzi, B. T., Mainzer, A., Moustakas, L. A., Röttgering, H. J. A., Seymour, N., Smith, H. A., Stanford, S. A., Stauffer, J. R., Sullivan, I., van Breugel, W., Willner, S. P., & Wright, E. L. 2009, The Spitzer Deep, Wide-field Survey, ApJ, 701, 428–453

Asplund, M., Grevesse, N., Sauval, A. J., & Scott, P. 2009, The Chemical Composi-

tion of the Sun, ARA&A, 47, 481–522

Battisti, A. J., Calzetti, D., Johnson, B. D., & Elbaz, D. 2015, Continuous Mid-Infrared Star Formation Rate Indicators: Diagnostics for $0 < z < 3$ Star-Forming Galaxies, ApJ, 800, 143

Beers, T. C., Flynn, K., & Gebhardt, K. 1990, Measures of Location and Scale for Velocities in Clusters of Galaxies - A Robust Approach, AJ, 100, 32–46

Bell, E. F. 2003, Estimating Star Formation Rates from Infrared and Radio Luminosities: The Origin of the Radio-Infrared Correlation, ApJ, 586, 794–813

Bell, E. F., Papovich, C., Wolf, C., Le Floc'h, E., Caldwell, J. A. R., Barden, M., Egami, E., McIntosh, D. H., Meisenheimer, K., Pérez-González, P. G., Rieke, G. H., Rieke, M. J., Rigby, J. R., & Rix, H.-W. 2005, Toward an Understanding of the Rapid Decline of the Cosmic Star Formation Rate, ApJ, 625, 23–36

Bell, E. F., van der Wel, A., Papovich, C., Kocevski, D., Lotz, J., McIntosh, D. H., Kartaltepe, J., Faber, S. M., Ferguson, H., Koekemoer, A., Grogin, N., Wuyts, S., Cheung, E., Conselice, C. J., Dekel, A., Dunlop, J. S., Giavalisco, M., Herrington, J., Koo, D. C., McGrath, E. J., de Mello, D., Rix, H.-W., Robaina, A. R., & Williams, C. C. 2012, What Turns Galaxies Off? The Different Morphologies of Star-forming and Quiescent Galaxies since $z \sim 2$ from CANDELS, ApJ, 753, 167

Bell, E. F., Wolf, C., Meisenheimer, K., Rix, H.-W., Borch, A., Dye, S., Kleinheinrich, M., Wisotzki, L., & McIntosh, D. H. 2004, Nearly 5000 Distant Early-Type Galaxies in COMBO-17: A Red Sequence and Its Evolution since $z \sim 1$, ApJ, 608, 752–767

Blanton, M. R., Hogg, D. W., Bahcall, N. A., Baldry, I. K., Brinkmann, J., Csabai, I., Eisenstein, D., Fukugita, M., Gunn, J. E., Ivezić, Ž., Lamb, D. Q., Lupton, R. H., Loveday, J., Munn, J. A., Nichol, R. C., Okamura, S., Schlegel, D. J., Shimasaku, K., Strauss, M. A., Vogeley, M. S., & Weinberg, D. H. 2003, The

Broadband Optical Properties of Galaxies with Redshifts 0.02<z<0.22, ApJ, 594, 186–207

Brandl, B. R., Bernard-Salas, J., Spoon, H. W. W., Devost, D., Sloan, G. C., Guilles, S., Wu, Y., Houck, J. R., Weedman, D. W., Armus, L., Appleton, P. N., Soifer, B. T., Charmandaris, V., Hao, L., Higdon, J. A., Marshall, S. J., & Herter, T. L. 2006, The Mid-Infrared Properties of Starburst Galaxies from Spitzer-IRS Spectroscopy, ApJ, 653, 1129–1144

Brinchmann, J., Charlot, S., White, S. D. M., Tremonti, C., Kauffmann, G., Heckman, T., & Brinkmann, J. 2004, The Physical Properties of Star-forming Galaxies in the Low-redshift Universe, MNRAS, 351, 1151–1179

Brown, M. J. I., Moustakas, J., Smith, J.-D. T., da Cunha, E., Jarrett, T. H., Imanishi, M., Armus, L., Brandl, B. R., & Peek, J. E. G. 2014, An Atlas of Galaxy Spectral Energy Distributions from the Ultraviolet to the Mid-infrared, ApJS, 212, 18

Bundy, K., Georgakakis, A., Nandra, K., Ellis, R. S., Conselice, C. J., Laird, E., Coil, A., Cooper, M. C., Faber, S. M., Newman, J. A., Pierce, C. M., Primack, J. R., & Yan, R. 2008, AEGIS: New Evidence Linking Active Galactic Nuclei to the Quenching of Star Formation, ApJ, 681, 931–943

Calzetti, D., Kennicutt, R. C., Engelbracht, C. W., Leitherer, C., Draine, B. T., Kewley, L., Moustakas, J., Sosey, M., Dale, D. A., Gordon, K. D., Helou, G. X., Hollenbach, D. J., Armus, L., Bendo, G., Bot, C., Buckalew, B., Jarrett, T., Li, A., Meyer, M., Murphy, E. J., Prescott, M., Regan, M. W., Rieke, G. H., Roussel, H., Sheth, K., Smith, J. D. T., Thornley, M. D., & Walter, F. 2007, The Calibration of Mid-Infrared Star Formation Rate Indicators, ApJ, 666, 870–895

Chabrier, G. 2003, Galactic Stellar and Substellar Initial Mass Function, PASP, 115, 763–795

Chary, R. & Elbaz, D. 2001, Interpreting the Cosmic Infrared Background: Constraints on the Evolution of the Dust-enshrouded Star Formation Rate, ApJ, 556, 562–581

Chen, Y., Lowenthal, J. D., & Yun, M. S. 2010, Color-Magnitude Relation and Morphology of Low-Redshift ULIRGs in Sloan Digital Sky Survey, ApJ, 712, 1385–1402

Cutri, R. M., Nelson, B. O., Kirkpatrick, J. D., Huchra, J. P., & Smith, P. S. 2001, in Astronomical Society of the Pacific Conference Series, Vol. 232, The New Era of Wide Field Astronomy, ed. R. Clowes, A. Adamson, & G. Bromage, 78

Dale, D. A. & Helou, G. 2002, The Infrared Spectral Energy Distribution of Normal Star-forming Galaxies: Calibration at Far-Infrared and Submillimeter Wavelengths, ApJ, 576, 159–168

Dey, A., Jannuzi, B. T., Brown, M. J. I., Tiede, G. P., Stern, D., Dawson, S., Spinrad, H., & NDWFS Team. 2004, in Bulletin of the American Astronomical Society, Vol. 36, American Astronomical Society Meeting Abstracts #204, 746

Diamond-Stanic, A. M. & Rieke, G. H. 2010, The Effect of Active Galactic Nuclei on the Mid-infrared Aromatic Features, ApJ, 724, 140–153

Diamond-Stanic, A. M. & Rieke, G. H. 2012, The Relationship between Black Hole Growth and Star Formation in Seyfert Galaxies, ApJ, 746, 168

Diamond-Stanic, A. M., Rieke, G. H., & Rigby, J. R. 2009, Isotropic Luminosity Indicators in a Complete AGN Sample, ApJ, 698, 623–631

Donley, J. L., Koekemoer, A. M., Brusa, M., Capak, P., Cardamone, C. N., Civano, F., Ilbert, O., Impey, C. D., Kartaltepe, J. S., Miyaji, T., Salvato, M., Sanders, D. B., Trump, J. R., & Zamorani, G. 2012, Identifying Luminous Active Galactic Nuclei in Deep Surveys: Revised IRAC Selection Criteria, ApJ, 748, 142

Donley, J. L., Rieke, G. H., Pérez-González, P. G., & Barro, G. 2008, Spitzer's

Contribution to the AGN Population, ApJ, 687, 111–132

Dopita, M. A. & Sutherland, R. S. 1995, Spectral Signatures of Fast Shocks. II. Optical Diagnostic Diagrams, ApJ, 455, 468

Draine, B. T. & Li, A. 2001, Infrared Emission from Interstellar Dust. I. Stochastic Heating of Small Grains, ApJ, 551, 807–824

Elbaz, D., Dickinson, M., Hwang, H. S., Díaz-Santos, T., Magdis, G., Magnelli, B., Le Borgne, D., Galliano, F., Pannella, M., Chanial, P., Armus, L., Charmandaris, V., Daddi, E., Aussel, H., Popesso, P., Kartaltepe, J., Altieri, B., Valtchanov, I., Coia, D., Dannerbauer, H., Dasyra, K., Leiton, R., Mazzarella, J., Alexander, D. M., Buat, V., Burgarella, D., Chary, R.-R., Gilli, R., Ivison, R. J., Juneau, S., Le Floc'h, E., Lutz, D., Morrison, G. E., Mullaney, J. R., Murphy, E., Pope, A., Scott, D., Brodwin, M., Calzetti, D., Cesarsky, C., Charlot, S., Dole, H., Eisenhardt, P., Ferguson, H. C., Förster Schreiber, N., Frayer, D., Giavalisco, M., Huynh, M., Koekemoer, A. M., Papovich, C., Reddy, N., Surace, C., Teplitz, H., Yun, M. S., & Wilson, G. 2011, GOODS-Herschel: an Infrared Main Sequence for Star-forming Galaxies, A&A, 533, A119

Ellis, R. S. 1997, Faint Blue Galaxies, ARA&A, 35, 389–443

Engelbracht, C. W., Gordon, K. D., Rieke, G. H., Werner, M. W., Dale, D. A., & Latter, W. B. 2005, Metallicity Effects on Mid-Infrared Colors and the 8 μm PAH Emission in Galaxies, ApJ, 628, L29–L32

Erb, D. K., Steidel, C. C., Trainor, R. F., Bogosavljević, M., Shapley, A. E., Nestor, D. B., Kulas, K. R., Law, D. R., Strom, A. L., Rudie, G. C., Reddy, N. A., Pettini, M., Konidaris, N. P., Mace, G., Matthews, K., & McLean, I. S. 2014, The Lyα Properties of Faint Galaxies at z $\sim$ 2-3 with Systemic Redshifts and Velocity Dispersions from Keck-MOSFIRE, ApJ, 795, 33

Faber, S. M., Willmer, C. N. A., Wolf, C., Koo, D. C., Weiner, B. J., Newman,

J. A., Im, M., Coil, A. L., Conroy, C., Cooper, M. C., Davis, M., Finkbeiner, D. P., Gerke, B. F., Gebhardt, K., Groth, E. J., Guhathakurta, P., Harker, J., Kaiser, N., Kassin, S., Kleinheinrich, M., Konidaris, N. P., Kron, R. G., Lin, L., Luppino, G., Madgwick, D. S., Meisenheimer, K., Noeske, K. G., Phillips, A. C., Sarajedini, V. L., Schiavon, R. P., Simard, L., Szalay, A. S., Vogt, N. P., & Yan, R. 2007, Galaxy Luminosity Functions to z∼1 from DEEP2 and COMBO-17: Implications for Red Galaxy Formation, ApJ, 665, 265–294

Farrah, D., Bernard-Salas, J., Spoon, H. W. W., Soifer, B. T., Armus, L., Brandl, B., Charmandaris, V., Desai, V., Higdon, S., Devost, D., & Houck, J. 2007, High-Resolution Mid-Infrared Spectroscopy of Ultraluminous Infrared Galaxies, ApJ, 667, 149–169

Farrah, D., Weedman, D., Lonsdale, C. J., Polletta, M., Rowan-Robinson, M., Houck, J., & Smith, H. E. 2009, Mid-Infrared Spectroscopy of Optically Faint Extragalactic 70 μm Sources, ApJ, 696, 2044–2053

Ferrarese, L. & Merritt, D. 2000, A Fundamental Relation between Supermassive Black Holes and Their Host Galaxies, ApJ, 539, L9–L12

Finkelstein, K. D., Papovich, C., Finkelstein, S. L., Willmer, C. N. A., Rigby, J. R., Rudnick, G., Egami, E., Rieke, M., & Smith, J.-D. T. 2011, Probing the Star Formation History and Initial Mass Function of the z $\sim$ 2.5 Lensed Galaxy SMM J163554.2+661225 with Herschel, ApJ, 742, 108

Finkelstein, S. L., Cohen, S. H., Malhotra, S., Rhoads, J. E., Papovich, C., Zheng, Z. Y., & Wang, J.-X. 2009a, A Plethora of Active Galactic Nuclei Among Lyα Galaxies at Low Redshift, ApJ, 703, L162–L166

Finkelstein, S. L., Papovich, C., Rudnick, G., Egami, E., Le Floc'h, E., Rieke, M. J., Rigby, J. R., & Willmer, C. N. A. 2009b, Turning Back the Clock: Inferring the History of the Eight O'clock Arc, ApJ, 700, 376–386

Franx, M., van Dokkum, P. G., Schreiber, N. M. F., Wuyts, S., Labbé, I., & Toft, S. 2008, Structure and Star Formation in Galaxies out to z = 3: Evidence for Surface Density Dependent Evolution and Upsizing, ApJ, 688, 770–788

Frayer, D. T., Fadda, D., Yan, L., Marleau, F. R., Choi, P. I., Helou, G., Soifer, B. T., Appleton, P. N., Armus, L., Beck, R., Dole, H., Engelbracht, C. W., Fang, F., Gordon, K. D., Heinrichsen, I., Henderson, D., Hesselroth, T., Im, M., Kelly, D. M., Lacy, M., Laine, S., Latter, W. B., Mahoney, W., Makovoz, D., Masci, F. J., Morrison, J. E., Moshir, M., Noriega-Crespo, A., Padgett, D. L., Pesenson, M., Shupe, D. L., Squires, G. K., Storrie-Lombardi, L. J., Surace, J. A., Teplitz, H. I., & Wilson, G. 2006, Spitzer 70 and 160 μm Observations of the Extragalactic First Look Survey, AJ, 131, 250–260

Fu, H. & Stockton, A. 2009, FR II Quasars: Infrared Properties, Star Formation Rates, and Extended Ionized Gas, ApJ, 696, 1693–1699

Fumagalli, M., Labbé, I., Patel, S. G., Franx, M., van Dokkum, P., Brammer, G., da Cunha, E., Förster Schreiber, N. M., Kriek, M., Quadri, R., Rix, H.-W., Wake, D., Whitaker, K. E., Lundgren, B., Marchesini, D., Maseda, M., Momcheva, I., Nelson, E., Pacifici, C., & Skelton, R. E. 2014, How Dead are Dead Galaxies? Mid-infrared Fluxes of Quiescent Galaxies at Redshift $0.3 < z < 2.5$: Implications for Star Formation Rates and Dust Heating, ApJ, 796, 35

Gebhardt, K., Bender, R., Bower, G., Dressler, A., Faber, S. M., Filippenko, A. V., Green, R., Grillmair, C., Ho, L. C., Kormendy, J., Lauer, T. R., Magorrian, J., Pinkney, J., Richstone, D., & Tremaine, S. 2000, A Relationship between Nuclear Black Hole Mass and Galaxy Velocity Dispersion, ApJ, 539, L13–L16

Genzel, R., Lutz, D., Sturm, E., Egami, E., Kunze, D., Moorwood, A. F. M., Rigopoulou, D., Spoon, H. W. W., Sternberg, A., Tacconi-Garman, L. E., Tacconi, L., & Thatte, N. 1998, What Powers Ultraluminous IRAS Galaxies?, ApJ,

498, 579

Goldader, J. D., Goldader, D. L., Joseph, R. D., Doyon, R., & Sanders, D. B. 1997, Heavily Obscured Star Formation in the II ZW 96 Galaxy Merger, AJ, 113, 1569–1579

Goldschmidt, P., Miller, L., La Franca, F., & Cristiani, S. 1992, The High Surface Density of Bright Ultraviolet-excess Quasars, MNRAS, 256, 65P–68P

Gordon, K. D., Engelbracht, C. W., Rieke, G. H., Misselt, K. A., Smith, J.-D. T., & Kennicutt, Jr., R. C. 2008, The Behavior of the Aromatic Features in M101 H II Regions: Evidence for Dust Processing, ApJ, 682, 336–354

Haan, S., Armus, L., Surace, J. A., Charmandaris, V., Evans, A. S., Diaz-Santos, T., Melbourne, J. L., Mazzarella, J. M., Howell, J. H., Stierwalt, S., Kim, D. C., Vavilkin, T., Sanders, D. B., Petric, A., Murphy, E. J., Braun, R., Bridge, C. R., & Inami, H. 2013, The Build-up of Nuclear Stellar Cusps in Extreme Starburst Galaxies and Major Mergers, MNRAS, 434, 1264–1286

Hainline, K. N., Shapley, A. E., Kornei, K. A., Pettini, M., Buckley-Geer, E., Allam, S. S., & Tucker, D. L. 2009, Rest-Frame Optical Spectra of Three Strongly Lensed Galaxies at z $\sim$ 2, ApJ, 701, 52–65

Hernán-Caballero, A., Pérez-Fournon, I., Hatziminaoglou, E., Afonso-Luis, A., Rowan-Robinson, M., Rigopoulou, D., Farrah, D., Lonsdale, C. J., Babbedge, T., Clements, D., Serjeant, S., Pozzi, F., Vaccari, M., Montenegro-Montes, F. M., Valtchanov, I., González-Solares, E., Oliver, S., Shupe, D., Gruppioni, C., Vila-Vilaró, B., Lari, C., & La Franca, F. 2009, Mid-infrared Spectroscopy of Infrared-luminous Galaxies at z $\sim$ 0.5-3, MNRAS, 395, 1695–1722

Ho, L. C. 2005, [O II] Emission in Quasar Host Galaxies: Evidence for a Suppressed Star Formation Efficiency, ApJ, 629, 680–685

Ho, L. C. & Keto, E. 2007, The Mid-Infrared Fine-Structure Lines of Neon as an

Indicator of Star Formation Rate in Galaxies, ApJ, 658, 314–318

Hopkins, P. F., Hernquist, L., Cox, T. J., & Kereš, D. 2008, A Cosmological Framework for the Co-Evolution of Quasars, Supermassive Black Holes, and Elliptical Galaxies. I. Galaxy Mergers and Quasar Activity, ApJS, 175, 356–389

Houck, J. R., Roellig, T. L., van Cleve, J., Forrest, W. J., Herter, T., Lawrence, C. R., Matthews, K., Reitsema, H. J., Soifer, B. T., Watson, D. M., Weedman, D., Huisjen, M., Troeltzsch, J., Barry, D. J., Bernard-Salas, J., Blacken, C. E., Brandl, B. R., Charmandaris, V., Devost, D., Gull, G. E., Hall, P., Henderson, C. P., Higdon, S. J. U., Pirger, B. E., Schoenwald, J., Sloan, G. C., Uchida, K. I., Appleton, P. N., Armus, L., Burgdorf, M. J., Fajardo-Acosta, S. B., Grillmair, C. J., Ingalls, J. G., Morris, P. W., & Teplitz, H. I. 2004, The Infrared Spectrograph (IRS) on the Spitzer Space Telescope, ApJS, 154, 18–24

Houck, J. R., Soifer, B. T., Weedman, D., Higdon, S. J. U., Higdon, J. L., Herter, T., Brown, M. J. I., Dey, A., Jannuzi, B. T., Le Floc'h, E., Rieke, M., Armus, L., Charmandaris, V., Brandl, B. R., & Teplitz, H. I. 2005, Spectroscopic Redshifts to z $>$ 2 for Optically Obscured Sources Discovered with the Spitzer Space Telescope, ApJ, 622, L105–L108

Hubble, E. P. 1926, Extragalactic Nebulae, ApJ, 64, 321–369

Jannuzi, B. T. & Dey, A. 1999, in Astronomical Society of the Pacific Conference Series, Vol. 191, Photometric Redshifts and the Detection of High Redshift Galaxies, ed. R. Weymann, L. Storrie-Lombardi, M. Sawicki, & R. Brunner, 111

Jannuzi, B. T., Dey, A., Brown, M. J. I., Ford, A., Hogan, E., Miller, M., Ryan, E., Tiede, G. P., Valdes, F., & NDWFS Team. 2004, in Bulletin of the American Astronomical Society, Vol. 36, American Astronomical Society Meeting Abstracts, 1478

Jester, S., Schneider, D. P., Richards, G. T., Green, R. F., Schmidt, M., Hall, P. B.,

Strauss, M. A., Vanden Berk, D. E., Stoughton, C., Gunn, J. E., Brinkmann, J., Kent, S. M., Smith, J. A., Tucker, D. L., & Yanny, B. 2005, The Sloan Digital Sky Survey View of the Palomar-Green Bright Quasar Survey, AJ, 130, 873–895

Kauffmann, G., Heckman, T. M., Tremonti, C., Brinchmann, J., Charlot, S., White, S. D. M., Ridgway, S. E., Brinkmann, J., Fukugita, M., Hall, P. B., Ivezić, Ž., Richards, G. T., & Schneider, D. P. 2003, The Host Galaxies of Active Galactic Nuclei, MNRAS, 346, 1055–1077

Kennicutt, R. C. & Evans, N. J. 2012, Star Formation in the Milky Way and Nearby Galaxies, ARA&A, 50, 531–608

Kennicutt, Jr., R. C. 1998, Star Formation in Galaxies Along the Hubble Sequence, ARA&A, 36, 189–232

Kennicutt, Jr., R. C., Calzetti, D., Walter, F., Helou, G., Hollenbach, D. J., Armus, L., Bendo, G., Dale, D. A., Draine, B. T., Engelbracht, C. W., Gordon, K. D., Prescott, M. K. M., Regan, M. W., Thornley, M. D., Bot, C., Brinks, E., de Blok, E., de Mello, D., Meyer, M., Moustakas, J., Murphy, E. J., Sheth, K., & Smith, J. D. T. 2007, Star Formation in NGC 5194 (M51a). II. The Spatially Resolved Star Formation Law, ApJ, 671, 333–348

Kennicutt, Jr., R. C., Hao, C.-N., Calzetti, D., Moustakas, J., Dale, D. A., Bendo, G., Engelbracht, C. W., Johnson, B. D., & Lee, J. C. 2009, Dust-corrected Star Formation Rates of Galaxies. I. Combinations of Hα and Infrared Tracers, ApJ, 703, 1672–1695

Kewley, L. J., Dopita, M. A., Sutherland, R. S., Heisler, C. A., & Trevena, J. 2001, Theoretical Modeling of Starburst Galaxies, ApJ, 556, 121–140

Kirkpatrick, A., Pope, A., Alexander, D. M., Charmandaris, V., Daddi, E., Dickinson, M., Elbaz, D., Gabor, J., Hwang, H. S., Ivison, R., Mullaney, J., Pannella, M., Scott, D., Altieri, B., Aussel, H., Bournaud, F., Buat, V., Coia, D., Danner-

bauer, H., Dasyra, K., Kartaltepe, J., Leiton, R., Lin, L., Magdis, G., Magnelli, B., Morrison, G., Popesso, P., & Valtchanov, I. 2012, GOODS-Herschel: Impact of Active Galactic Nuclei and Star Formation Activity on Infrared Spectral Energy Distributions at High Redshift, ApJ, 759, 139

Kochanek, C. S., Eisenstein, D. J., Cool, R. J., Caldwell, N., Assef, R. J., Jannuzi, B. T., Jones, C., Murray, S. S., Forman, W. R., Dey, A., Brown, M. J. I., Eisenhardt, P., Gonzalez, A. H., Green, P., & Stern, D. 2012, AGES: The AGN and Galaxy Evolution Survey, ApJS, 200, 8

Kormendy, J. & Ho, L. C. 2013, Coevolution (Or Not) of Supermassive Black Holes and Host Galaxies, ARA&A, 51, 511–653

Kroupa, P. & Weidner, C. 2003, Galactic-Field Initial Mass Functions of Massive Stars, ApJ, 598, 1076–1078

Lacy, M., Wilson, G., Masci, F., Storrie-Lombardi, L. J., Appleton, P. N., Armus, L., Chapman, S. C., Choi, P. I., Fadda, D., Fang, F., Frayer, D. T., Heinrichsen, I., Helou, G., Im, M., Laine, S., Marleau, F. R., Shupe, D. L., Soifer, B. T., Squires, G. K., Surace, J., Teplitz, H. I., & Yan, L. 2005, The Infrared Array Camera Component of the Spitzer Space Telescope Extragalactic First Look Survey, ApJS, 161, 41–52

Laurent, O., Mirabel, I. F., Charmandaris, V., Gallais, P., Madden, S. C., Sauvage, M., Vigroux, L., & Cesarsky, C. 2000, Mid-infrared Diagnostics to Distinguish AGNs from Starbursts, A&A, 359, 887–899

Le Floc'h, E., Papovich, C., Dole, H., Bell, E. F., Lagache, G., Rieke, G. H., Egami, E., Pérez-González, P. G., Alonso-Herrero, A., Rieke, M. J., Blaylock, M., Engelbracht, C. W., Gordon, K. D., Hines, D. C., Misselt, K. A., Morrison, J. E., & Mould, J. 2005, Infrared Luminosity Functions from the Chandra Deep Field-South: The Spitzer View on the History of Dusty Star Formation at 0 $<\sim$ z $<\sim$

1, ApJ, 632, 169–190

Leger, A. & Puget, J. L. 1984, Identification of the 'Unidentified' IR Emission Features of Interstellar Dust?, A&A, 137, L5–L8

Lei, X., Rieke, G. H., Egami, E., Haines, C. P., Pereira, M. J., & Smith, G. P. 2015, The Relation between Luminous AGNs and Star Formation in Their Host Galaxies, ApJ, in preparation

Lin, H., Buckley-Geer, E., Allam, S. S., Tucker, D. L., Diehl, H. T., Kubik, D., Kubo, J. M., Annis, J., Frieman, J. A., Oguri, M., & Inada, N. 2009, Discovery of a Very Bright, Strongly Lensed z = 2 Galaxy in the SDSS DR5, ApJ, 699, 1242–1251

Lutz, D. 2014, Far-Infrared Surveys of Galaxy Evolution, ARA&A, 52, 373–414

Lutz, D., Sturm, E., Tacconi, L. J., Valiante, E., Schweitzer, M., Netzer, H., Maiolino, R., Andreani, P., Shemmer, O., & Veilleux, S. 2008, Star Formation in the Hosts of High-z QSOs: Evidence from Spitzer PAH Detections, ApJ, 684, 853–861

Madau, P. & Dickinson, M. 2014, Cosmic Star-Formation History, ARA&A, 52, 415–486

Magnelli, B., Elbaz, D., Chary, R. R., Dickinson, M., Le Borgne, D., Frayer, D. T., & Willmer, C. N. A. 2009, The $0.4 < z < 1.3$ Star Formation History of the Universe as Viewed in the Far-infrared, A&A, 496, 57–75

Meléndez, M., Kraemer, S. B., Armentrout, B. K., Deo, R. P., Crenshaw, D. M., Schmitt, H. R., Mushotzky, R. F., Tueller, J., Markwardt, C. B., & Winter, L. 2008, New Indicators for AGN Power: The Correlation between [O IV] 25.89 μm and Hard X-Ray Luminosity for Nearby Seyfert Galaxies, ApJ, 682, 94–103

Mendez, A. J., Coil, A. L., Aird, J., Diamond-Stanic, A. M., Moustakas, J., Blanton, M. R., Cool, R. J., Eisenstein, D. J., Wong, K. C., & Zhu, G. 2013, PRIMUS: Infrared and X-ray AGN Selection Techniques at $0.2<z<1.2$, ArXiv e-prints

Murphy, E. J., Chary, R.-R., Dickinson, M., Pope, A., Frayer, D. T., & Lin, L. 2011, An Accounting of the Dust-obscured Star Formation and Accretion Histories Over the Last ∼11 Billion Years, ApJ, 732, 126

Nandra, K., Georgakakis, A., Willmer, C. N. A., Cooper, M. C., Croton, D. J., Davis, M., Faber, S. M., Koo, D. C., Laird, E. S., & Newman, J. A. 2007, AEGIS: The Color-Magnitude Relation for X-Ray-selected Active Galactic Nuclei, ApJ, 660, L11–L14

Netzer, H. 2009, Accretion and Star Formation Rates in Low-redshift Type II Active Galactic Nuclei, MNRAS, 399, 1907–1920

O'Dowd, M. J., Schiminovich, D., Johnson, B. D., Treyer, M. A., Martin, C. D., Wyder, T. K., Charlot, S., Heckman, T. M., Martins, L. P., Seibert, M., & van der Hulst, J. M. 2009, Polycyclic Aromatic Hydrocarbons in Galaxies at z $\sim$ 0.1: The Effect of Star Formation and Active Galactic Nuclei, ApJ, 705, 885–898

Oke, J. B. & Gunn, J. E. 1983, Secondary Standard Stars for Absolute Spectrophotometry, ApJ, 266, 713–717

Osterbrock, D. E. 1989, Astrophysics of gaseous nebulae and active galactic nuclei (University Science Books), 84

Papovich, C., Bassett, R., Lotz, J. M., van der Wel, A., Tran, K.-V., Finkelstein, S. L., Bell, E. F., Conselice, C. J., Dekel, A., Dunlop, J. S., Guo, Y., Faber, S. M., Farrah, D., Ferguson, H. C., Finkelstein, K. D., Häussler, B., Kocevski, D. D., Koekemoer, A. M., Koo, D. C., McGrath, E. J., McLure, R. J., McIntosh, D. H., Momcheva, I., Newman, J. A., Rudnick, G., Weiner, B., Willmer, C. N. A., & Wuyts, S. 2012, CANDELS Observations of the Structural Properties of Cluster Galaxies at z = 1.62, ApJ, 750, 93

Papovich, C. & Bell, E. F. 2002, On Measuring the Infrared Luminosity of Distant Galaxies with the Space Infrared Telescope Facility, ApJ, 579, L1–L4

Papovich, C., Cool, R., Eisenstein, D., Le Floc'h, E., Fan, X., Kennicutt, Jr., R. C., Smith, J. D. T., Rieke, G. H., & Vestergaard, M. 2006, An MMT Hectospec Redshift Survey of 24 μm Sources in the Spitzer First Look Survey, AJ, 132, 231–241

Papovich, C., Rudnick, G., Rigby, J. R., Willmer, C. N. A., Smith, J.-D. T., Finkelstein, S. L., Egami, E., & Rieke, M. 2009, Paschen-α Emission in the Gravitationally Lensed Galaxy SMM J163554.2+661225, ApJ, 704, 1506–1518

Pérez-González, P. G., Rieke, G. H., Egami, E., Alonso-Herrero, A., Dole, H., Papovich, C., Blaylock, M., Jones, J., Rieke, M., Rigby, J., Barmby, P., Fazio, G. G., Huang, J., & Martin, C. 2005, Spitzer View on the Evolution of Star-forming Galaxies from z = 0 to z $\sim$ 3, ApJ, 630, 82–107

Petric, A. O., Armus, L., Howell, J., Chan, B., Mazzarella, J. M., Evans, A. S., Surace, J. A., Sanders, D., Appleton, P., Charmandaris, V., Díaz-Santos, T., Frayer, D., Haan, S., Inami, H., Iwasawa, K., Kim, D., Madore, B., Marshall, J., Spoon, H., Stierwalt, S., Sturm, E., U, V., Vavilkin, T., & Veilleux, S. 2011, Mid-Infrared Spectral Diagnostics of Luminous Infrared Galaxies, ApJ, 730, 28

Pettini, M. & Pagel, B. E. J. 2004, [OIII]/[NII] as an Abundance Indicator at High Redshift, MNRAS, 348, L59–L63

Pope, A., Chary, R.-R., Alexander, D. M., Armus, L., Dickinson, M., Elbaz, D., Frayer, D., Scott, D., & Teplitz, H. 2008, Mid-Infrared Spectral Diagnosis of Submillimeter Galaxies, ApJ, 675, 1171–1193

Rieke, G. H., Alonso-Herrero, A., Weiner, B. J., Pérez-González, P. G., Blaylock, M., Donley, J. L., & Marcillac, D. 2009, Determining Star Formation Rates for Infrared Galaxies, ApJ, 692, 556–573

Rigby, J. R., Diamond-Stanic, A. M., & Aniano, G. 2009, Calibration Of [O IV] 26 μm as a Measure of Intrinsic Active Galactic Nucleus Luminosity, ApJ, 700,

1878–1883

Rigby, J. R., Marcillac, D., Egami, E., Rieke, G. H., Richard, J., Kneib, J.-P., Fadda, D., Willmer, C. N. A., Borys, C., van der Werf, P. P., Pérez-González, P. G., Knudsen, K. K., & Papovich, C. 2008, Mid-Infrared Spectroscopy of Lensed Galaxies at $1 < z < 3$: The Nature of Sources Near the MIPS Confusion Limit, ApJ, 675, 262–280

Rigopoulou, D., Spoon, H. W. W., Genzel, R., Lutz, D., Moorwood, A. F. M., & Tran, Q. D. 1999, A Large Mid-Infrared Spectroscopic and Near-Infrared Imaging Survey of Ultraluminous Infrared Galaxies: Their Nature and Evolution, AJ, 118, 2625–2645

Roussel, H., Helou, G., Hollenbach, D. J., Draine, B. T., Smith, J. D., Armus, L., Schinnerer, E., Walter, F., Engelbracht, C. W., Thornley, M. D., Kennicutt, R. C., Calzetti, D., Dale, D. A., Murphy, E. J., & Bot, C. 2007, Warm Molecular Hydrogen in the Spitzer SINGS Galaxy Sample, ApJ, 669, 959–981

Rujopakarn, W., Rieke, G. H., Papovich, C. J., Weiner, B. J., Rigby, J. R., Rex, M., Bian, F., Kuhn, O. P., & Thompson, D. 2012, Large Binocular Telescope and Spitzer Spectroscopy of Star-forming Galaxies at $1 < z < 3$: Extinction and Star Formation Rate Indicators, ApJ, 755, 168

Sanders, D. B. & Mirabel, I. F. 1996, Luminous Infrared Galaxies, ARA&A, 34, 749

Sargsyan, L. A. & Weedman, D. W. 2009, Star Formation Rates for Starburst Galaxies from Ultraviolet, Infrared, and Radio Luminosities, ApJ, 701, 1398–1414

Schawinski, K., Thomas, D., Sarzi, M., Maraston, C., Kaviraj, S., Joo, S.-J., Yi, S. K., & Silk, J. 2007, Observational Evidence for AGN Feedback in Early-type Galaxies, MNRAS, 382, 1415–1431

Schawinski, K., Urry, C. M., Virani, S., Coppi, P., Bamford, S. P., Treister, E., Lintott, C. J., Sarzi, M., Keel, W. C., Kaviraj, S., Cardamone, C. N., Masters,

K. L., Ross, N. P., Andreescu, D., Murray, P., Nichol, R. C., Raddick, M. J., Slosar, A., Szalay, A. S., Thomas, D., & Vandenberg, J. 2010, Galaxy Zoo: The Fundamentally Different Co-Evolution of Supermassive Black Holes and Their Early- and Late-Type Host Galaxies, ApJ, 711, 284–302

Schutte, W. A., Tielens, A. G. G. M., & Allamandola, L. J. 1993, Theoretical Modeling of the Infrared Fluorescence from Interstellar Polycyclic Aromatic Hydrocarbons, ApJ, 415, 397–414

Schweitzer, M., Lutz, D., Sturm, E., Contursi, A., Tacconi, L. J., Lehnert, M. D., Dasyra, K. M., Genzel, R., Veilleux, S., Rupke, D., Kim, D.-C., Baker, A. J., Netzer, H., Sternberg, A., Mazzarella, J., & Lord, S. 2006, Spitzer Quasar and ULIRG Evolution Study (QUEST). I. The Origin of the Far-Infrared Continuum of QSOs, ApJ, 649, 79–90

Seitz, S., Saglia, R. P., Bender, R., Hopp, U., Belloni, P., & Ziegler, B. 1998, The z=2.72 Galaxy cB58: a Gravitational Fold Arc Lensed by the Cluster MS1512+36, MNRAS, 298, 945–965

Shang, Z., Brotherton, M. S., Wills, B. J., Wills, D., Cales, S. L., Dale, D. A., Green, R. F., Runnoe, J. C., Nemmen, R. S., Gallagher, S. C., Ganguly, R., Hines, D. C., Kelly, B. J., Kriss, G. A., Li, J., Tang, B., & Xie, Y. 2011, The Next Generation Atlas of Quasar Spectral Energy Distributions from Radio to X-Rays, ApJS, 196, 2

Shao, L., Lutz, D., Nordon, R., Maiolino, R., Alexander, D. M., Altieri, B., Andreani, P., Aussel, H., Bauer, F. E., Berta, S., Bongiovanni, A., Brandt, W. N., Brusa, M., Cava, A., Cepa, J., Cimatti, A., Daddi, E., Dominguez-Sanchez, H., Elbaz, D., Förster Schreiber, N. M., Geis, N., Genzel, R., Grazian, A., Gruppioni, C., Magdis, G., Magnelli, B., Mainieri, V., Pérez García, A. M., Poglitsch, A., Popesso, P., Pozzi, F., Riguccini, L., Rodighiero, G., Rovilos, E., Saintonge,

A., Salvato, M., Sanchez Portal, M., Santini, P., Sturm, E., Tacconi, L. J., Valtchanov, I., Wetzstein, M., & Wieprecht, E. 2010, Star Formation in AGN Hosts in GOODS-N, A&A, 518, L26

Shi, Y., Rieke, G. H., Ogle, P. M., Su, K. Y. L., & Balog, Z. 2014, Infrared Spectra and Photometry Of Complete Samples of Palomar-Green and Two Micron All Sky Survey Quasars, ApJS, 214, 23

Shipley, H. V., Papovich, C., Brown, M. J., Moustakas, J., & Rieke, G. H. 2015, A New Star-formation Rate Calibration from Polycyclic Aromatic Hydrocarbon Emission Features: Application to High Redshift Galaxies, ApJ, submitted

Shipley, H. V., Papovich, C., Rieke, G. H., Dey, A., Jannuzi, B. T., Moustakas, J., & Weiner, B. 2013, Spitzer Spectroscopy of Infrared-luminous Galaxies: Diagnostics of Active Galactic Nuclei and Star Formation and Contribution to Total Infrared Luminosity, ApJ, 769, 75

Siana, B., Teplitz, H. I., Chary, R.-R., Colbert, J., & Frayer, D. T. 2008, Spitzer Observations of the z = 2.73 Lensed Lyman Break Galaxy: MS 1512-cB58, ApJ, 689, 59–67

Smail, I., Smith, G. P., & Ivison, R. J. 2005, The Intrinsic Properties of SMM J14011+0252, ApJ, 631, 121–125

Smith, J. D. T., Draine, B. T., Dale, D. A., Moustakas, J., Kennicutt, Jr., R. C., Helou, G., Armus, L., Roussel, H., Sheth, K., Bendo, G. J., Buckalew, B. A., Calzetti, D., Engelbracht, C. W., Gordon, K. D., Hollenbach, D. J., Li, A., Malhotra, S., Murphy, E. J., & Walter, F. 2007, The Mid-Infrared Spectrum of Star-forming Galaxies: Global Properties of Polycyclic Aromatic Hydrocarbon Emission, ApJ, 656, 770–791

Smith, P. S., Schmidt, G. D., Hines, D. C., Cutri, R. M., & Nelson, B. O. 2002, The Optical Polarization of Near-Infrared-selected Quasi-Stellar Objects, ApJ, 569,

23–35

Somerville, R. S., Gilmore, R. C., Primack, J. R., & Domínguez, A. 2012, Galaxy Properties from the Ultraviolet to the Far-infrared: Λ Cold Dark Matter Models Confront Observations, MNRAS, 423, 1992–2015

Spoon, H. W. W., Marshall, J. A., Houck, J. R., Elitzur, M., Hao, L., Armus, L., Brandl, B. R., & Charmandaris, V. 2007, Mid-Infrared Galaxy Classification Based on Silicate Obscuration and PAH Equivalent Width, ApJ, 654, L49–L52

Springel, V., Di Matteo, T., & Hernquist, L. 2005, Modeling Feedback from Stars and Black Holes in Galaxy Mergers, MNRAS, 361, 776–794

Steidel, C. C., Giavalisco, M., Pettini, M., Dickinson, M., & Adelberger, K. L. 1996, Spectroscopic Confirmation of a Population of Normal Star-forming Galaxies at Redshifts Z > 3, ApJ, 462, L17

Stern, D., Eisenhardt, P., Gorjian, V., Kochanek, C. S., Caldwell, N., Eisenstein, D., Brodwin, M., Brown, M. J. I., Cool, R., Dey, A., Green, P., Jannuzi, B. T., Murray, S. S., Pahre, M. A., & Willner, S. P. 2005, Mid-Infrared Selection of Active Galaxies, ApJ, 631, 163–168

Teplitz, H. I., McLean, I. S., Becklin, E. E., Figer, D. F., Gilbert, A. M., Graham, J. R., Larkin, J. E., Levenson, N. A., & Wilcox, M. K. 2000, The Rest-Frame Optical Spectrum of MS 1512-CB58, ApJ, 533, L65–L68

Tielens, A. G. G. M. 2005, The Physics and Chemistry of the Interstellar Medium (Cambridge University Press)

Tinsley, B. M. 1968, Evolution of the Stars and Gas in Galaxies, ApJ, 151, 547

Tran, Q. D., Lutz, D., Genzel, R., Rigopoulou, D., Spoon, H. W. W., Sturm, E., Gerin, M., Hines, D. C., Moorwood, A. F. M., Sanders, D. B., Scoville, N., Taniguchi, Y., & Ward, M. 2001, Isocam-Cvf 5-12 Micron Spectroscopy of Ultraluminous Infrared Galaxies, ApJ, 552, 527–543

Tremonti, C. A., Heckman, T. M., Kauffmann, G., Brinchmann, J., Charlot, S., White, S. D. M., Seibert, M., Peng, E. W., Schlegel, D. J., Uomoto, A., Fukugita, M., & Brinkmann, J. 2004, The Origin of the Mass-Metallicity Relation: Insights from 53,000 Star-forming Galaxies in the Sloan Digital Sky Survey, ApJ, 613, 898–913

Treyer, M., Schiminovich, D., Johnson, B. D., O'Dowd, M., Martin, C. D., Wyder, T., Charlot, S., Heckman, T., Martins, L., Seibert, M., & van der Hulst, J. M. 2010, Mid-infrared Spectral Indicators of Star Formation and Active Galactic Nucleus Activity in Normal Galaxies, ApJ, 719, 1191–1211

Van Dokkum, P. G., Kriek, M., Rodgers, B., Franx, M., & Puxley, P. 2005, Gemini Near-Infrared Spectrograph Observations of a Red Star-forming Galaxy at z=2.225: Evidence of Shock Ionization Due to a Galactic Wind, ApJ, 622, L13–L16

Veilleux, S., Rupke, D. S. N., Kim, D.-C., Genzel, R., Sturm, E., Lutz, D., Contursi, A., Schweitzer, M., Tacconi, L. J., Netzer, H., Sternberg, A., Mihos, J. C., Baker, A. J., Mazzarella, J. M., Lord, S., Sanders, D. B., Stockton, A., Joseph, R. D., & Barnes, J. E. 2009, Spitzer Quasar and ULIRG Evolution Study (QUEST). IV. Comparison of 1 Jy Ultraluminous Infrared Galaxies with Palomar-Green Quasars, ApJS, 182, 628–666

Volino, F., Wucknitz, O., McKean, J. P., & Garrett, M. A. 2010, Very Large Array Observations of the 8 O'clock Arc Lens System: Radio Emission and a Limit on the Star-formation Rate, A&A, 524, A79

Weedman, D., Polletta, M., Lonsdale, C. J., Wilkes, B. J., Siana, B., Houck, J. R., Surace, J., Shupe, D., Farrah, D., & Smith, H. E. 2006, Active Galactic Nucleus and Starburst Classification from Spitzer Mid-Infrared Spectra for High-Redshift SWIRE Sources, ApJ, 653, 101–111

Weiner, B. J., Papovich, C., Bundy, K., Conselice, C. J., Cooper, M. C., Ellis, R. S., Ivison, R. J., Noeske, K. G., Phillips, A. C., & Yan, R. 2007, AEGIS: Extinction and Star Formation Tracers from Line Emission, ApJ, 660, L39–L42

Wu, Y., Helou, G., Armus, L., Cormier, D., Shi, Y., Dale, D., Dasyra, K., Smith, J. D., Papovich, C., Draine, B., Rahman, N., Stierwalt, S., Fadda, D., Lagache, G., & Wright, E. L. 2010, Infrared Luminosities and Aromatic Features in the 24 μm Flux-limited Sample of 5MUSES, ApJ, 723, 895–914

Wuyts, E., Rigby, J. R., Gladders, M. D., Gilbank, D. G., Sharon, K., Gralla, M. B., & Bayliss, M. B. 2012, Stellar Populations of Highly Magnified Lensed Galaxies: Young Starbursts at z $\sim$ 2, ApJ, 745, 86

Wuyts, S., Förster Schreiber, N. M., van der Wel, A., Magnelli, B., Guo, Y., Genzel, R., Lutz, D., Aussel, H., Barro, G., Berta, S., Cava, A., Graciá-Carpio, J., Hathi, N. P., Huang, K.-H., Kocevski, D. D., Koekemoer, A. M., Lee, K.-S., Le Floc'h, E., McGrath, E. J., Nordon, R., Popesso, P., Pozzi, F., Riguccini, L., Rodighiero, G., Saintonge, A., & Tacconi, L. 2011, Galaxy Structure and Mode of Star Formation in the SFR-Mass Plane from z $\sim$ 2.5 to z $\sim$ 0.1, ApJ, 742, 96

Wyder, T. K., Martin, D. C., Schiminovich, D., Seibert, M., Budavári, T., Treyer, M. A., Barlow, T. A., Forster, K., Friedman, P. G., Morrissey, P., Neff, S. G., Small, T., Bianchi, L., Donas, J., Heckman, T. M., Lee, Y.-W., Madore, B. F., Milliard, B., Rich, R. M., Szalay, A. S., Welsh, B. Y., & Yi, S. K. 2007, The UV-Optical Galaxy Color-Magnitude Diagram. I. Basic Properties, ApJS, 173, 293–314

Yan, L., Chary, R., Armus, L., Teplitz, H., Helou, G., Frayer, D., Fadda, D., Surace, J., & Choi, P. 2005, Spitzer Detection of Polycyclic Aromatic Hydrocarbon and Silicate Dust Features in the Mid-Infrared Spectra of z $\sim$ 2 Ultraluminous Infrared Galaxies, ApJ, 628, 604–610

APPENDIX A

ESTIMATING THE TOTAL IR LUMINOSITY

At the redshifts of our sample, $0.02 < z < 0.6$, the MIPS IR data probe the rest-frame mid-to-far-IR, which broadly correlates with the total IR luminosity (e.g. Chary & Elbaz, 2001; Papovich & Bell, 2002; Rieke et al., 2009). We used models (Chary & Elbaz, 2001; Dale & Helou, 2002; Rieke et al., 2009) for the IR SED of galaxies to convert the observed MIPS data to total IR luminosity. By selection, all galaxies in our sample have 24μm detections, and we convert the observed 24μm flux densities to rest-frame luminosity densities at $24\mu\mathrm{m}/(1+z)$. We then correct these values to a total IR luminosity, $\mathrm{L_{IR}}(24\mu\mathrm{m})$, using *each* of the three sets of model IR SEDs, assuming for each set of models that a given rest-frame $24\mu\mathrm{m}/(1+z)$ luminosity density translates uniquely to a single SED template. The Rieke et al. (2009) templates apply to local galaxies and do not include the SED evolution seen at high redshift. However, Rujopakarn et al. (2012) show that the local SEDs and those appropriate for high redshift converge for the redshift range of our sample.

For those galaxies with detections at 70μm and/or 160μm in the MAGES data (as listed in table 2.1), we use all available MIPS flux densities to estimate the total IR luminosity. For each source, we convert the observed MIPS data to rest-frame luminosity densities, and scaled each IR SED in each set of models with a multiplicative factor to obtain a best-fit for each SED. For each set of models, we minimized a χ^2 statistic with $\chi^2_a = \sum(d_i - c \times m_i^a)^2/\sigma_i$, where d_i is the rest-frame luminosity density measured from the i=24μm, 70μm, and 160μm data, $m_{(a,i)}$ is the luminosity density expected for model IR SED a, c is the fitted scale factor, and σ_i are the errors on the measured MIPS data. We chose the IR SED from each set of

models that minimizes χ^2_a.

In figure A.1, we compare the $L_{IR}(24\mu m)$ against the L_{IR} derived using multiple MIPS bands (24μm, 70μm and/or 160μm) for each of the three sets of IR SED models (Chary & Elbaz, 2001; Dale & Helou, 2002; Rieke et al., 2009). We found that there is no more than a factor of 2-3 difference in the derived IR luminosity from multiple MIPS bands and that derived from 24μm only between any of the IR SED models. This is particularly true for galaxies with total IR luminosities $L_{IR} > 10^{11} L_{\odot}$ (the majority of L_{IR} estimates in our sample). However, our far-IR (160μm sources) sample is incomplete in the direction that the less luminous galaxies ($L_{IR} < 10^{11} L_{\odot}$) will be under-represented. As illustrated in figure A.1 and discussed below, the IR luminosities derived from the 24μm data only from the Rieke et al. (2009) SED templates are the most consistent with the IR luminosities derived using multiple MIPS bands. In particular, for IRAGN the IR luminosities derived with the Rieke et al. (2009) SED templates with only 24μm data are consistent with those from multiple MIPS bands. We find the median ratio estimates of the total IR luminosity (using all bands available) compared to the total IR luminosity (using only the 24μm band) for the Chary & Elbaz (2001), Dale & Helou (2002), and Rieke et al. (2009) models to be 0.97, 0.96, and 1.0, respectively.

We considered the idea that the IR SED templates we used for the IRAGN may be incorrect, which could be the case for those IRAGN with only 24μm detections. Specifically, we computed the total IR luminosities from the 24 micron flux densities for the IRAGN using the SEDs for optically luminous quasars (Shang et al., 2011). In these cases the total IR luminosities for the IRAGN would decrease by at most a factor of five (at most a factor of 3.5 for the IRAGN with only 24μm detections). Because there are only four IRAGN with only 24μm detections, and the effect is not large ($\approx$0.5 dex in L_{IR}), this would not change any of our conclusions if all of these

IRAGN have SEDs of optical luminous quasars. However, the MIPS-to-IRAC colors of the IRAGN in our sample ($F_{24\mu m}/F_{8.0\mu m} = 4.2$ median and ranging from 3.5 to 6.1 for the four IRAGN with only 24μm detections) are highly discrepant compared to those of the Shang et al. (2011) optically luminous SEDs ($F_{24\mu m}/F_{8.0\mu m} = 1.4$ median). Therefore, it seems highly unlikely that the IRAGN in our sample have SEDs like optical QSOs[1]. In this case, we take the lower IR luminosity of a factor of 3.5 to be a lower bound for an extreme case for the IRAGN in our sample.

We found that when only the 24μm and 70μm flux densities are available the estimates of the total IR luminosity are similar to those derived using 24μm only for the Rieke et al. (2009) SED models. And when using the Chary & Elbaz (2001) and Dale & Helou (2002) models the estimates for the total IR luminosity are smaller compared to the that derived with only the 24μm flux density by a median of 0.97 and 0.95, respectively. When all three MIPS flux densities are available the estimate of the total IR luminosity is larger compared to that derived by 24μm only (larger by a median of 1.34, 1.61, and 1.44 for the Rieke et al. (2009), Chary & Elbaz (2001), and Dale & Helou (2002) SED models, respectively). One conclusion from this analysis is that objects in our sample detected at 160μm appear to have a large cold-dust mass which is not sufficiently probed by the 24μm and 70μm bandpasses. However, since the 160μm detections are not complete and preferentially find galaxies with larger-than-typical flux densities, the larger luminosity estimates may have a contribution due to selection bias.

For these reasons, we adopt the IR luminosities derived using the Rieke et al. (2009) SED templates for this work. For all galaxies in our sample, we use the IR luminosity derived from all available MIPS bands.

[1]Indeed, we have an optical spectrum for one of the IRAGN with only 24μm detection and it only shows narrow lines indicative of a Seyfert galaxy, clearly not a broad-line quasar.

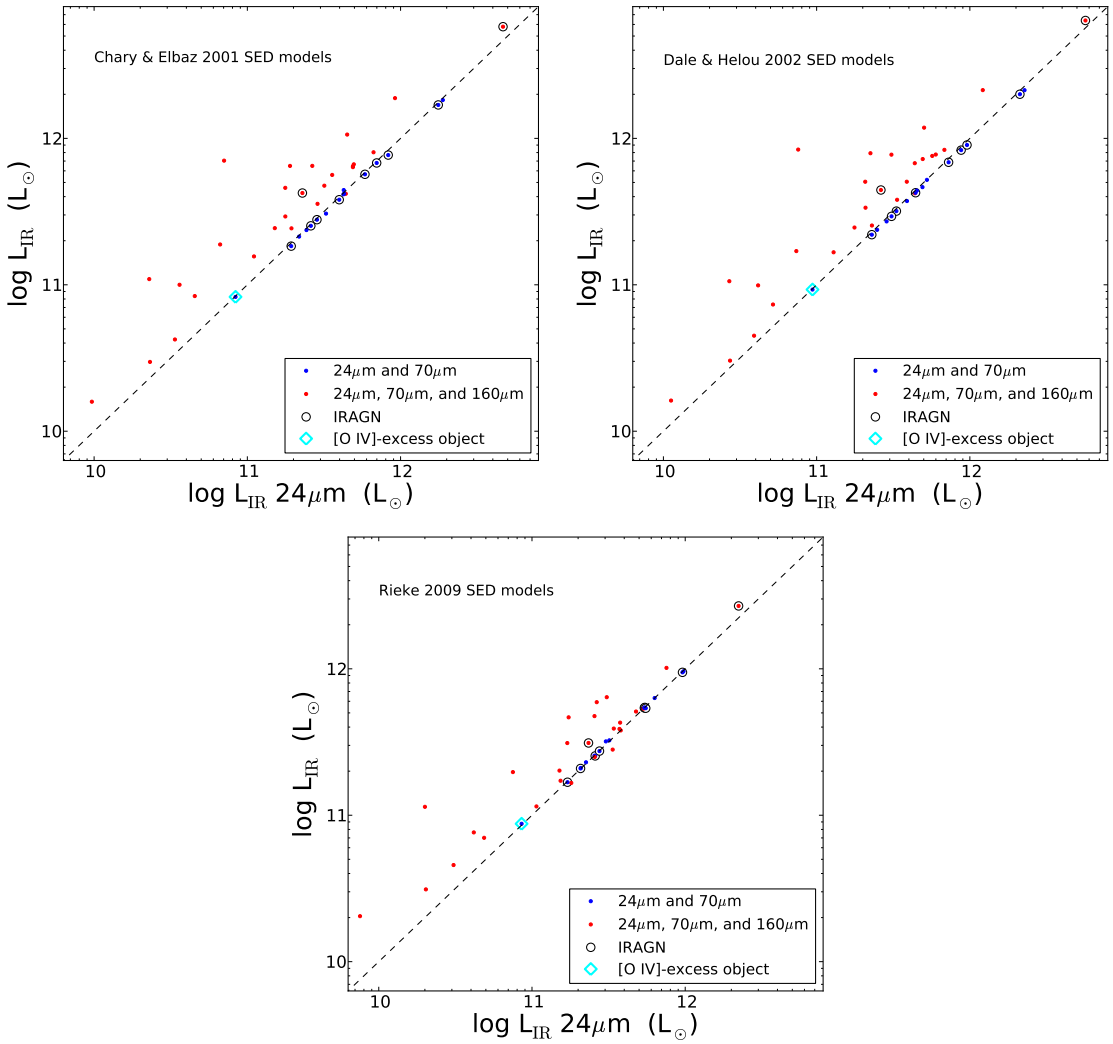

Figure A.1 — The IR luminosities derived from the 24μm data only $L_{IR}(24\mu m)$ compared to the L_{IR} derived using multiple MIPS bands (24μm, 70μm and/or 160μm) for each of the three sets of IR SED models (Chary & Elbaz, 2001; Dale & Helou, 2002; Rieke et al., 2009, as labeled in each panel). The dashed line represents a unity relation between the two L_{IR} estimates. Sources with only 24μm flux densities are not plotted.